2021

Copper Sulfide Manganese Nanoparticles for Multimodality Imaging and Therapy

Ali S. Gawi Ermi

Copper Sulfide Manganese Nanoparticles for Multimodality Imaging and Therapy

A dissertation submitted in partial fulfillment of the requirements for the degree of Doctor of Philosophy in Chemical Biology at Virginia Commonwealth University

By
Ali S. Gawi Ermi, MSc
University Sciences Malaysia, 2009

Directors: Professor Jamal Zweit & Professor Nicholas Farrell
Departments of Radiology and Chemistry

Departments of Chemistry
Virginia Commonwealth University
Richmond, Virginia

May 3rd, 2021

Abstract

COPPER SULFIDE MANGANESE NANOPARTICLES FOR MULTIMODALITY IMAGING AND THERAPY

By Ali S. Gawi Ermi, MSc

A dissertation submitted in partial fulfillment of the requirements for the degree of Doctor of Philosophy in Chemical Biology at Virginia Commonwealth University.

Virginia Commonwealth University, 2021.

Major Director: Professor Jamal Zweit,
Departments of Radiology and Affiliate Professor, Department of Chemistry

Inorganic nanoparticles (NPs) are compatible with metal-based multi-modality molecular imaging and targeted therapy. Copper sulfide nanoparticles (CuS NPs) are attractive photoacoustic and photothermal agents and are amenable to incorporation of radionuclides and paramagnetic elements to facilitate image-guided therapy. The aim of this work is to develop manganese (Mn)-doped CuS NP, intrinsically radiolabeled with radionuclides such as (Zirconium-89 (^{89}Zr), Copper-64/67 ($^{64/67}$Cu) and Manganese-52/55 ($^{52/55}$Mn)). This novel approach combines Photoacoustic (PA), Positron emission tomography (PET), Single-photon emission computed tomography (SPECT) and magnetic resonance imaging (MRI) in one platform. Potentially, such a platform can also accommodate therapeutic radionuclides and enable image-guided radionuclide therapy as well as photothermal therapy (PTT). In this study, two radionuclides were intrinsically incorporated into CuS-Mn NPs, ^{89}Zr for PET imaging and ^{67}Cu for SPECT imaging and potential radiotherapy. Doping of Mn into CuS NPs (CuS-Mn NPs) provided an enhanced T1/T2 MRI contrast. The CuS NP has a high absorption in the NIR region suitable for PA imaging and exhibits high photo-thermal conversion efficiency, adequate for PTT.

A hydrothermal method was developed for the synthesis of $^{89}Zr/^{67}Cu$ labeled CuS-Mn NP, by reacting Sodium Sulfide (Na_2S) with Copper Chloride ($CuCl_2$)/ Manganese Chloride ($MnCl_2$) in aqueous solution under existence of organic/polymeric ligand as a coating. ^{89}Zr or ^{67}Cu was doped into NPs during the synthesis. Hydrodynamic (HD) size of the NPs was measured by dynamic light scattering (DLS). Reaction yields were assessed by inductively coupled plasma optical emission spectrometry (ICP-OES) and gamma counting. Multispectral Optoacoustic Tomography (MSOT) signal was assessed as a function of NPs concentration. Animal PET imaging and biodistribution were done at 30 min, 2 h, and 24 h post intravenous (i.v.) injection. Stability of radiolabeled NPs in water, plasma and urine was evaluated by radio-high performance liquid chromatograph (radio HPLC). Relaxivity characterization was done to study the enhancement of MRI signal by CuS-Mn NP. Animal MRI was performed in mice before and 2 h after injection of CuS-Mn NPs and T1 and T2 weighted MRI images were acquired.

The reaction yield of CuS-Mn NPs ranged from 80-90% as measured by ICP. The radiolabeling yield of [^{89}Zr]-CuS-Mn NP was > 63%. When labeling with the same chemical element as the copper core, the radiolabeling yield of [^{67}Cu]-CuS-Mn NP was almost quantitative. Doping with Mn reduced HD size from 20 nm to ≈ 5 nm, as measured by size distribution DLS. In a phantom study, the MR contrast signal was enhanced two-fold following injection of CuS-Mn NP compared to the bulk molecule $MnCl_2$. The photoacoustic signal response was linear across a NPs concentration ranging from 0.11 µg/ml to 10µg/ml of CuS-Mn NPs.

PET imaging of [^{89}Zr]-CuS-Mn NP showed rapid renal clearance within less than 30 min post injection. This rapid clearance has been facilitated by the ultra-small size (≈3-5nm) of the NP being below the glomerular filtration rate. Enhancement of MRI images was demonstrated in liver

and kidney at 2 hours post injection of the NP. CuS-Mn NP increased signal intensity and contrast following i.v. injection into mice, with the signal intensity decreased over time.

Studies were also conducted with [^{67}Cu]-CuS-Mn NPs, which have a larger size distribution of 10-30 nm. Biodistribution of [^{67}Cu]-CuS-Mn NPs showed rapid liver and spleen uptake due to phagocytosis of larger particle size. Such accumulation resulted in increased hepatobiliary clearance compared to the small NPs which are cleared more through the kidney.

The synthesis and intrinsic radiolabeling of CuS-Mn NPs, using either ^{89}Zr or ^{67}Cu has been demonstrated. The feasibility of multi-modal capability with PET, MRI and PA imaging has been demonstrated. This novel approach of intrinsically labelled radio-nanoparticles can be expanded to incorporate a number of radionuclides and the platform can be modified to carry targeting molecules, enabling the potential of target-specific imaging and therapy (Theranostics).

Acknowledgement

My deepest thanks to Allah for helping me to enlighten my mind while doing this research and pursue this PhD.

First of all, my most profound thankfulness and gratitude goes to my direct supervisor Prof. Jamal Zwiet, for providing me with guidance and support through the period of this research. He has given me the opportunity to learn so much. I am truly thankful to be a student of such a committed and passionate researcher. This thesis could not have been completed without the support of my supervisor.

I would also like to express my special thanks to Dr. Sundaresan Gobalakreshnan, for his guidance, advice, and assistance throughout this research. I learned a lot from him: molecular imaging, cell culture, mouse tail-vein injection, tumor implantation, and much more.

I would like to give special thanks to my thesis committee members, Dr. Nicholas P Farrell, Dr. Sundaresan Gobalakrishnan, Dr. Jessika V Rojas Marin, and Dr. Frank Corwin for their time and dedication.

Special thanks to all of my colleagues at the Center of Molecular Imaging (CMI), especially Dr. Minghao Sun, Dr. Vimalan Vijayaragavan, Dr. Frank Corwin, and Li Wang for their support and for providing me with information regarding the study when I started this project: Minghao with the nanoparticle synthesis, Vimalan, and Frank with MRI, and Li with the cell work and MSOT.

I would like to thank the director of the chemical biology Ph.D. program Dr. Farrell, and the faculty members for their kind help and cooperation. I would like to thank all of my friends, classmates, and laboratory staff.

Special acknowledgment to Nouri Elmekharam, for his assistance in this work and he has been a good companion on the entire journey.

Dr. Joseph Turner, director of the Chemistry Research Instrumentation Facility, thank you very much for your assistance during this study. Dr. da Rocha, Dr. Yang and Judy Williamson, thank you for your cooperation to use your lab facility for NPs characterizations.

I would like to thank all my dearest family members who always gave me support and advised me, especially to my father, mother and my special thanks to my dearest wife for her support and patience during of this journey. Also, my brothers, sisters and my kids, thank you all for prayers, love and support.

Last but not least, my gratitude to the Libyan Ministry of Higher Education for funding my Ph.D. scholarship.

Vita

Ali Gawi was born on February 19th, 1972, in Tripoli, Libya, and is a Libyan citizen. He received his Bachelor of Sciences in Medical Technology from the College of Medical Technology, Misurata, Libya, 1992 (former, Faculty of Medical Technology, Alfateh University for Medical Sciences). After years of work as a Medical Technologist and Application Specialist, he decided to pursue his master's degree. He moved to Penang, Malaysia to start his graduate school and received his Master of Sciences from University Sciences Malaysia, 2009. From 2010 to 2014 he was working as a faculty member and lecturer at the College of Sciences and Medical Technology. In 2014 he was awarded scholarship to pursue his Ph.D. in the USA. In 2015, he started his Ph.D. program in chemical biology at Virginia Commonwealth University.

Table of Contents

List of Tables

List of Figures

List of Abbreviations

Here is the list of abbreviations for the convenience of the reader.

NPs	Nanoparticles
CuS NPs	Copper sulfide nanoparticles
PA	Photoacoustic
PET	Positron-emission tomography
SPECT	Single photon emission computed tomography
MRI	Magnetic resonance imaging
PTT	Photothermal therapy
^{89}Zr	Zirconium-89
^{67}Cu	Copper-67
^{64}Cu	Copper-64
^{55}Mn	Manganese-55
Na_2S	Sodium Sulfide
$CuCl_2$	Copper Chloride
$MnCl_2$	Manganese chloride
HD	Hydrodynamic
DLS	Dynamic light scattering
ICP-OES	Inductively coupled plasma-optical emission spectrometry
MSOT	Multi spectral optoacoustic tomography
HPLC	High performance liquid chromatograph
T1	Longitudinal relaxation time
T2	Transverse relaxation time
cRGD	Cyclic arginine–glycine–aspartic acid
PAA	Poly (acrylic acid)
PEG	Polyethylene glycol
BSA	Bovine serum albumin
αvβ3	Alpha(V) Beta (3)
NOTA	1,4,7-triazacyclononane-1,4,7-triacetic acid
DOTA	1,4,7,10- tetraazacyclododecane-1,4,7,10-tetraacetic acid
^{111}In	Indium-111
CMI	Center of Molecular Imaging
IARC	International Agency for Research on Cancer
EBR	External beam radiation therapy
CT	Computed tomography
DNA	Deoxyribonucleic acid
^{125}I	Iodine-125
^{109}Pd	Palladium-109
^{192}Ir	Iridium-192
^{131}Cs	Cesium-131
^{198}Au	Gold-198
MOA	Mechanism of action

RIT	Radioimmunotherapy
MAbs	Monoclonal antibodies
PSMA	Prostate-specific membrane antigen
^{177}Lu	Lutetium-177
^{225}Ac	Actinium-225
NIR	Near infrared
Au-NPs	Gold nanoparticles
SPR	Surface plasmon resonance
CTLA-4	T lymphocyte-associated antigen-4
PD1	Programmed cell death protein 1
FDA	Food and drug administration
EPR	Enhanced permeability and retention
TNPs	Theranostic nanoparticles
FRα	Folate receptor alpha
MI	Molecular imaging
FDG	[^{18}F]-fludeoxyglucose
^{18}F	Fluorine-18
T	Tesla
SNR	Signal to noise ratio
RF	Radiofrequency field
SAR	Specific absorption rate
Gd	Gadolinium
T1	Longitudinal relaxation time
T2	Transverse relaxation time
r1	Longitudinal relaxivity
r2	Transverse relaxivity
MnO	Manganese oxide
MnS	Manganese sulfide
Mn_2O_3	Manganese trioxide
^{99m}Tc	Technetium-99m
^{1223}I	Iodine-123
NaI	Sodium iodide
CCD	Charged coupled device
Sulfo-SMCC	Succinimidyl 4-(N-maleimidomethyl) cyclohexane-1-carboxylate
EDC	N-(3-dimethylaminopropyl)-N′ -ethylcarbodiimide hydrochloride
NHS	N-hydroxysuccinimide
A549	Human lung carcinoma
U87-MG	Human brain glioblastoma astrocytoma
COLO-205.	Human colon carcinoma
MDA-MB-435	Breast cancer cell lines
ATCC	American Type Culture Collection
DMEM	Dulbecco's Modified Eagle's Medium
FBS	Fetal bovine serum
IACUC	Animal Care and Use Committee

ANL	Argonne National Laboratory
MWCO	Molecular weight cut-off centrifugal filters
^{89}Zr-Oxalate	Zirconium oxalate
$^{89}ZrCl_4$	Zirconium chloride
HCl	Hydrochloric acid
ZP	Zeta potential
TEM	Transmission electron microscope
RP-HPLC	Reversed phase high-performance liquid chromatography
GBCA	Gd-based contrast agents
iv	Intravenous
ICP-MS	Inductively Coupled Plasma Mass Spectrometry
% ID/g	Percent injected dose per gram
CONP	Cerium oxide nanoparticle
SPION	Superparamagnetic iron oxide nanoparticle
Ce $(NO_3)_3$	Cerium nitrate
NH_4OH	Ammonium hydroxide

Chapter 1: General Introduction

1.1 Multimodality Copper Sulfide Manganese Nanoparticle

The merging of nanotechnology with targeted therapy and molecular imaging is gaining a tremendous amount of interest within the biomedical research community. This is because the potential for multi-targeting, controlled delivery and release can now be realized as a more rational approach to the treatment of various diseases. This marriage is also leading to the development of theranostic ("image as you treat") approaches, which can contribute in precision and personalized medicine[1–4]. The main motivation of this project is to exploit the combination of molecular imaging and nanotechnology to develop a theranostic platform that could potentially be used in combination therapy guided by molecular imaging. The nano-platform developed during the course of this research has generated a novel multi-modal nanoparticle probe. It contains stable and radioactive elements that can be detected by positron emission tomography (PET), single-photon emission computerized tomography (SPECT), photoacoustic (PA) and magnetic resonance (MR) imaging. This has been accomplished with a manganese doped copper sulfide nanoparticle (CuS-Mn NP) that can intrinsically incorporate radionuclides for PET, Zirconiun-89 (^{89}Zr), and SPECT, copper-67 (^{67}Cu) imaging. The MR and PA signals are provided by manganese (Mn), and copper sulfide (CuS) respectively. The platform could also contain therapeutic radionuclides to enable nano-radiopharmaceutical therapy guided by imaging (Theranostics).

1.2 Objectives

The overall objective of this project is to develop a novel multi-modal nanoparticle which combines MR, PA, PET, SPECT signals in an "all in one" theranostic platform. The core/shell CuS-Mn NP can be doped with PET radionuclides, such as ^{64}Cu, ^{52}Mn and ^{89}Zr among others, to afford PET imaging. It can also be doped with therapeutic radionuclides such as ^{67}Cu. CuS provides efficient photo-absorption to enable both photoacoustic imaging and photothermal

therapy, whilst doping with Mn allows MRI imaging. The novelty of this technology resides in the fact that the MR, PET/SPECT and PA molecular imaging signals are all coming from the same multi-elemental nanoparticle (Mn-MRI; CuS-PA; ^{67}Cu-/^{64}Cu-/^{89}Zr-/^{52} Mn-SPECT/PET).

1.3 Hypothesis and Aims

We hypothesize that intrinsic labeling or doping of core/shell CuS NPs with radioisotopes and contrast agents, would lead to the development of a multi-modality platform that merges molecular imaging with nanotechnology. Furthermore, the use of therapeutic radionuclides, such as ^{67}Cu could also enable the combination of radiotherapy and photothermal therapy in the same image-guided platform.

The following specific aims have been investigated to demonstrate the feasibility of the working hypothesis:

1.1 Synthesis and physiochemical characterization of CuS NPs and CuS-Mn-doped NPs, including size and charge analysis.

1.2 Optimization of intrinsic radiolabeling of CuS-Mn NPs with the radionuclides ^{89}Zr and ^{67}Cu, as positron and single photon-emitting tracers respectively.

1.3 Evaluate the MR and MSOT imaging performance of Mn-doped CuS and determine minimum amount of Mn needed for adequate MR signal.

1.4 Demonstrate imaging and radiotracer kinetics of radiolabeled CuS-Mn NPs *in vivo* and in a live animal.

1.4 Research Strategy

Manganese-doped-CuS NPs (CuS-Mn) was synthesized with different coating materials such as Poly (acrylic acid) (PAA), Alginic acid, Sodium Citrate, Polyethylene glycol (PEG), and

intrinsically labeled with radionuclides such as ^{89}Zr, ^{67}Cu. Zirconium-89 (^{89}Zr) is a positron-emitting radionuclide with a half-life of 78.41 hours, which is used for PET imaging and *ex vivo* biodistribution studies. Copper-67(^{67}Cu) is a beta-emitting radioisotope which is attractive for medical purposes due to its ability to carry sufficient radiation energy to cause cell death in targeted cells while having a sufficiently short half-life of 62 hours, limiting radiation dose to patients. ^{67}Cu, incorporated in CuS-Mn NP was used as radiotracer tool to evaluate the chemical and biological behavior of radiolabeled NP. CuS-Mn NP provided enhancement in both the PA and MRI signals. To prepare a NP for future targeted imaging, preliminary experiments were conducted to functionalize the CuS-Mn NP various coating, including polyethylene glycol (PEG), or bovine serum albumin (BSA). To demonstrate peptide conjugation to the CuS-Mn NP, cyclo (Arg-Gly-Asp) peptide (cRGD) peptide was used. This peptide has been previously used in our laboratory, to target the alpha(V) beta (3) ($\alpha V\beta 3$) integrins and imaged with PET and MRI.[5]

1.4.1 Extrinsically vs. Intrinsically Radio-labeled Nanoparticles

In order to radiolabel the nanoparticle with radionuclide, two main approaches have been used (Figure 1). The first and most widely used radiolabeling strategy is extrinsically radio-labeled nanoparticle, which involves the use of an exogenous linker that matches with certain isotopes to form stable complex.[6] Well known chelators, such as 1,4,7-triazacyclononane-1,4,7-triacetic acid (NOTA), 1,4,7,10- tetraazacyclododecane-1,4,7,10-tetraacetic acid (DOTA), *p*-isothiocyanatobenzyl- desferrioxamine (Df-Bz-NCS) and diethylene triamine pentaacetic acid (DTPA), etc., have been used for radiolabeling of copper-64 (^{64}Cu, $t_{1/2}$ = 12.7 h), zirconium-89 (^{89}Zr, $t_{1/2}$= 78.4 h) and indium-111 (^{111}In, $t_{1/2}$= 67 h) for imaging in preclinical studies.[7,8] There are many concerns of using traditional radiolabeling strategies include the possible changes of chemical structure of the nanoparticle which lead to altering of *in vivo* pharmacokinetics of

carriers. In addition, the external label is on the surface of the nanostructure and is exposed to chemical and enzymatic activity that may separate the radionuclide from the nanoparticle. This could compromise the label's usefulness for multi-modal imaging as the imaging systems such as PET or SPECT detect signal from the radioisotope.[9] Therefore, an alternative and successful radiolabeling method is required to overcome with these limitations. The second strategy used in this research intrinsically incorporates radionuclide into the core structure of the nanoparticle. The focus here is on developing more reliable chelator-free radiolabeling technique, which could fully take advantage of the unique physical and chemical properties of the nanoparticles for radiolabeling, and more importantly, offer an easier, faster, and more specific radiolabeling possibility. This will ensure effective shielding of the radionuclide within the nano-construct, thereby providing a pharmacokinetic profile indicative of the overall nanoparticle. Additionally, this will simplify the surface coating chemistry and offer a greater surface area for conjugation of the targeting moiety. This intrinsic radiolabeling approach has been studied in Center of Molecular Imaging (CMI) by using different radioisotopes with three types of NPs: cerium oxide NPs with cerium-141, Indium-111, Zinc-65 and Zarconium-89, quantum dots with Indium-111, and superparamagnetic iron oxide NPs with Iron-59 and Manganese-52.[10–13]

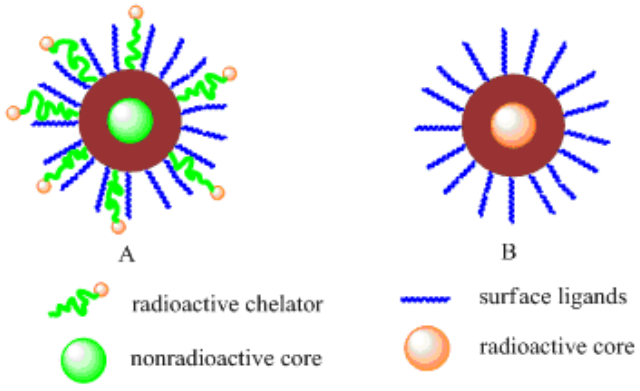

Figure 1: Extrinsically vs. Intrinsically Radio-labeled Nanoparticles. A) Externally labels nanoparticle, by using linker (radioactive chelator). B) Internally incorporates the radioactivity into the core of nanoparticle.

1.4.2 Intrinsically Radiolabeled Manganese-doped Copper Sulfide Nanoparticle

For intrinsic incorporation of radiolabeled CuS-Mn nanoparticles, ^{89}Zr or ^{67}Cu was used. While the synthesis was optimized the ^{89}Zr was used. The ^{89}Zr isotope is a clinically relevant PET imaging isotope and allows for both high activity PET imaging, and *ex vivo* biodistribution to more precisely measure uptake in specific organs. ^{67}Cu is a good candidate, chemically identical to the CuS NP and does not affect chemical structure or physical properties of the nanoparticles. The intrinsic radiolabeling strategy is more stable than using chelator to label the nanoparticle which may cause change on the surface chemistry of the NP. This could increase the nanoparticle binding with plasma proteins, increase the nanoparticle size, and change the pharmacokinetic profile.

1.5 Thesis Organization

This thesis contains eight chapters. The first chapter is a general introduction to the research, including an overview of overall objective and strategy of the approach. Chapter two provides an overview of cancer and nanotechnology and the impact of nanotechnology research on cancer imaging, drug delivery and targeted therapy. Chapter three describes molecular imaging techniques and their application in cancer imaging and therapy. Special emphasis is given to techniques relevant to this project. Chapter four details the research approach and methods adopted in this thesis. Chapter five describes the results of experiments, while chapter six focuses on discussing the results of the research work and how it relates to the literature in the relevant research area. Chapter seven outlines preliminary work on the synthesis of CuS-Mn NPs conjugated with cRGD peptide for potential targeted imaging. Chapter eight provides an overall summary and the way forward.

Chapter 2: Cancer and Nanotechnology

2.1 Cancer

Cancer is a group of diseases, which are characterized by uncontrolled and uncoordinated cell division and growth. Cancer remains a major threat to human health and one of the most leading causes of death. According to estimates from the International Agency for Research on Cancer (IARC), in 2012 there were 14.1 million new cancer cases and 8.2 million cancer deaths worldwide. By 2030, the global burden is expected to grow to 21.7 million new cancer cases and 13 million cancer deaths[14,15]. In the last few decades, advances have been made in early diagnosis and treatment of cancer. In the United States, this has resulted in improved survival rates for many types of cancers[16]. Despite this, cancer is still a major killer, and there is still the need for more advanced and effective diagnostic and therapeutic approaches to reduce the burden of the disease. Cancer was and remains one of the challenges that face scientists. There are many theories studied to answer and explain the behavior and nature of cancer cells, or at least to understand the underlying mechanism of its occurrence and progression. One of the remarkable progress when Hanahan and Weinberg published the hallmarks of cancer that allow normal cells to become cancerous ones (Figure2). These characters which are shared in all types of cancer cells, sustaining proliferative signaling, evading growth suppressors, avoiding immune destruction, enabling replicative immortality, tumor-promoting inflammation, activating invasion and metastasis, inducing angiogenesis, resisting cell death, deregulating cellular energetics, and genome instability and mutation. By understanding and targeting these hallmarks of cancer which the main changes occur in normal cell growth pathways, the treatment of cancer has been improved in most of cancers[17,18].

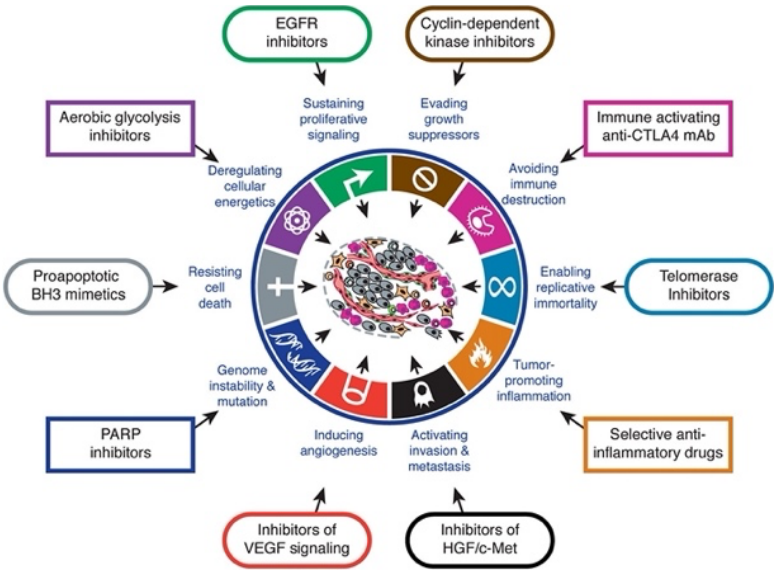

Figure 2**:** Therapeutic Targeting of the Hallmarks of Cancer

2.2 Cancer treatments

Currently, cancer treatment involves surgery, chemotherapy, radiotherapy and biologically targeted therapy[19]. Treatment options depend on a number of factors, including type and severity of the disease, location of the disease and the overall health status of the patient concerned. However, the problems of tumor recurrence, normal tissue damage and moderate to severe side effects are still common among many cancer patients. In recent years, cancer immunotherapy has emerged as a promising and effective approach for a number of cancers, especially melanoma and lung cancer among others.[20,21] Early cancer detection is still paramount, and all the evidence points to the fact that early diagnosis, while the disease is still localized, can lead to better therapeutic outcome. This is because controlling local disease, before tumor spread and metastasis, will always be more effective than treating more advanced disease.[22]

Surgery: is usually the first treatment option. This can be done when the cancer is diagnosis in the early stage and the cancer located only on one area and did not spread to other parts of the body. However, not all surgeries result in complete removal of cancer cells and it is these residual cancer cells that usually lead to recurrence. Some of these cell clusters are pre-cancerous stem cells which

are never eradicated by surgery. Surgery also used for diagnosis of cancer where small piece of the tissue called biopsy tested for the presence of cancer, type of cancer, and rate of growth. Recent advances in targeting stem cell therapy are still at the experimental stage and the potential of this approach could help eradicate the "roots" of cancer cells.[23,24]

Radiotherapy: is widely used in the treatment of cancer. The most commonly used approach is external beam radiation therapy (EBR). The radiation used is called ionizing radiation because it forms electrically charged particles to irradiate a field of view, previously planned by image guidance using computed tomography (CT) or magnetic resonance imaging (MRI). This energy can kill cancer cells or cause genetic changes (damages deoxyribonucleic acid, DNA) resulting in cancer cell death. Advances in the physics of EBR has resulted in more beam focused therapy, such is the case of confocal radiotherapy.[25] In addition to CT and MRI, which provide excellent morphological detail, high resolution positron-emission tomography (PET) has been applied to determine functional volume of the tumor in order to guide a more effective EBR.[26]

Brachytherapy: is another type of radiation therapy and also known as internal radiation therapy where the source of radioactive material is placed inside the patient body into or close to the tumor to irradiate cancer cells. In this way the damage to normal cells can be reduced. Therefore, brachytherapy delivers precise radiation doses to the tumor from the inside out. Brachytherapy can be administered in different ways, including intracavitary, interstitially, intraluminal, and intravascular.[27] The duration of treatment is dependent on the half-life of the radio isotope placed in the tumor area. Radioisotopes used in brachytherapy include, Iodine-125 (^{125}I), Palladium-109 (^{109}Pd), Iridium-192(^{192}Ir), Cesium-131 (^{131}Cs), and Gold-198 (^{198}Au).[28] The delivery of radiation to the tumor site has been improved by incorporating of imaging modalities and delivery systems such as nanoparticles.[29,30]

Chemotherapy: is still a major treatment modality despite the failure of many therapeutic regimens used. In general, chemotherapeutic drugs are usually, if not always associated with mild to severe side effects. It is side effects is further exasperated by the fact that chemotherapy is cytotoxic and does not discriminate normal from cancer cells. In advanced metastatic disease, it is given systemically and hence all types of cells and tissue get exposed to the chemotherapy. Damage to bone marrow, intestinal mucosa, and hair follicles is not uncommon. Damage to bone marrow cells can cause anemia and affect immune system which lead to patient discomfort and more importantly compromising the body defense mechanisms against for example "opportunistic" infection.[31] These side effects sometimes cause dose reduction and delay in treatment or discontinuation of therapy. There are many types of chemotherapeutic agents which are classified according to chemical nature and function, some of well know classes are listed in table 1. They have been used in cancer treatment depending on the type of cancer and the mechanism of action of the anticancer agents. The efficacy of chemotherapy agents depends on the drug concentration against the specific site of the tumor. It is very important that chemotherapeutic agent be delivered to the site of the cancer. This will minimize the exposure to surrounding normal and healthy tissue.[32] The use of drug delivery systems such as nanoparticles will help to deliver chemotherapy agents to the tumor site and do not affect surrounding normal tissues. In clinical use there are different types of the nanocarriers that used to deliver chemotherapies drugs and many others in clinical trials. Examples of food and drug administration (FDA) approved nanomaterial chemotherapy agents are liposomal doxorubicine (Doxil), liposomal irinotecan (onivyde), and liposomal vincristine (Marqibo). Liposomes are the most widely used NP as a drug delivery system[33].

.

Table 1: Classification of chemotherapeutic agents and mechanism of action (MOA) with the examples.[34]

Type of the agent	MOA	Treatment of	Examples
Alkylating agents	Damage DNA and prevent mitosis.	leukemia, lymphomas, multiple myeloma, sarcoma and lung, breast, and ovarian cancer	Nitrogen mustards such as chlorambucil Alkylsulfonates such as busulfan Nitrosoureas such as streptozotocin Triazines such as dacarbazine Ethylenimines such as thiotepa and altretamine Platinum drugs such as cisplatin, carboplatin and oxalaplatin
Antimetabolites	Interrupt the S phase and substitute normal DNA and RNA with other amino acids.	Leukemia and cancers of the breast and ovary	5-fluorouracil (5-FU), 6-mercaptopurine (6-MP), cytarabine, capecitabine, fludarabine, gemcitabine, methotrexate, pemetrexed, pentostatin and thioguanine.
Anti-tumor antibiotics or Anthracyclines	Inhibit the enzymes that bring about DNA replication	Lymphoma, solid tumors, bone and soft tissue sarcomas	Doxorubicin, daunorubicin, idarubicin and epirubicin.
Topoisomerase inhibitors	Inhibit the enzyme topoisomerase	Leukemia and lung, ovarian and gut cancer	Topotecan, irinotecan, etoposide and teniposide.
Plant alkaloids or Mitotic inhibitors	Interrupt the M phase of the cell cycle and inhibit mitosis	Breast and lung cancers and myeloma, lymphoma, and leukemia	Taxanes such as paclitaxel and docetaxel, vinca alkaloids such as vinblastine, vincristine and vinorelbine.

Biological targeted therapy: as the name suggests, in this type of treatment a specific molecule is targeted to the tumor site. Such molecules range from small to macro-molecules including monoclonal antibodies and peptides. Targeting certain entities expressed on cancer cells may help increase the specificity of these agents and reduce damage to healthy cells that do not express such binding entities to the targeted agent. These molecules can stop the spread of cancer cells by blocking specific molecules which involved in the growth of the cells and metastasis. For instance, specific receptors which are only expressed on the surface of cancer cells can be identified and targeted. Many molecules have been engineered to increase their selectivity and hence enhanced binding to, for example receptors over-expressed by the cancer cells.[35] Some targeting molecules have been radiolabeled with therapeutic radioisotopes to produce targeted radio-pharmaceutical therapy with beta- and alpha-emitting radioisotopes. [36,37]. These molecular targeted therapies have shown remarkable success in clinical use for treatment of breast, leukemia, colorectal, lung and ovarian cancers. The main types of targeted cancer therapies are monoclonal antibodies, small molecule inhibitors and immunotoxins.[38,39]

Radioimmunotherapy (RIT): In RIT uses specific monoclonal antibodies (MAbs) or antibody fragments (peptides) against specific antigens on the surface of cancer cells, as targeting vehicles of α- or β-emitting radionuclides. The MAbs or peptides linked to radioisotopes by using a chelator to form radioimmunoconjugate (Figure 3). These radioimmunoconjugates are able to bind to cancer cell surface and deliver the radiotherapy to the tumor and cause damage only to the targeted cancer cells and not to the normal cells. The level of damage depends on the type of the radionuclide and dose. For example, MAbs against prostate-specific membrane antigen (PSMA) have been radiolabeled with Lutetium-177 (^{177}Lu).[40] PSMA is an antigen expressed on prostatic cancer cells. ^{177}Lu is a beta-emitting radioisotope with a half-life of (6.7 days) that is compatible

with the *in vivo* kinetics of MAbs. Clinical experience with ^{177}Lu-PSMA in men with advanced prostate cancer is encouraging.[41] More recently, alpha-emitting radioisotopes have been used with remarkable success in treating castrate- resistant metastatic prostate cancer. The use of the alpha-emitter, Actinium-225 (^{225}Ac) conjugated to anti-PSMA molecules has shown to be very promising and effective against such metastatic disease.[42] The combination of immunotherapy with radiotherapy and chemotherapy has recently been proposed to enhance therapeutic effect in lung cancer.[43]

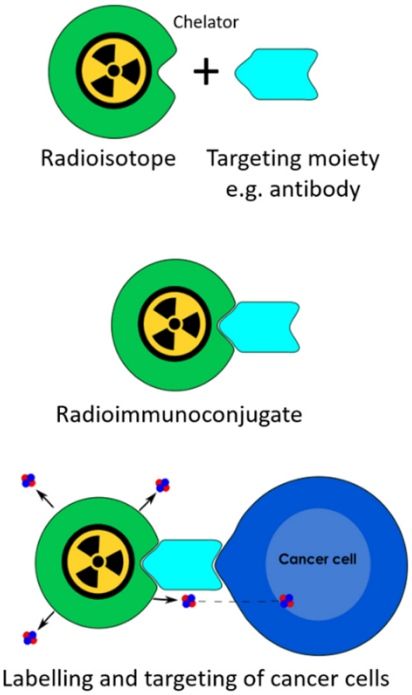

Figure 3: The principles of radioimmunotherapy

Photothermal therapy (PTT): is a treatment modality in which tumors are ablated by heat following absorption of light. Currently, several heating resources such as laser light, focused ultrasound and microwaves have been employed in thermal cancer therapy. When heat is generated in the tumor site, the ablation efficacy can be significantly enhanced. This can be achieved by targeting near infrared (NIR) molecules. Compared with other therapeutic modalities, PTT shows high specificity

and selectivity, with less damage to normal cells if the NIR molecule can be efficiently targeted and retained at the tumor site.[44] Photothermal agents can also be combined with chemotherapy or radiotherapy to enhance efficacy of the treatment.[45] The cancer cells become more sensitive to radiotherapy or chemotherapy because of thermal stress, and this results in an improvement in cancer survival rate. For example, photothermal with a combination of radiotherapy studies for treatment of metastatic head and neck squamous cancers showed improvement results without causing toxicity. Also, another enhancement was seen with phototherapy combined with chemotherapy drugs for treatment of malignant melanoma.[46] The massive invasion of heat could cause damage for normal and healthy tissues. As a result, of whole-body hyperthermia cardiovascular side effects and gastrointestinal symptoms can be seen. This makes conventional PTT limited. Therefore, specific energy absorbing nanomaterials are needed, which can be *in vivo* localized to target tumors to absorb energy and facilitate photothermal therapy.[47,48]

Recently, PTT has been used with the nanoparticles (NPs) to help with localized treatment and minimize effect on normal tissues. Gold nanoparticles (Au NPs) have been developed as effective PTT agents, and this is due to the fact that these NPs utilize the surface plasmon resonance (SPR) which make them stronger absorption in visible and near infrared (NIR) regions.[49] Copper sulfide NPs (CuS NPs) have developed as a new class of PTT agents over the past few years. There are three major advantages of CuS NPs in terms of their translational applications and compared to Au-NP: i) consistent NIR absorption, ii) low cost, and iii) better degradability profile *in vivo*. Instead of SPR effects, the NIR light absorption of CuS NPs derives from d-d energy band transition of Cu^{2+} ions, and therefore the absorption wavelength of CuS NPs is not affected by the size, particle shape, and surrounding environment. This feature can benefit the application of CuS-NPs in different ways. First, in the CuS-NPs synthesis there is no need for control of morphology

or shape to maintain SPR effects. Second, CuS-NPs can be made in smaller size (<10 nm), which may lead to improve pharmacokinetic, biodistribution and fast renal clearance profile. This is importance for toxicity concerns of NPs. Third, the stability and consistence of NIR absorption of CuS-NPs in solutions, cancer cells, or *in vivo* environment, helps to better predict *in vivo* PT properties of CuS-NPs based on *in vivo* experimental observations. Fourth, similar quantities of CuS-NPs are about 200 times cheaper than that of Au-NPs, in term the cost of making.[50,51] In addition to the above consideration, the incorporation of imaging moieties into the NP platform is essential because it provides for a direct means to examine not only the efficacy of the therapy, but it also enables *in vivo* pharmacokinetics and underlying biology to be assessed non-invasively *in situ* and within the intact *in vivo* environment.[52] In this research, a promising multimodality CuS-Mn NP will be studied which could be used for targeted localized PTT.

2.3 Emerging cancer therapies

Immunotherapy: in this type of cancer treatment the immune system for the patient is activated to fight the tumor. These types of drugs are made by the body or in the laboratory to improve the immune system by stopping the cancer from growing or spreading. There are several forms of immunotherapy including cancer vaccines, oncolytic viruses, adoptive transfer of *ex vivo* activated T and natural killer cells, non-specific immunotherapies, and administration of antibodies or recombinant proteins that either co-stimulate cells or block the so-called immune checkpoint pathways.[53,54] One of the most successful immunotherapeutic platforms is the use of monoclonal antibody to block cytotoxic T lymphocyte-associated antigen-4 (CTLA-4) which is a type of immune checkpoint receptor or negative regulator of T-cell immune function. Another checkpoint inhibitor antibody, nivolumab, a monoclonal antibody (mAb) which targets the programmed cell death protein 1 (PD1) receptors on T-cells. Two of anti-PD-1 antibodies have been approved by

the FDA for the treatment of metastatic melanoma and shows a higher survival rate. Many immunotherapy treatments for preventing, managing, or treating different cancers can also be used in combination with surgery, chemotherapy, radiation, or targeted therapies to improve their effectiveness.[55,56]

2.4 Cancer nanotechnology

The study and application of materials in the nanoscale range (1-100's of nanometer) is known as nanotechnology. There are many applications of nanotechnology in cancer such as prevention, diagnosis, therapy and combination of diagnosis and therapy (Theranostic).[57] Recent years have shown a tremendous expansion in the field of nanomedicine with the development of various types of nanoparticles (NPs) geared towards both diagnosis and treatment of cancer.[58] Compared to "bulk" molecules, NPs have unique physiochemical and biological properties given their small size and large surface area-to-volume ratio.[59] Such features allow them to bind, absorb, and carry many types of chemicals, including proteins, small molecule drugs, DNA, ribonucleic acid (RNA), and probes such as radioisotopes, and contrast agents. There are over 200 nanomaterials approved for clinical use and clinical trials.[60] The first FDA approved nanomaterial was Doxil, a nano formulation of liposome to deliver a chemotherapy drug (doxorubicin) to tumor cells with less toxicity to normal cells[61]. A number of applications have been explored using NPs, including drug delivery, targeted drug therapy, photo-thermal therapy as well as multi-modality molecular imaging. Over the last decade, many types of organic and inorganic NPs have been developed. These include metal- and polymer-based nanomaterials.[62] The research described here focuses on the development of the inorganic copper sulfide NP as a platform, which is amenable to contain both therapeutic cargo and imaging moieties enabling image-guided studies.

2.4.1 Nanoparticles

Nanoparticles (NPs) have unique physiochemical properties given their small size and large surface area to volume ratio, which allows them to bind, absorb, and carry compounds such as small molecule drugs, proteins, radioisotopes, and probes with high efficiency.[63] Also, The NPs have the ability to accumulate at the tumor by the enhanced permeability and retention (EPR) effect, which means that they are better absorbed and dispersed within the tumor cells than normal cells.[64] Due to these unique properties, nanoparticle can combine cancer diagnosis and therapy in one platform, a theranostic NPs.[65] Theranostic nanoparticles (TNPs) are a multifunctional nanomaterial which designed and characterized for disease management. They have ability to combine diagnostic and therapeutic in one biocompatible and biodegradable nanoparticle.[66] In the last decades, there has been interest in the development of various types of theranostic nanoparticles for cancer imaging and therapy. Effective targeting theranostic nanoparticles to specific site (tumor) is crucial for both diagnosis and therapy. However, there are many requirements for biocompatible TNPs with highly specific *in vivo* tumor-targeting capabilities, which need to be realized. TNPs must accumulate rapidly and selectively at the target of interest, report biochemical and morphological properties of the disease, site-specific drug delivery without affecting healthy tissues. In addition, they must also have fast clearance from the body or to be degraded to nontoxic byproducts. These NP features depend on a number of properties including size and overall charge. Ultra-small NPs (HD size = 1-5 nm) are below the threshold of renal clearance, while larger NP (e.g., >20 nm) are usually cleared through the hepatobiliary system [67,68]. Although, many types of TNPs have been developed over the last decades, few meet all the ideal criteria. Nanoparticles have been made of different materials, organic nanomaterials or in organic nanomaterials. For example, carbon nanotubes, quantum dots, liposome NPs, polymer NPs and

metallic NPs (Figure 4). Among the metal-based NPs, gold NPs (AuNP) have been the most developed and accelerated towards clinical trials. This is mainly due to their plasmonic effects and high photothermal efficiency.[69] NPs have also attracted attention in bioimaging and the most studied in this regard include silica NPs gold NPs, cerium oxide NPs, magnetic NPs and polymer NPs. Inorganic nanoparticles are compatible with incorporation of metals to facilitate multi-modality molecular imaging and targeted therapy.[70] They also offer the opportunity to incorporate SPECT or PET imaging radionuclides to track and guide delivery of therapeutics.[71]

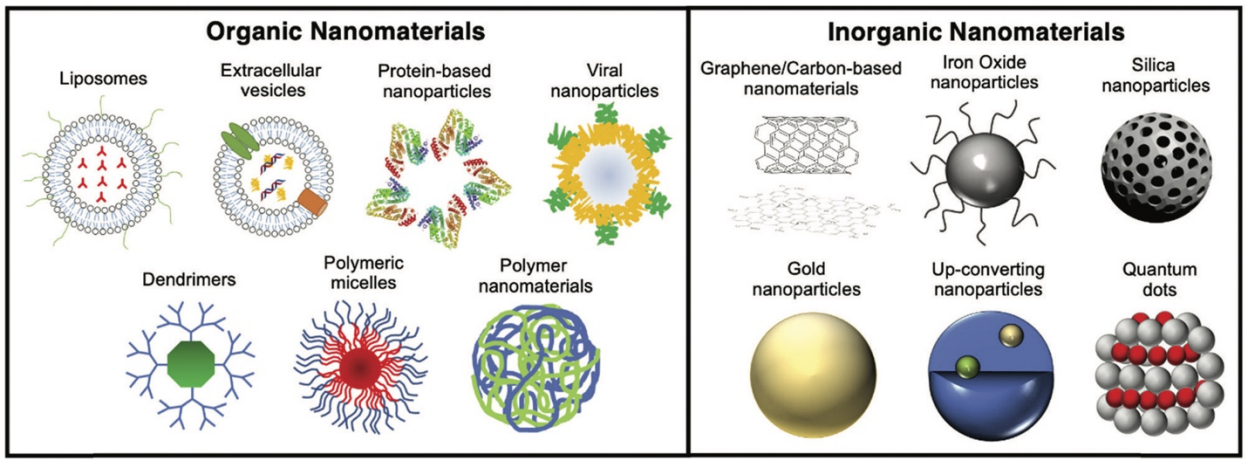

Figure 4: Different type of the NPs, organic nanoparticles and inorganic nanoparticles.[72]

2.4.2 Types of nanoparticles as a nanocarrier

There are many types of the nanoparticles which have been used as a drug delivery system, liposomes and simple polymers were the first generation of the nanocarriers. Liposomes are formed of phospholipids and they have a polar head and hydrophobic tail to form spheres. Their size ranges are from ten nanometers to hundreds of nanometers. Liposomes have the ability to deliver hydrophilic or hydrophobic drugs and their surface can be functionalized with polyethylene glycol (PEG). This will help to increase their stability *in vivo*. The other first generation of the nanocarriers is simple polymer which consists of natural polymers such as polysaccharides and polypeptides that contain sugars and amino acids. For example, chitosan and albumin, in addition

to polylactic acid and polyglycolic acid or a combination of both. This type of nanoparticles also can be used as a drug delivery system for non-soluble treatment. The main advantage of liposomes and polymers are biocompatible and biodegradable. Micelles are another type of complex polymer which can be used as a drug nanocarrier. Micelles are made of self-assembling molecules that contain hydrophobic and hydrophilic segments which are able to deliver hydrophilic and hydrophobic drugs. A branched polymers nanoparticle also named dendrimers are a new generation of the nanocarriers which are made of natural and non-natural components. The other type of nanoparticles include metal or oxide-based nanocarriers (gold, copper, magnetic, quantum dots, titanium dioxide, zinc oxide, and silica), carbon based nanocarriers (nanotubes and fullerenes), and hybrids of materials such as lipid-coated or polymer-coated nanocarriers. [73,74]

2.4.3 Copper sulfide nanoparticles CuS NPs

One of the metal-based NPs attracted in biomedical research is a CuS NP**.** It has a multifunctional property and has been studied for different applications such as biosensing, DNA detection, glucose detection, immunosensor, drug delivery, photoacoustic and photothermal therapy. Also, they are merging and promising for combination diagnosis and therapy for cancer (Theranostics). [75,76] They are attracted because of stability, easy synthesis, biocompatible, low toxicity and low cost. [77,78] CuS NP has strong near-infrared (NIR) optical absorption (700-1100nm) acquired from the d-d transition of Cu^{2+} ions and does not depend on morphology.[77] However, gold NP (AuNP) which is the most investigated metal-based NPs which is depends on surface plasmon resonance (SPR).[79] It is very important for the NPs to be cleared from the body to avoid toxicity and accumulation. CuS NP showed fast and easy clearance and better biodegradable compared to AuNP. This is due to non-metabolize nature of AuNP which related with their non-biodegradable characteristics. On the other hand, CuS NP can be removed by hepatobiliary after

metabolism of Cu by hepatocytes. [80,81] CuS NP has high photothermal conversion efficiency which can be exploited for photothermal therapy. In addition, ^{64}Cu and ^{67}Cu radionuclides can be integrated into CuS NP [82]. These features make CuS NP an emerging as a multimodality platform for imaging and therapy.

2.4.4 Nanotechnology for prevention and diagnosis of cancer

Nanoparticles can be used to prevent cancer disease by delivering tumor specific antigen to the immune system to produce immune response against cancer. Also using the nanoparticle for biosensing and diagnostic imaging will help with diagnosis of cancer. The example for biosensing is by detecting specific cancer markers utilizing nanomaterials.[83,84] The use of molecular imaging improved detection and monitoring of the cancer treatment. Imaging systems utilizing various types of nanoparticles because of their ability to generate imaging signals and their surface has the ability to be functionalize with targeting molecules and some nanomaterials can produce more than one signal, this makes them a multimodality that can be used for more than one imaging systems. In addition, some nanomaterials have the ability to combine diagnostic and therapeutic agents. Imaging systems that utilize iron oxide, gold nanoparticles, copper sulfide nanoparticles or carbon nanotubes may have a theranostic value because these nanomaterials may be employed for therapy in addition to imaging through their thermal ablation capabilities. New imaging modality such as photoacoustic imaging are using nanoparticles as a contrast agent.[85]

2.4.5 Nanotechnology for cancer therapy

As mentioned in 2.1, the use of traditional therapeutic agents has been shown to have side effects on the patients. The use of nanomaterials as nanocarriers for drug delivery may overcome some of these problems. The advantages of using nanoparticles as a drug delivery system are: 1-

To avoid drug degradation or solubility *in vivo*, the drug can be encapsulated within nanomaterials. 2-There surface can be functionalized with different molecules which are drugs, an imaging agent, and a targeting moiety as a ligand or antibody. 3-The nanoparticles are able to accumulate at the cancer site because of EPR effect properties. This is due to the fact that the gaps between endothelial cells at the cancer site. This causes leakage of nanocarriers and gets retained there because of defective lymphatic drainage, which results in passive targeting cancer tissue. 4-Active targeting nanoparticles to target specific molecules expressed only on the surface of cancer cells. For instance, folate receptor alpha (FRα) is a tumor marker expressed by certain epithelial cancers while in normal tissue it is not accessible through the blood. In cancer, receptors on endothelial cells have been targeted to remove cells from their blood supply. Examples for such receptors include integrins α2bβ3, αvβ3, and α5β1. Actively targeting cancer cells or endothelial cells by nanocarriers results in more effective therapy while avoiding nonspecific toxicity to normal cells. 5-Nanocarriers may overcome drug resistance by loading more than one drug onto nanoparticles.[86,87]

The work described here is concerned with the development of doping manganese copper sulfide nanoparticles (CuS-Mn NPs) for multimodality imaging and therapy. Such NP has inherent near ideal properties including, stability, easy synthesis, high photothermal absorption, biocompatibility, low toxicity and lower cost, compared to, for example gold NPs.[82] Doping with manganese enables MRI and the CuS core/shell can also accommodate radioisotopes of Cu, Mn and other PET/SPECT/ radioisotopes. Copper and manganese are natural trace elements in the body and are generally less toxic than heavier metals especially at low concentrations.[88]

Chapter 3: Molecular Imaging

3.1 Molecular imaging (MI)

Molecular imaging is a multidisciplinary field that combines chemistry, biology, mathematics and medicine. It has the capability to visualize, characterize, and monitor biological processes at the molecular and cellular levels and in real time in live subjects. The field has had a huge impact, particularly in the last two decades, in the management of cancer patients. [89–91] The use of [^{18}F]-fluorodeoxyglucose (FDG)-PET for example, revolutionized cancer detection, staging, and how best to monitor response to therapy. This is because, the technique can highlight disease in any part of the body, thereby overcoming sampling limitations.[92] The recent development of total body PET/CT is a major advance in that it provides a snapshot of the whole body faster and more quantitative than conventional PET.[93] Clinically applicable molecular imaging technologies include magnetic resonance imaging (MRI), positron emission tomography (PET), and single photon emission computed tomography (SPECT). PET and SPECT are truly molecular imaging modalities because they are based on specifically targeted radiotracers. MRI and ultrasound (US) can obtain molecular and functional information when used with specifically targeted contrast agents.[94,95] Nowadays, PET and SPECT are combined with x-ray computed tomography (CT) to provide functional information within a specific anatomical location. These techniques use non-ionizing electromagnetic (MRI) and ionizing (CT, PET, SPECT) radiation with infinite penetration and hence can detect deep seated legions. Fluorescence, bioluminescence, photoacoustic and other optical-based techniques have wide applications in small animal imaging and as of now they are not clinically viable due to limited penetration of light photons.[96] Table 2 summarizes unique features of imaging technologies utilized in this project. Figure 5 shows the spectrum of medical imaging which ranks the ability to image low concentrations (Sensitivity) of specific molecules (Specificity).

Figure 5: Schematic showing the spectrum of medical imaging which ranks the ability to image low concentrations (Sensitivity) of specific molecules (Specificity).

Table 2: Characteristics of medical imaging modalities[97]

Imaging Modality	**Signal for image generation**	**Spatial resolution**	**Temporal resolution**	**Depth**	**Sensitivity**	**Type, Amount of the probe**
Magnetic resonance imaging (MRI)	Radiowaves	25–100 μm	minutes to hours	no limit	10^{-3}–10^{-5} mole/L	activatable, direct or indirect, micrograms to milligrams
Positron emission tomography (PET)	High-energy γ rays	1–2 mm	10 sec to minutes	no limit	10^{-11}–10^{-12} mole/L	Radiolabeled, direct or indirect, nanograms
Single photon emission computed tomography (SPECT)	Low energy γ rays	1–2 mm	minutes	no limit	10^{-10}–10^{-11} mole/L	Radiolabeled, direct or indirect, nanograms
Photoacoustic (PA)	Frequency sound (laser excitation)	50-500 μm	seconds to minutes	mm to cm	not well characterized, likely 10^{-9}–10^{-12} mole/L	limited activatable, direct, micrograms to milligrams
Optical fluorescence imaging	Visible light or near-infrared	2–3 mm[g]	seconds to minutes	<1 cm[h]	not well characterized, likely 10^{-9}–10^{-12} mole/L	activatable, direct or indirect, micrograms to milligrams

Table2: Continuous, Characteristics of medical imaging modalities

Imaging Modality	Principal use	Advantages	Disadvantages	Clinical Application	Quantitative degree	Cost
Magnetic resonance imaging (MRI)	morphological reporter/gene expression, receptor/ligand if many receptors	highest spatial resolution, combines morphological and functional imaging	relatively low sensitivity, long scan and postprocessing time, mass quantity of probe may be needed	Yes	++	$$$$
Positron emission tomography (PET)	metabolic, reporter/gene expression, receptor/ligand, enzyme targeting	high sensitivity, isotopes can substitute naturally occurring atoms, quantitative translational research	PET cyclotron or generator needed, relatively low spatial resolution, radiation to subject	Yes	+++	$$$$
Single photon emission computed tomography (SPECT)	reporter/gene expression, receptor/ligand	many molecular probes available, can image multiple probes simultaneously, may be adapted to clinical imaging systems	relatively low spatial resolution because of sensitivity, collimation, radiation	Yes	++	$$$
Photoacoustic (PA)	melanoma and lymph node metastases	spectral information and optical contrast characteristics, high resolution, deeper into body than fluorescence imaging	shielding by strongly absorbing objects newer technology with few current probes	Yes, but limited	++	$$-$$$
Optical fluorescence imaging	reporter/gene expression, cell trafficking	high sensitivity, detects fluorochrome in live and dead cells	relatively low spatial resolution, surface-weighted	yes, but limited	+ to ++	$–$$

3.1.1 Magnetic resonance imaging (MRI)

The first clinical use of MRI was in 1980. Since then, MRI has become a widely use and powerful tool to examine anatomical abnormalities caused by various diseases. MRI provides a three-dimensional image with good soft tissue contrast and submillimeter spatial resolution that can be used for diagnostic and therapeutic purposes. This is obtained by avoiding exposure to an ionizing radiation. MR imaging applications include cardiac imaging, neuroimaging, musculoskeletal imaging, to angiography.[98–101]

The basic principle of MRI depends on the fact of that certain atomic nuclei, such as the hydrogen nucleus (^{1}H) which consists of proton and neutron with a net positive charge, and has a property known as ‘‘spin’’. When the strong external magnetic field (B_0), which usually ranges from 0.2-7 Tesla (T), is applied to nucleus, their spin aligns in parallel or perpendicular to the external field. A subject (tissue of the patient or animal) containing many nuclear spins, placed within the B_0 field, will have an extra spin in the same direction as B_0. During their alignment, the spins precession along this axis is under a specified frequency proportional to the magnetic field, known as the Larmor frequency ($\omega 0$) which is calculated by equation (1).

$$[\omega 0 = \gamma B_0] \qquad (1)$$

Where γ is the gyromagnetic ratio of the particles of interest (^{1}H= 42.58 MHz/T) (Figure 6, A). The image signal to noise ratio (SNR) depends on the strength of the fields (B_0), where higher strength fields result in higher image SNR which result in reduced radiofrequency field (RF) homogeneity and increased specific absorption rate (SAR). Due to the introduction of RF to the nuclei, the protons absorb energy and are excited to the transverse state (Figure 6, A). The excited nuclei relaxed to their initial state, after the disappearance of the RF pulse. Two types of relaxation pathways, longitudinal or T1 relaxation, including the decreased net magnetization in the *z*-direction recovering to the initial state (Figure 6, B). The transverse or T2 relaxation is the second one, where the induced magnetization on the perpendicular plane (*x y* plane) decreases by the dephasing of the spins (Figure 6, C). The two relaxation measurements are used to reconstruct images where different tissues show different values for T_1 and T_2. T_1 weighted images show better differentiation for fatty tissues, while T_2 weighted images are better for showing water content.[102,103]

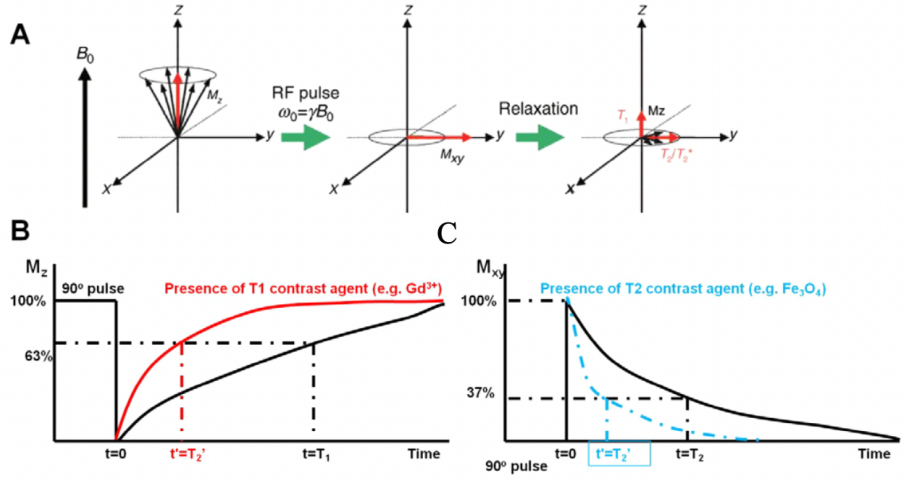

Figure 6: A) Principle of MRI: spins align parallel or antiparallel to the magnetic field and precess under the Larmor frequency; after introduction of the RF pulse the magnetization of the spin changes; excited spins undergo both T1 and T2 relaxation processes. B) T1 relaxation of protons which is shortened under the presence of T1contrast agents (e.g., Gd), which will generate a brighter image. C)T2 relaxation of protons is shortened under the presence of T2 contrast agents (e.g., Fe_3O_4 NPs), which will generate a darker image.[104]

3.1.2 Contrast agents for MRI

The endogenous MR contrast of different tissues has been shown more flexibility than in other clinical imaging systems; nevertheless, to detect pathologies the utilization of exogenous contrast metals which are able to differentiate the normal and diseased tissues by modifying their intrinsic parameters are required. The metal contrast agent efficiency depends on their longitudinal (r1) and transverse (r2) relaxivity, which are defined as the increase of the nuclear relaxation rate (the reciprocal of the relaxation time) of water protons produced by one mmol/l of contrast agent. The contrast agents are classified as T1 or T2 based on their relaxation processes.[105]

Contrast-enhanced MRI is widely used to diagnose soft tissue and vascular abnormalities.[106] To enhance the contrast in MRI images, paramagnetic compounds, with a large number of unpaired electrons, such as gadolinium (Gd)-based compounds, are desirable as contrast agents because they can shorten the longitudinal relaxation time (T1) and the transverse relaxation time (T2), and increase tissue signal intensity on T1 weighted images. However, safety concerns limit the use of Gd-based and iodinated (I) MRI contrast media in renal compromised patients. More recently, a number of reports have identified dose dependent Gd accumulation in the brains of patients with normal renal function that have received contrast-enhanced MRI, raising further concerns by the FDA regarding this class of compounds. Gd retention in a subset of patients further underscores the need for a Gd-free alternative to enhance MR contrast.[107,108] Therefore, a new enhanced and safe contrast agent, compatible with renal impairment is sorely needed.

The transition metal ion manganese (Mn^{2+}), with five unpaired electrons, can produce a very efficient positive contrast enhancement and offers an attractive alternative to Gd-based MRI contrast agents. Manganese is a trace micronutrient in the human body that, along with other transition metals (Fe, Cu, and Zn), play essential roles in health and disease. In this sense, Mn is a biologically relevant micronutrient metal ion and therefore has a much lower toxicity than lanthanides or other heavy metals. In fact, Manganese chloride ($MnCl_2$) has been approved by the FDA as a T1 contrast agent. In addition to $MnCl_2$, most other Mn-based MRI contrast agents have predominately been developed as coordination complexes with acyclic or macrocyclic ligands. Some recent developments have been based on different forms of Mn-based nanoparticles, such as manganese oxide (MnO), manganese trioxide (Mn_2O_3) and manganese sulfide (MnS).[109,110] Despite this, Mn-based agents developed so far, did not translate into clinical use because of modest contrast enhancement at low safe doses, and if used at higher concentrations, they tend to

induce toxicity particularly in the brain, a condition called (Manganism). Therefore, the hypothesis here is that a trace Mn content within a safe and biologically compatible metal platform, could provide high contrast at low doses. Accordingly, previously developed intrinsic nanoparticle (NP) labeling technology will be exploited to develop a new CuS nanoparticle doped with trace amount of Mn (CuS-Mn NP), as a novel platform with 1.5-2-fold higher contrast enhancement than the commercially available Gd-based MRI contrast agents. In this project, we present the development of a new copper sulfide-doped manganese (CuS-Mn) nanoparticle with ultra-small size and biocompatible coating that facilitates rapid renal clearance. The product is a novel and safe MRI contrast agent with a dual photoacoustic imaging (PAI) capability.

3.2 Positron emission tomography (PET) and Single Photon Emission Tomography (SPECT)

These molecular imaging modalities have been used to study and understand biological function and disorders of living tissue in health and disease. PET and SPECT are widely used for the diagnosis of various diseases, including neurogenerative disorders, cardiovascular diseases and cancer among others. A key component of PET or SPECT is the radiotracer which consists of the biochemical compound of interest labeled with a PET or SPECT radionuclide respectively. PET and SPECT will be disused in details in the following sections.

3.2.1 Positron emission tomography (PET)

The principle of PET imaging is based on the use of radionuclides coupled to chemical compounds to produce radiotracers that decay by positron emission (Table 3). When a radiotracer labeled with a radionuclide, such as Fluorine-18 (^{18}F), or Zirconium-89 (^{89}Zr), is injected into a patient, a PET scanner can detect and track the signal from such radiotracer in different organs and tissues. As an example, the decay schemes of ^{18}F and ^{89}Zr are shown in figure 7, A and B.

Following positron decay, the positron travels a certain distance (determined by their kinetic energy) and collides with a negative electron in tissue. The result of this is the annihilation of both particles and the production of annihilation radiation in the form of two gamma rays with an energy of 511 keV emitted at opposite directions. These photons are detected in coincidence by a PET scanner using opposing pairs of detectors in a ring system. The principle of PET coincidence detection and imaging is illustrated in (Figure 7, C). [111,112]

The activity distribution of the radionuclide represents an image of the tracer distribution/concentration that provides an insight into the physiology and/or pathology in the patient.

Table 3: The characteristics of commonly used PET radionuclides.

Nuclide	Half-life	Decay Modes	Maximum positron energy (MeV) and yield (%)	Production
^{11}C	20.3 min	β^+	0.961 (99.8%)	$^{14}N(p,\alpha)^{11}C$
^{13}N	10 min	β^+	1.20 (99.8%)	$^{16}O(p, \alpha)^{13}N$
^{15}O	2 min	β^+	1.74(99.9%)	$^{15}N(p,n)^{15}O$ $^{14}N(d,n)^{15}O$
^{18}F	109.8 min	EC, β^+	0.634 (96.7%)	$^{18}O(p,n)^{18}F$ $^{20}Ne(d, \alpha)^{18}F$
^{52}Mn	5.6 days	EC, β^+	0.575 (29.6%)	$^{52}Cr(p,n)\ ^{52}Mn$
^{89}Zr	3.27 days	EC, β^+	0.90 (22%)	$^{89}Y(p,n)^{89}Zr$ $^{89}Y(d,2n)^{89}Zr$
^{64}Cu	12.7 hrs	EC, β^+, β^-	0.653 (17.4%)	$^{64}Ni(p,n)^{64}Cu$
^{124}I	4.2 days	EC, β^+	2.14 (23.0%)	$^{124}Te(p,n)^{124}I$

β^+: beta-plus; β^-: beta-minus; EC: Electron Conversion

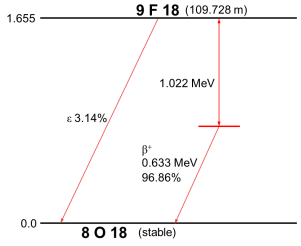

A

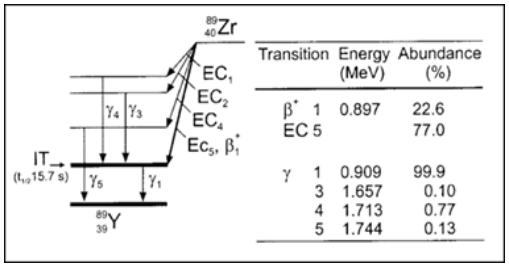

B

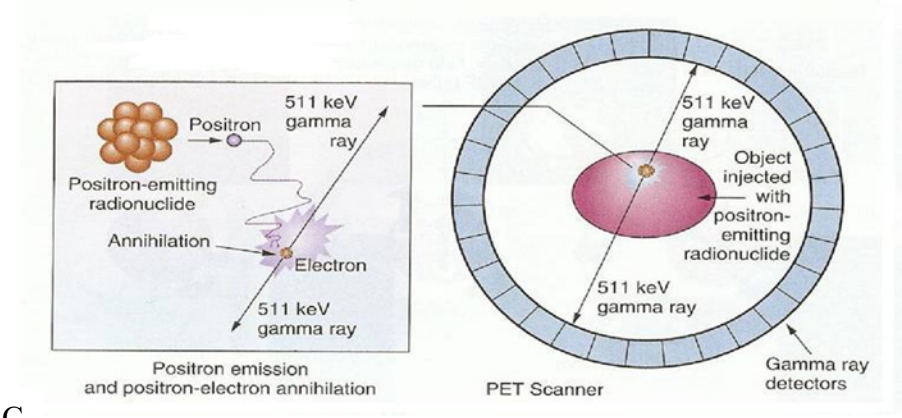

C

Figure 7: A) Decay scheme of Fluorine-18. B) Decay schemes of Zerconium-89. C) Principle of PET imaging: positron emitting radionuclide yields a positron that travels a short distance, before colliding with an electron which results in the annihilation of both particles and the production of two collinear 511 keV photons. These photons exit the body and are detected by an array of scintillation crystals.

3.2.2 Single Photon Emission Tomography (SPECT)

The fundamental basis for SPECT imaging is the detection of mono-energetically emitted γ-rays from intravenously injected exogenous radionuclides (Table 4), ex. Iodine-123 (^{123}I) (Figure8, A) or Technetium-99m (^{99m}Tc) (Figure8, B). Gamma-ray photons emitted from the internal distributed radiopharmaceutical penetrate through the animal's or patient's body are detected by a single or a set of collimated radiation detectors. The collimator defines the angle of incidence of the γ-rays emitted. Most of the detectors used in current SPECT systems are based on multiple sodium iodide (NaI) (TI) scintillation crystal detectors. Upon interaction with the γ-rays, these crystals emit light which is amplified by photomultiplier tubes and converted to electronic signals. 2D images are acquired by rotating the gamma camera at different angles. These are then converted to 3D image data set using tomographic reconstruction algorithms (Figure 8, C). [113]

In SPECT, data are acquired from different views around the animal/patient and physical collimation is used to project the signal emanating from specific field of view. Some of the emitted γ-rays will be absorbed by the lead collimation, and it is because of this, SPECT imaging has a

lower detection efficiency than PET, where electronic collimation is used to detect two coincident γ-rays. Therefore, PET systems have higher sensitivity and higher resolution than SPECT cameras. However, the use of radionuclide generators and medium half-life radionuclides, combined with lower cost of gamma cameras, make SPECT imaging much more widely available for clinical use than PET scanners. [114]

Table 4: The characteristics of SPET radionuclides

Nuclide	Half-life	Decay Modes	Maximum energy (MeV)	Production reaction
^{67}Cu	61.83 hrs	β^-, γ	0.5617	^{68}Zn (γ, p)
^{99m}Tc	6 hrs	g	0.1405	^{99}Mo/^{99m}Tc
^{123}I	13.3 hrs	EC, γ	0.16	^{127}I(p,5n)
^{198}Au	2.7 days	β^-, γ	0.960	^{197}Au (n, γ)
^{111}In	67.9 hrs	EC, γ	0.17/.0.25	^{111}Cd (p,n)
^{153}Gd	240.4 days	EC, γ	0.10	^{152}Gd (n, γ)
^{67}Ga	78.3 hrs	EC, γ	0.09/0.19/0.30	^{68}Zn(p,2n)

β^+: beta-plus, β^-: beta-minus, EC: Electron Conversion, γ: gamma rays

A

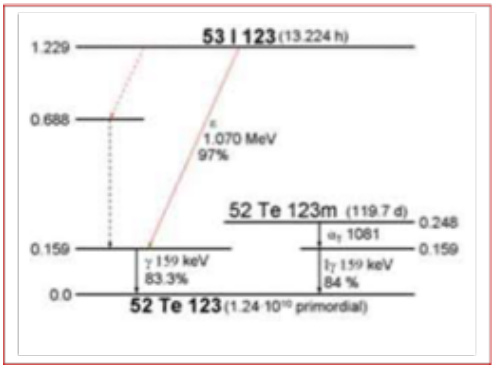

B

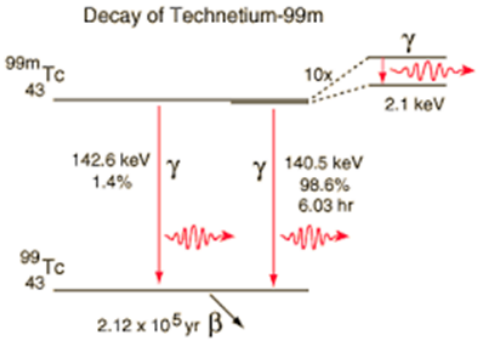

C

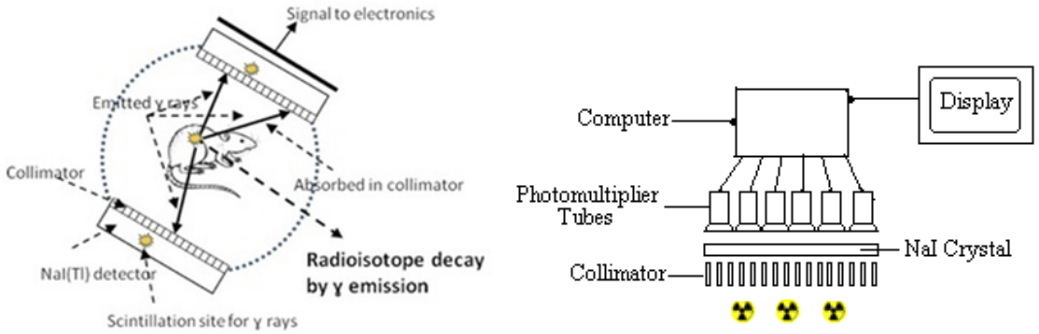

Figure 8: A) Decay scheme for single photon emitting radionuclides Indium-123 (A), and Technetium-99m (B). C) Principle of SPECT imaging.

3.2.3 Radiotracers

Radiotracers are chemical compounds labeled with radionuclides which enable PET and SPECT imaging techniques to be used, non-invasively, to visualize, study and diagnose various disease conditions. Table 5 lists a number of commonly used radiotracers for PET and SPECT. These range from simple thyroid imaging using a ^{99m}Tc-pertechnetate or iodide ion to more complex metabolic and receptor-based radiotracers. For instance, fluorine-18-fluorodeoxyglucose ([^{18}F]-FDG) is used for PET imaging of various cancers because the radiotracer is preferentially taken up by cancer cells due to their greater metabolic activity compared to normal cells.[115,116] Among the recently developed molecularly targeted radiotracers, gallium-68-prostate specific membrane antigen (^{68}Ga-PSMA) has shown high sensitivity and specificity for prostate cancer detection and for monitoring response to therapy because it is taken up by specific membrane antigen over-expressed on the prostate cancer cells.[117,118]

There is a continuous development of radiotracers for molecular imaging, including the exciting combination of radiolabeled nanoparticles with drug nano-delivery systems for multi-modality image-guidance of multiple therapeutics and drug “cocktails”. The introduction of nanotechnology into radiotracer research has opened new possibilities of solid phase chemistry,

microreactors and flow chemistry techniques to synthesis radiotracers.[119] The incorporation of radionuclides, contrast agents and therapeutic drugs has opened up the potential of multi-functional nano-based agents including radiopharmaceuticals for imaging and therapy (theranostics). This thesis is contributing to this effort by the development of a novel multi-modality intrinsically labeled nanoparticle which encompasses an ‘’all in one” platform for multi-modal imaging by PET, SPECT, MRI and photoacoustic imaging.

Table 5: Common radiotracers used in medical imaging

Radiopharmaceutical	**Common clinical use**	**Mechanism of uptake**
Tc-99m pertechnetate or Sodium iodide-123/131 pertechnetate	Thyroid gland imaging	Trapping by Active transport
Tc-99m methylene diphosphonate (^{99m}Tc-MDP)	Bone imaging	Adsorption by hydroxyapatite crystals
Tc-99m macroaggregated albumin particles (^{99m}Tc-MAA)	Lung perfusion imaging	Blockage of capillaries and precapillary arterioles
Tc-99m-(mercaptoacetyltriglycine) ^{99m}Tc-MAG-3	Renal dynamic imaging	Tubular excretion
Tc-99m or In-111 labeled white blood cells and monoclonal antibody	Infection imaging	Cell migration
Fluorine-18 fluorodeoxyglucose ([^{18}F] FDG)	Tumor imaging	Active transport to cells (glucose analog)
Fluorine-18 sodium fluoride ([^{18}F] NaF)	Bone imaging	Ion exchange
Gallium-68-PSMA(^{68}Ga-PSMA)	Prostate cancer imaging	Receptor binding
Gallium-68- octreotide/ edotreotide (^{68}Ga-NOC/TOC)	Neuroendocrine tumor imaging	Receptor binding
Zr-89-labeled monoclonal antibody	Immune PET imaging	Receptor binding

3.3 Optical imaging

Optical imaging is another type of molecular imaging using optical technology non-invasively to visualize and characterize biological processes at the cellular and molecular level. Using non-invasive and non-toxic imaging methods allows researchers and clinicians to study and examine inside the system over the time without any modification or interactions in the tissues or their microenvironments. This real time imaging is important especially for the examination of diseases such as cancer. Deferent types of optical imaging such as florescence imaging, bioluminescence imaging and optoacoustic imaging, use various techniques which depend on illumination light in the ultraviolet, visible and infrared regions of the electromagnetic spectrum. In the florescence imaging, the light illuminates on the subject or tissue within the range of the wavelength between 395-600 nm and the emitted light with wavelength higher than excited wavelength will be detected by charged coupled device (CCD) detectors. Near infrared probes can be used to maximize tissue penetration. In bioluminescence imaging, the emission light only detected by CCD because bioluminescence is a light producing phenomenon which occurs naturally in many species whereas the oxidation of substrate (luciferin) by enzyme (luciferase), photons are released as the substrate returns to its ground state from its excited state. Commonly used probes for bioluminescence are reporter genes such as firefly or renilla luciferase (Fluc or Rluc). Optoacoustic technology principle based on using pulsed laser to excite light on the subject and as a result an ultrasound emitted and detected.[91,120] In this work, MSOT was used for photoacoustic imaging, and will be discussed in detail in the following section.

3.3.1 Multi-spectral optoacoustic tomography (MSOT)

Over the last decade, MSOT has been developed by combining high sensitivity optical detection with high resolution ultrasound imaging.[121] This technology works by using a pulsed

laser light (1-100 nanoseconds) to illuminate tissue or an entity within. The technology can utilize either endogenous compounds such as oxygenated & deoxygenated hemoglobin, and melanin, or use exogenous agents with photoacoustic properties such as imaging probes and nanoparticles.

The principle of MSOT imaging is outlined in figure 9. First, the electromagnetic energy from the laser light is absorbed by a photo-absorber in tissue, and part of this energy is converted to heat. This causes thermo-elastic expansion, a phenomenon known as the optoacoustic or photoacoustic effect, creating a pressure wave that is detected by ultrasound sensors. The detected wave is converted into an image of the initial pressure distribution in the tissue using tomographic inversion methods.[122,123] Image formation can be done by means of hardware (e.g., acoustic focusing or optical focusing) or computed tomography (mathematical image formation). MSOT has the ability to illuminate tissues with various wavelengths, which allows the detection of ultrasound waves emitted by different photo-absorbing molecules. Optoacoustic imaging based on collecting ultrasound waves in the 0.1–10 MHz range achieves a resolution of about 300 microns through 1-3 cm of tissue in the near-infrared (NIR) region, since sound scattering in tissue is orders of magnitude lower than photon scattering. Compared with other conventional optical imaging techniques, MSOT is not affected by photon scattering and as a result of this, high-resolution optical images in reasonably deep biological tissues will be obtained.[122] MSOT biological applications include studies in cardiovascular disease research, neuroimaging, and cancer research, among others.[124–127] In addition, prototype clinical use of MSOT for imaging the breast, vasculature, lymph nodes and skin, by real-time handheld imaging systems, has been recently demonstrated.[128,129]

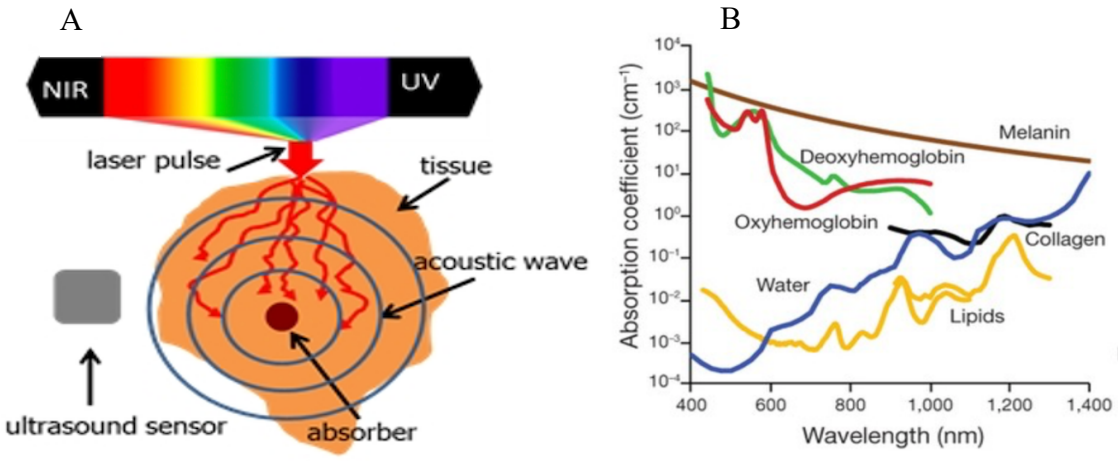

Figure 9: A) Principle of MSOT operation. Illuminating the tissue at multiple wavelengths can stimulate ultrasound wave emission by several photo-absorbers, leading to more informative imaging than single-wavelength illumination. B) A number of endogenous compounds has different absorption coefficient that compatible with MSOT.

3.3.2 MSOT contrast agents

Light absorbing molecules capable of converting light to a pressure wave have the potential to be detected leading to the formation of an optoacoustic signal. Contrast agents absorbing light in the NIR are particularly attractive, because the high wavelength in the NIR region enables imaging at greater depth. Contrast agents with this feature help to expand the range of MSOT imaging applications. Contrast agents can either be endogenous, that is light absorbing molecules, which are naturally present in animal or humans, or they can be exogenous compounds administered to the subject.

3.3.2.1 Endogenous contrast agents

A number of endogenous compounds have different absorption coefficients that are compatible with MSOT shown in figure 9, B. One of the most commonly used endogenous contrast agents for optoacoustic imaging is hemoglobin which is a dominate absorber of light in the visible and NIR of the optical spectra. Hemoglobin, as a contrast agent allows sensitive imaging of

vascular anatomy at various levels. Furthermore, MSOT has multispectral capability that allows differentiation between oxygenated versus de-oxygenated hemoglobin. This is a unique tool which can assess tissue oxygenation level and hypoxia (reduced oxygen), hence providing a functional measure of oxygen status in normal and pathological physiology. Many useful applications for using hemoglobin-based imaging, such as resolve vascular abnormalities and oxygenation status, as well as perfusion imaging, inflammation imaging, and tumor detection and characterization.[123,130] Another endogenous contrast agent is melanin, which has the ability to absorb over abroad range of the wavelength in the visible and NIR and the absorption decreases with higher wavelength. There are different uses of melanin based optoacoustic imaging such as to assess the depth of melanoma ingrowth inside epithelial tissue, and to assess the metastatic status of sentinel lymph nodes in melanoma patients, also to detect circulating melanoma cells.[131] More endogenous absorbers can be detected by MSOT. For example, lipids which can be imaged at NIR wavelengths with absorption peak of 930 nm, and water which has strong absorption at NIR wavelengths and higher peak at 980 nm. Bilirubin and cytochromes can be imaged at blue wavelengths. DNA absorbs UV which is exploited to image cell nuclei.[132,133]

3.3.2.2 Exogenous contrast agents

A large numbers of exogenous contrast agents have been developed and are under development for optoacoustic imaging, examples of imaging probes have been reported in table 6. The absorption spectrum for these contrast agents is different from that of endogenous ones and this makes them easily separated from other background absorbers using spectral unmixing. Organic dyes, such as the fluorochromes indocyanine green and methylene blue, are non-specific, approved for clinical use, and suitable for perfusion imaging. Another type already in clinical use for photodynamic therapy is photosensitizers which can be detected using MSOT and allowing

analysis of their pharmacokinetics and biodistribution *in vivo*.[134] Light-absorbing nanoparticles are another exogenous contrast agent, and because of their lower photosensitivity and ability to produce stronger photo-echoes, they offer potential advantages over organic dyes. Gold nanoparticles, silver nanoparticles, carbon nanotubes, and iron-oxide particles have been used for optoacoustic imaging in animals. Gold nanoparticles have the ability to produce strong optoacoustic signals due to plasmon resonance and their absorption spectrum can be adjusted by modifying their shape. Nanoparticle or dye can be combined with a targeting ligand to form MSOT targeted contrast agents and used for a specific tissue which expressed specific cellular molecules.[135] For instance, MSOT imaging of integrins within tumor animals, and image matrix metalloproteinase (MMP) activity within thyroid tumors in mice.[136,137] Another powerful tool which is already widely used in biomedical research and can also be visualized by MSOT is fluorescent proteins. Green fluorescent protein and red fluorescent protein are examples of that.[138]

Table 6: Examples of optoacoustic imaging probes and their characterizations[139]

Probe	**Type**	**Size (nm)**	**Absorption peak (nm)**	**Imaging target(s)**
Green fluorescent protein (GFP)	Genetically engineered chromophore (GEC)	NA	488	Drosophila Pupa
LacZ (produced by transgene)	GEC	NA	605-665	Tumor
Melanin (produced by tyrosinase transgene)	GEC	NA	680-800	Lymph nodes and tumor
Indocyanine Green (ICG)	NIR- Fluorescent dye FD	<2	790	Brain, lymph nodes, tumor
IRDye800cw	NIR-FD	<2	774	Tumor
Methylene blue	NIR-FD	<2	670	Lymph nodes and tumor
Polypyrrole	Polymeric nanostructures (NS)	≈50	800	Brain and deep tissue
Porphysome	Polymeric-NS	≈100	400, 680	Lymph nodes
Conjugated polymers	Polymeric-NS	50-200	Depends on composition	Vasculature and tumor
Gold nanorods	Inorganic NP	100–1000	600-1100	Tumor and lymph nodes
Gold nanoclusters	Inorganic NP	50-100	500-600	Tumor
Copper sulfide	Inorganic NP	≈20	900-1000	Tumor
Iron oxide	Inorganic NP	10–200	500-800	Tumor

Single-walled carbon nanotubes	Inorganic NP	5-8	600-1100	Tumor and lymph nodes
Graphene oxide	Inorganic NP	≈10	500-900	Tumor
Quantum dots	Inorganic NP	5-50	630	Cells and lymph nodes

The CuS NP platform described in this work has been conceptually developed as a multi-modality theranostic nano-platform which can accommodate a radioisotope and a magnetic element, in addition to the CuS core with photoacoustic capability. This "all in one" platform can be used as a single modality probe or as a combination of two or more modalities. By inserting a radioisotope into the core/shell of NP, quantitative *in vivo* imaging and biodistribution analysis can be accomplished by either PET or SPECT. Such a tool would provide robust pharmacokinetic data and would also validate the performance of the NP imaging signal from the other modalities, namely photoacoustic (PA) and MR imaging.

Chapter 4: Materials and Methods

4.1 Chemicals and suppliers

All chemical reagents involved in this work, including cell culture were used without further modification unless it is stated in the text. Copper Chloride ($CuCl_2$), Manganese Chloride ($MnCl_2.4H_2O$), Sodium Sulfide ($Na_2S.9H_2O$), Poly (acrylic acid) (PAA, M_W =1800), Thiol Polyethylene glycol Amine (HS-PEG2K-NH_2), Methoxypolyethylene glycol (MPEG), Bovine serum albumin (BSA), Succinimidyl 4-(N-maleimidomethyl) cyclohexane-1-carboxylate (Sulfo-SMCC), N-(3-dimethylaminopropyl)-N′-ethylcarbodiimide hydrochloride (EDC), N-hydroxysuccinimide (NHS), and Cyclo (Arg-Ala-Asp-D-Phe-Lys) peptide (cRGD). All stoke solutions, nanoparticle synthesis and purification were prepared by using nano pure water (18MΩ).

4.2 Cell lines and cell culture

The cell lines were used in this project were human lung carcinoma (A549), human colon cancer cell (HCT116), human brain glioblastoma astrocytoma (U87-MG), human colon carcinoma (COLO-205) and breast cancer cell lines (MDA-MB-435) and were obtained from American Type Culture Collection (ATCC). Cell lines were maintained in humidified incubator at 37 °C and 5% CO_2. Briefly, cells were grown in Dulbecco's Modified Eagle's Medium (DMEM)/High glucose medium supplemented with 10% fetal bovine serum (FBS), 5mM L-Glutamine, Penicillin (100U/ml), Streptomycin (100µg/ml) and Amphotericin B (0.25 µg/ml). The cells were grown to 80 – 90 % confluency before they were used. Trypsin was used to detach the cells, and then cells were resuspended in the media. Cells were counted by using a Neubauer chamber and the exact number used for *in vitro* experiments and implantation in animals.

4.3 Animal tumor models

All animal experiments were performed according to the policies and guidelines of the Animal Care and Use Committee (IACUC) at Virginia Commonwealth University. Female athymic nude mice and CD-1 mice were aged 4-6 weeks were obtained from Charles River Laboratories. For the tumor mice model, $5X10^6$ cells were inoculated subcutaneously into the shoulder-side (Right and Left) of the mouse. Mice were monitored and tumor growth was measured by using digital caliper every three days. Tumors developed within 8-10 weeks.

4.4 Synthesis of Intrinsically Radio-labeled CuS-Mn NPs

Overview: To develop the synthesis procedure for multimodality NPs. First, a non-radiolabeled Mn doped CuS NPs were synthesized and coated with different coating small molecules or polymers to develop the chemistry of synthesis. Second, ^{89}Zr was incorporated with CuS-Mn NPs to develop the chemical process of intrinsically radiolabeled NPs. Another radionuclide was used for radiolabeling which is ^{67}Cu. ^{67}Cu was used for incorporation with CuS-Mn NPs to develop [^{67}Cu]-CuS-Mn NP. The following sections describe the development of small NPs, composed of CuS core, which was doped with radionuclides ($^{89}Zr/^{67}Cu$) and paramagnetic (e.g., Mn) elements, to enable MR, PET, SPECT and PA imaging in one platform (Figure 10).

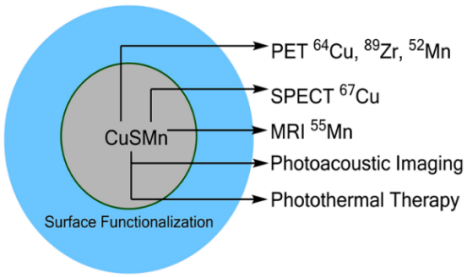

Figure 10: Concept and synthetic strategy of multi-label CuS-Mn NPs

Different approaches have been used to synthesize CuS NPs. Hydrothermal/solvent methods, sono-chemical synthesis, microwave irradiation methods and co-precipitation method are generally used to prepare nanostructure.[77,140] The synthesis of CuS NP and Mn doped CuS-Mn NP was done by hydrothermal reaction, without complexity and at lower temperature. A two-step synthesis involving the reactants, copper (II) chloride ($CuCl_2$), manganese chloride ($MnCl_2.4H_2O$), sodium sulfide $Na_2S.9H_2O$, and different coating material were used including alginic acid, poly (acrylic acid), citric acid, sodium citrate, and polyethylene glycol (PEG). ^{89}Zr or ^{67}Cu were used for intrinsically radiolabeling the NP. ^{89}Zr is produced by proton irradiation of a natural yttrium target on a PET-Trace Cyclotron by IBA Molecular (Richmond, VA, USA). ^{89}Zr activity separated from the target using ion exchange chromatography to produce ^{89}Zr-oxalate in a solution of 1M oxalate. ^{67}Cu is produced by a photonuclear reaction from Zinc-68 (^{68}Zn) at Argonne National Laboratory (ANL) and received in the form of $^{67}CuCl_2$. Due to its medium energy beta particle, gamma emissions and 2.6 days half-life, ^{67}Cu is useful isotope can be used for therapy and diagnosis[141].

4.4.1 Synthesis of non-radiolabeled CuS NPs and CuS-Mn NPs

The synthesis of non-radiolabeled CuS NPs and CuS-Mn NPs was done as following:

1- $CuCl_2$ (13.4mg, 0.1 mmole), $MnCl_2.H_2O$ (3.4mg, 0.005-0.05 mmole) which was added only to the CuS-Mn NP synthesis and not in CuS NP synthesis, under the existence of organic polymers (25mg) was dissolved in 100 ml of nano-pure water.

2- In another tube, $Na_2S.H_2O$ (28.8 mg, 0.12 mmole) was dissolved in 1ml of nano-pure water.

3- A 100 µl from Na_2S solution was added to 10 ml of $CuCl_2/MnCl_2$ and organic polymer solution, dropwise and stirred for 5 min at room temperature, to form CuS-Mn core,

followed by heating the reaction mixture to 90° C for 30 min to grow nanoparticles, which changed color from brown to green color.

4- The obtained NPs dissolved in water and were purified by using a 3KDa molecular weight cut-off centrifugal filter (MWCO) by centrifugation spin at 4750 rpm for 30 minutes.

5- The NPs size and surface properties can be manipulated by adjust the reaction conditions.

6- Organic polymers were used for CuS-Mn NPs synthesis, for instance: poly (acrylic acid) (PAA), sodium citrate, alginic acid, ascorbic acid and polyethylene glycol (PEG).

7- Stability of nanoparticles, hydrodynamic size, toxicity and biodistribution depends on the surface coating. An outline of the synthesis of coated CuS NP and CuS-Mn NPs shown in figure 11 and 12.

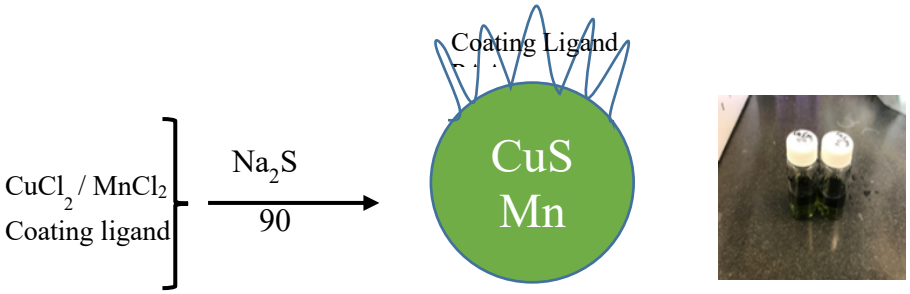

Figure 11: Schematic for the synthesis of CuS-Mn NPs

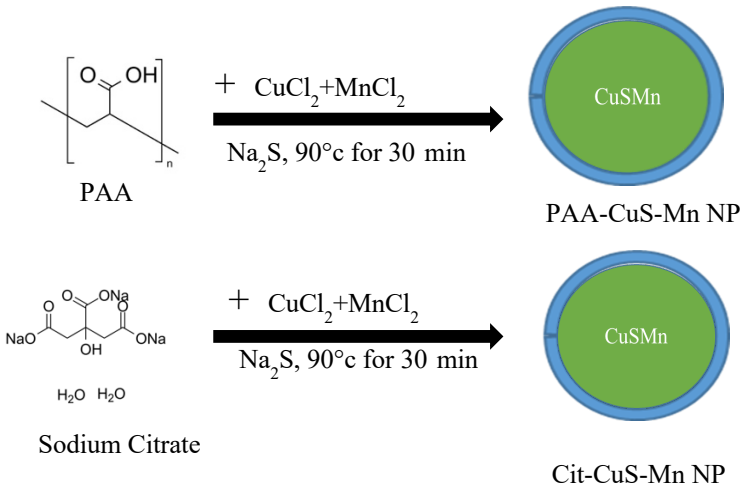

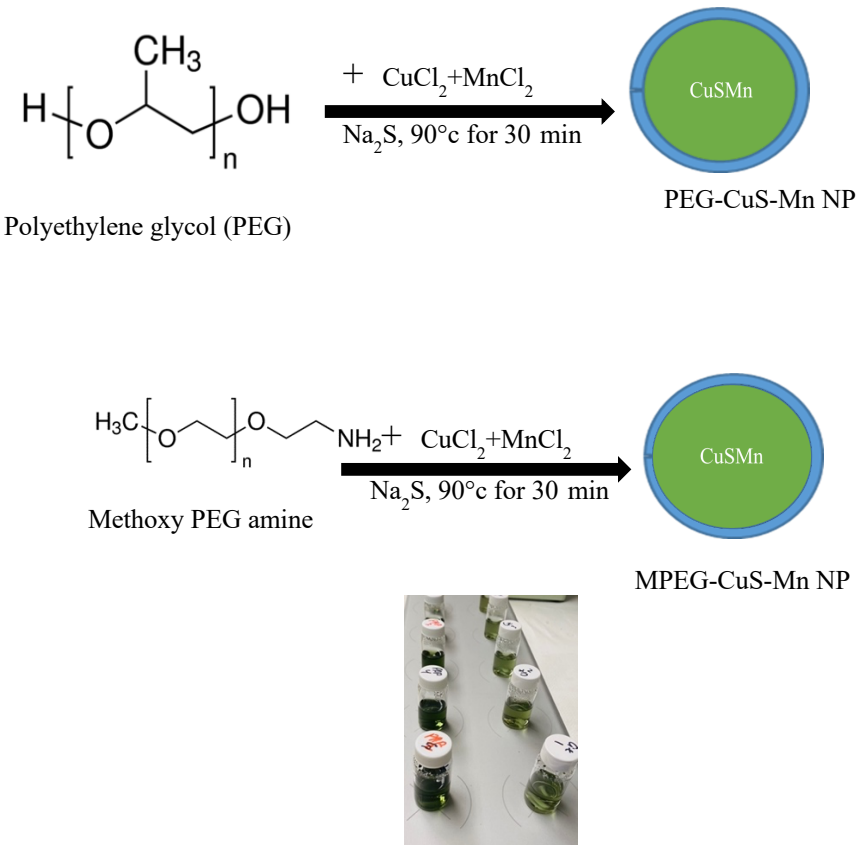

Figure 12: Synthesis scheme and image for coated CuS-Mn NPs. Different coated material was used to synthesis CuS-Mn NP by adding polymers or small molecules to the reaction mixture including PAA, PEG, sodium citrate and alginic acid.

4.4.2 Synthesis of intrinsic radiolabeling ^{89}Zr labeled CuS-Mn NPs

In order to enable PET imaging, CuS-Mn NP was incorporated with Zirconium-89 (^{89}Zr). ^{89}Zr is an increasingly used radionuclide in PET imaging, particularly for radiolabeled antibodies investigated for immunotherapy.[142] This is because it has medium half-life, 3.27 days, which is compatible with *in vivo* kinetics of macromolecules. The cyclotron produced ^{89}Zr is in the form of zirconium oxalate (^{89}Zr-Oxalate), and in order to intrinsically introduce ^{89}Zr in the CuS-Mn NPs it needs to be converted to zirconium chloride $^{89}ZrCl_4$ in 1M hydrochloric acid (HCl). This was done as follows:

$^{89}ZrCl_4$ preparation

1- Sep-pak Light QMA strong anion exchange column (Waters, Inc.) was pre-washed with 6 mL acetonitrile, 10 mL 0.9% saline, and 10 mL nano-pure water.

2- The ^{89}Zr-Oxalate was loaded onto the cartridge and then rinsed with 40 mL nano-pure water.

3- The ^{89}Zr activity is retained in the column and oxalate is washed out by the water.

4- The ^{89}Zr is eluted by 1mL 1M HCl and fractions are collected, with the highest activity fractions combined and used for subsequent reactions.

Preparation of ^{89}Zr labeled CuS-Mn NPs

The synthesis scheme of ^{89}Zr labeled CuS Mn NPs is shown in figure 13, and the synthesis procedure was done as follow:

1- $CuCl_2$ (13.4mg, 0.1 mmole), $MnCl_2.H_2O$ (3.4mg, 0.02 mmole) under existence of organic polymers (25mg) was dissolved in 100 ml of nano-pure water.

2- For radiolabeling with ^{89}Zr, a 100 µl of $^{89}ZrCl_4$ (100 µCi - 940 µCi) was added to $CuCl_2/MnCl_2$ solution before starting reaction to incorporate ^{89}Zr in core NPs.

3- In another tube, $Na_2S.H_2O$ (28.8 mg, 0.12 mmole) dissolved in 1ml of nano-pure water.

4- A 100 µl from Na_2S was added to 10 ml of $CuCl_2/MnCl_2$ and organic polymer (PAA) solution, dropwise and stirred for 5 min at room temperature, to form CuS-Mn core, followed by heating the reaction mixture to 90° C for 30 min to grow nanoparticles, which changed color from brow to green.

5- The obtained ^{89}Zr labeled CuS-Mn NPs dissolved in water and were purified by using a 3KDa MWCO by centrifugation spin at 4750 rpm for 30 minutes.

6- This was repeated three times to remove non-NP ^{89}Zr associated activity, which passes through the MWCO filter. This purification ensures that all radioactivity remaining is in the core of the nanoparticle.

7- The NPs size and surface properties can be manipulated by adjust the reaction conditions. Organic polymers PAA was used for coating [^{89}Zr]-CuS-Mn NPs because it resulted of smaller size NP.

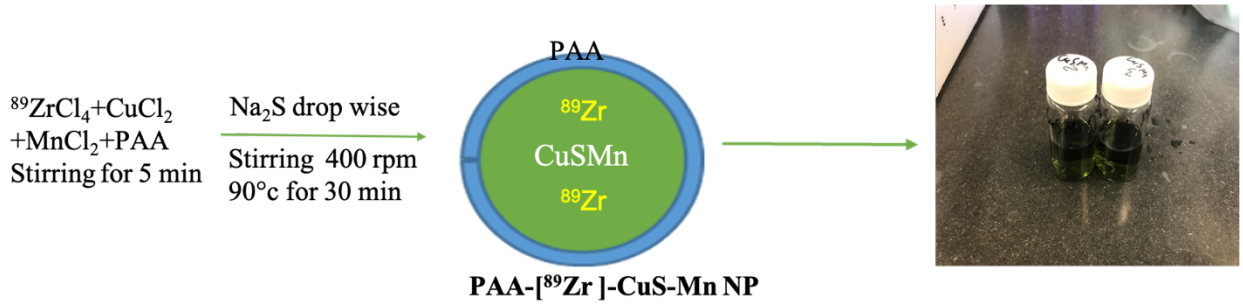

Figure 13: Synthesis scheme for ^{89}Zr labeled CuS-Mn NPs. $^{89}ZrCl_4$ was added to the synthesis to incorporate ^{89}Zr into the CuS-Mn NP. PAA coated material was used to synthesis CuS-Mn NP.

4.5 Characterization of CuS-Mn NPs

The produced CuS-Mn NPs needs to be characterized to determine concentration, size and surface charge using different methods such as an Ultraviolet-visible (UV-Vis) absorption spectrum, dynamic light scattering (DLS), zeta potential (ZP) measurement, transmission electron microscope (TEM) and inductively couple plasma – optical emission spectrometry (ICP-OES). For radioactive yields, a dose calibrator to measure the activity was used during radiosynthesis and at the end of the synthesis.

4.5.1 Absorption spectra of CuS-Mn NPs

The effect of surface coating and content of manganese on the absorption of CuS-Mn NPs were studied and the plots showing the absorbance VS wavelength range from (400-1100) analyzed by using an UV spectrum to see the effect of Mn concentration and surface coating. The nanoparticles were diluted in water (1:2), and plain water was used as a blank. The absorption

spectra of CuS NP and CuS-Mn NP were recorded by using the DU 730 spectrophotometer which is a complete scanning UV-Vis spectrophotometer with a bandwidth of 3 nm and a wavelength range of 190 to 1100 nm.

4.5.2 Hydrodynamic size and zeta potential measurement of CuS NPs and CuS-Mn NPs

The coating and doping Mn into CuS NPs changes its size and charge, so it is important to determine the size and charge of the NPs. The hydrodynamic size (HD) of the nanoparticles was measured by dynamic light scattering (DLS) using a Zeta Sizer Nano Series ZEN3600 (Malvern, USA). The HD size of the CuS-Mn NP represents core/shell size. When the NP is coated with a ligand, then the HD size is representative of the whole coated NP. DLS measures the diffraction of light by particles in a solution, which fluctuate in a manner correlated to the particle size. The diffraction can be analyzed by the system to determine the size distribution of the particles. This method is able to determine size as small as 1-5 nm. The samples of CuS NPs, CuS-Mn with 10% and 20% Mn concentration were diluted (1:2) with water and sonicated for 30 minutes before the measurement.

The zeta potential is the electro-kinetic potential between the surface of nanoparticle coating and the dispersion medium. This potential was also calculated with the Zeta Sizer Nano Series ZEN3600, by measuring the effect of an external electric field on the nanoparticle motion.

4.5.3 Transmission electron microscope (TEM) for CuS-Mn NPs

The TEM analysis was carried out on CuS-Mn NPs. The size and morphology of synthesized CuS-Mn NPs were investigated by EOL JEM-1400 Plus transmission electron microscope (JEOL USA INC, Peabody, MA, USA) at an accelerating voltage of 120 kV. Images were taken by a Gatan OneView camera (Gatan Inc., Warrendale, PA. USA). The steps of this process are described below:

1- First CuS-Mn NPs samples were diluted (1:5) in water and one drop was taken on copper grids coated with carbon film. The samples of CuS-Mn NPs were left to dry for overnight.

2-The scale of the image was defined in the software by matching a scale line to the scale bar in the TEM image.

3-The background of the image was removed by subtracting a Gaussian blur filter image with a radius much larger than the nano-particle size (usually 150 nm).

4-The threshold of the image was adjusted to give high nanoparticle contrast and sharp edges.

5-The 'analyze particles' tool was used to measure the area of the particles in the image. Around 300 nanoparticles were analyzed.

4.5.4 Concentration and radioactive yield

In order to determine the concentration of CuS-Mn NPs in solution, the inductively couple plasma – optical emission spectrometry (ICP-OES) was used to measure the concentration of Cu and Mn. ICP-OES was also used for testing the doping of Mn in the CuS-Mn NPs. For radioactive yield, a dose calibrator was used.

4.5.4.1 Inductively couple plasma – optical emission spectrometry (ICP-OES)

ICP-OES is an analytical system used to determine how much trace metal is in the sample. The principle of ICP-OES depends on the fact that absorption of energy by the atoms and ions to move electrons from the ground state to an excited state. The source of energy is argon plasma that operate at 10,000 kelvin, which used to ionize the metal atoms in a liquid sample (nitric acid). Those excited atoms as they are transition to a lower energy, the photons produced at specific wavelengths that can be detected by photomultiplier tubes. The amount of light given off from the sample is proportional to the concentration of the metal in solution. This method can detect metals

as low as 2 parts per billion (ppb) (2 ng/mL). Agilent 5110 ICP-OES system was used for the measurement.

Copper and manganese standards were prepared, and 7% nitric acid was used as a diluent solution and ranged in concentration from 0.1, 0.5, 1.0, 5.0, 10, 20, 30 and 40 parts per million (ppm) and showed linear response across that range and a standard curve was produced from the results of the Cu and Mn standards, as seen in (Figure 14; A, B)**.** The samples were prepared by adding a volume (100 µL) of CuS-Mn NPs from the stock solution to 10mL 7% nitric acid solution, expected to create a concentration within the range of the standards. The nitric acid dissolves the CuS-Mn NPs, producing free ions of Cu and Mn in solution which can be detected.

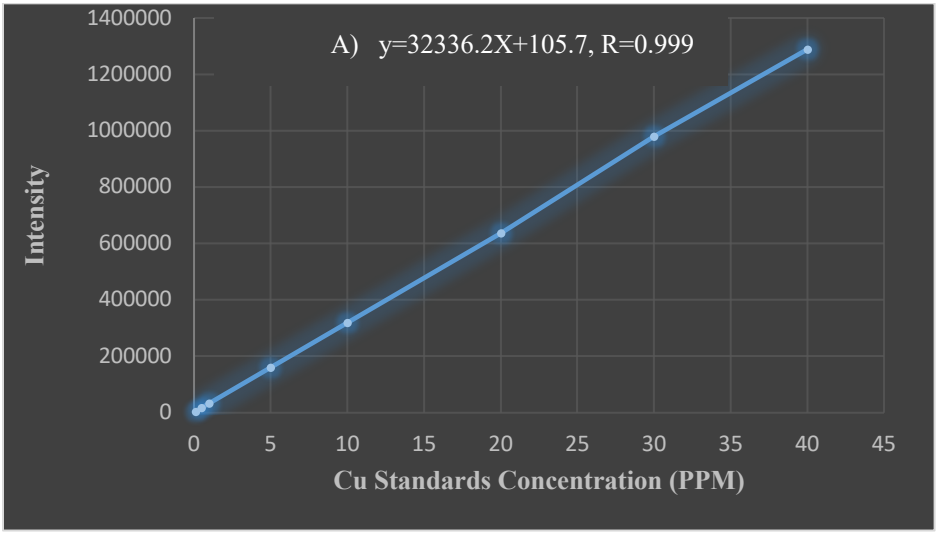

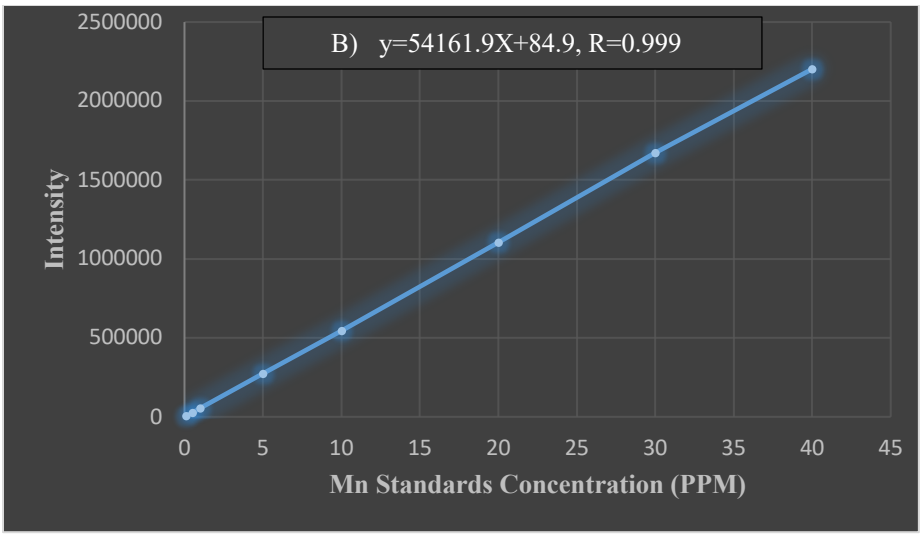

Figure 14: Inductively couple plasma – optical emission spectrometry (ICP-OES) calibration curves of Copper (A) and Manganese (B) standards show good response across a wide range of concentrations (0.1-40 PPM). Samples concentrations within this range were measured.

4.5.4.2 Radiochemical yield

A capintec CRC-15 PET chamber-based dose calibrator was used to measure ^{89}Zr incorporation into CuS-Mn NPs. The measurement was taken during and at the end of radiosynthesis of [^{89}Zr]-CuS-Mn NPs to determine the yield and monitor the decrease of radioactive yield.

4.6 Stability of [^{89}Zr]-CuS-Mn NP

The purpose of radiolabeling CuS-Mn NP is to be used for *in vivo* biodistribution study. So before injecting the [^{89}Zr]-CuS-Mn NP it is important to ensure that the radioactive signal is represent the radiolabeled NP and continue even post injection *in vivo* within period of time. The MWCO filter was used for purification of the NP three times to remove unreacted ^{89}Zr which pass through the MWCO filter from the solution, and this indicate all the radioactivity still remining in the nanoparticle core. To study stability of [^{89}Zr]-CuS-Mn NP after the synthesis, Reversed phase high-performance liquid chromatography (RP-HPLC) (Bio-scan, Model B-FC-3300) was used.

The PAA-[^{89}Zr]-CuS-Mn NPs samples were incubated in three different types of media, in water solution, in *ex vivo* plasma for 24 hrs, and in urine sample collected 2hrs post injection of mice. The samples were injected into RP-HPLC, and 8 x 300 mm, 200 Å Diol (YMC, Japan) size-exclusion column was used. A 20 µL of sample solutions were injected into the HPLC with DI water as the mobile phase and a flow rate of 1 mL/min.

4.7 MRI Performance of CuS-Mn NP

Overview: In order to enhance contrast in MRI images, paramagnetic compounds, with a large number of unpaired electrons, such as gadolinium (Gd)-based compounds, are used as contrast agents because they can shorten the longitudinal relaxation time (T1) and the transverse relaxation time (T2). However, safety concerns limit the use of Gd-based contrast agents (GBCA). The transition metal ion manganese (Mn2+), with five unpaired electrons, can produce a very efficient positive contrast enhancement and offers an attractive alternative to GBCA. In fact, Manganese chloride ($MnCl_2$) has been approved by the FDA as a T1 contrast agent. The performance of CuS-Mn NPs as a contrast agent was studied in comparison to $MnCl_2$. The toxicity of CuS-Mn NPs is significantly lower due to reduced Mn concentration with retention of MR signal. Furthermore, Cu and Mn are less toxic elements than Gd and are biologically compatible.

4.7.1 MRI relaxivity study of CuS-Mn NP

The MRI performance of CuS-Mn NPs was done in comparison to $MnCl_2$ contrast agent. In order to determine the relationship between MR signal intensity as a functional of different concentration of both $MnCl_2$ and CuS-Mn NPs, a phantom study was done.

Methodology: $MnCl_2$ and CuS-Mn NPs was prepared in Mn concentrations ranging from (0.0 mM (Water), 0.0081mM, 0.0163mM, 0.0327mM, 0.0675mM, 0.135mM, 0.27mM and 0.54 mM). The samples loaded in a 1ml syringe and sealed using para film on both ends (Phantom samples, Figure

15). Each syringe labeled with the corresponding concentration. Each syringe (phantom) arranged and taped together to make one bundle and loaded in the cradle within MRI scanner and 72mm transmit/receive coil was used. The MR protocol with this coil results in both T1 and T2 images. The MRI T1 and T2 signal intensity as a functional of concentration of CuS-Mn NPs and $MnCl_2$ was calculated. MRI images of phantom for both CuS-Mn NPs and $MnCl_2$ were taken. This phantom was imaged by using Bruker 7T Bio spec. 70/30 small animal MRI scanner, with multiple slice multiple echo (MSME) sequence which produce phantom image.

Figure 15: Phantom samples of $MnCl_2$ and CuS-Mn NP. Mn concentration was in the range from 0.0mM-0.54mM.

Relaxivity calculation

1. T1 calculation: An inversion recovery pulse sequence with variable inversion time was used to image the samples. Then, the region of interest (ROI) was drawn on each image to find the signal intensity. The signal intensity of each concentration was plotted as a function of inversion time. The recovery curve was then fitted into the inversion recovery equation, to yield the T1 value. The inversion of the T1, for all the concentrations, gives the relaxation rate (R1=1/T1). The R1 values were plotted, as a function of concentration. The slope of the straight-line fit equation gives the relaxivity value, r1.

2. T2 calculation: A spin-echo equation with a variable echo time was used for the same samples above as above. The signal intensity for all the concentrations was measured as a function of echo time, which is an exponential decay curve. This was then fitted to the exponential decay equation to give the T2 value. The inversion of T2 is R2 (R2=1/T2). The R2 values were plotted, as a function of concentration, and the slope of the straight-line fit gives the relaxivity value, r2.

4.7.2 *In vivo* MRI with CuS-Mn NP

The purpose of this experiment to evaluate the performance of CuS-Mn NPs in an *in vivo* setting which is a live animal. Before imaging, the animal was anesthetized using 2% isoflurane at room temperature until stable vital signs were established. Once the animal was sedated, it was placed onto the imaging bed under mixtures of 2% isoflurane and O_2 (1 mL/min) for the duration of the imaging. The pre-injection MR images for mouse kidney and liver were taken and then mouse was received intravenous (iv) injection (tail vein) with 200 µl of CuS-Mn NPs and images for mouse kidneys and liver were taken 2 hours post injection.

4.8 Photoacoustic imaging of CuS-Mn by using (MSOT)

The CuS-Mn NP was also evaluated in terms of its photoacoustic performance *in vitro* and *in vivo*. The CuS NP has unique properties which is the ability to absorb NIR which results an efficient NIR and photoacoustic signal. In this study, the PA performance need to be demonstrated using MSOT. Both phantom and animal studies were conducted to test the merit of the NP performance as a PA agent.

4.8.1 MSOT signal as a function of CuS-Mn NP concentration

In order to determine the relationship between photoacoustic signal and NP concentration. Such measurements determine the sensitivity of detection. To demonstrate this, a phantom study

was carried out whereby various concentration of the CuS-Mn NPs were used and the intensity (PA signal) of each concentration was calculated. CuS-Mn NP was prepared in the concentration range 0 µg/ml to 100 µg/ml in water. The samples were placed in the phantom as shown in figure 16 and imaged in MSOT.

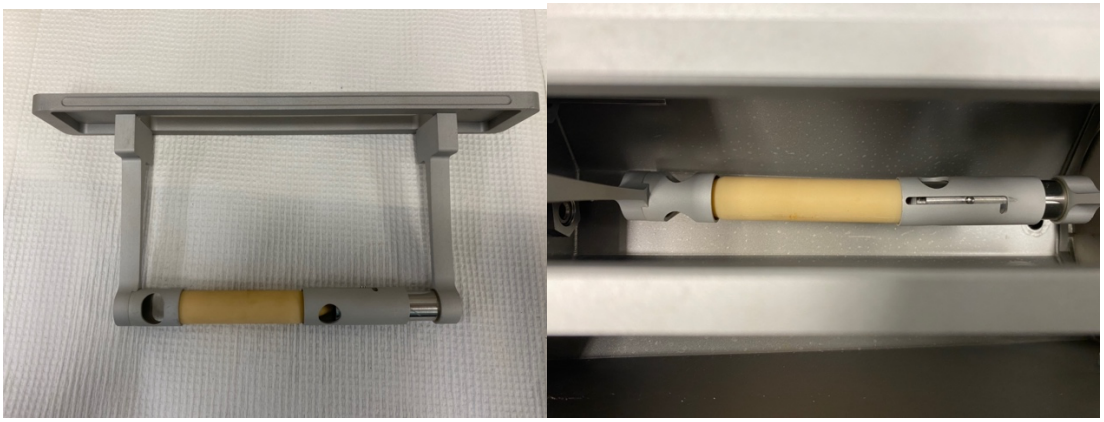

Figure 16: Agar phantom after prepared and loaded in the MSOT

Agar phantoms for MSOT imaging:

Phantoms were used to characterize injectable contrast agent in controlled setting. The sensitivity and linearity of an optoacoustic system can be determined by using of phantoms. There are various properties of phantoms, such as size, composition and their resulting absorption and scattering properties. Agar phantom was made shortly before use and the preparation method was used as follows:

1- A 20 ml syringe was used, and the front part cut off by using a scalpel, with an internal diameter of 2 cm.

2- Intralipid (Sigma I141-100mL), 1.03 ml was heated in hot water bath.

3- To 0.75 g of Agar (Fluka, 05039-500g), a 50 ml of dH_2O was added, and heated in microwave until it boils.

4- The agar was taken out of the microwave and immediately added to the hot intralipid and shake gently.

5- A 15 ml of this mixture poured into a plastic adapted (distal part of cut off) syringe which having a diameter of 2 cm. Then, immediately two 3 mm diameter straws were placed in the syringe and was hold in position using tape. Then, cooled at room temperature for 30 minutes.

The agar phantom can be stored in the fridge in sealed container with some dH2O to keep moist. However, the optical properties of the agar phantom change over time, so it is recommended to be used on the same day.

MSOT image acquisition: MSOT images were acquired multispectral according to the protocol for CuS-Mn NP (wavelengths, 700-900 nm). After image reconstruction, images corresponding to different wavelengths were weighted with the internal laser energy values.

4.8.2 CuS-Mn NP Photoacoustic Imaging *in vivo*

In addition to evaluation in a phantom, the CuS-Mn NPs were also investigated *in vivo.*

Method: An initial baseline image was taken prior to NP administration in order to compare the PA signal to that after injection. Mice were injected with 200 µl of CuS-Mn NPs (≈20µg/ml), and images were taken 1 hr, 5 hrs and 24 hrs post injection.

4.8.3 *Ex vivo* Biodistribution of CuS-Mn NPs using ICP

CuS-Mn NPs was used for *ex vivo* biodistribution study and *in vivo* stability. Inductively coupled plasma mass spectrometry (ICP-MS) was used to measure Cu and Mn in the tissues.

Methodology: three mice were received iv injection of a 200 µl of CuS-Mn NPs and then 24 hrs post injection following MSOT imaging, mice were dissected, blood, major organs, and tumor

were collected and prepared for ICP-MS measurements. The tissues need to be digested before ICP-MS measurements, and this was done as follows:

1- The tissues were placed in a 10 mL tube, and 1mL of concentrated (70%) nitric acid was added.

2- Tissues were allowed to be dissolved at room temperature for 24-48 hours.

3- Then, 9 ml of nano-pure water was added, and total volume became 10 ml.

4- The solution was filtered through a 0.25um filter. The final solution concentration was 7% nitric acid.

5- Standards for Mn and Cu was made at concentrations from 0.1 PPM - 40 PPM as explained on section 4.2.4.1.

6- ICP-MS was used to measure Mn and Cu, because it is sensitive enough for the low concentration in tissue.

4.9 *In vivo* PET imaging of [^{89}Zr]-CuS-Mn NP

Biodistribution of [^{89}Zr]-CuS-Mn NP was determined by PET imaging. Mice PET imaging studies were performed using a Multimodality PET/CT system (Siemens Medical Solutions Inc., Knoxville, TN, USA). Ten minutes prior to imaging, the animals were anesthetized using 2% isoflurane at room temperature until stable vital signs were established. Once the animal was sedated, it was placed onto the imaging bed under mixtures of O_2 (1 mL/min) and 2% isoflurane for the duration of the imaging. [^{89}Zr]-CuS-Mn NPs (200µl, ≈320 µCi) was injected intravenously in a nude mouse via the tail vein. Immediately following the injection, imaging was performed at 30 min, 2hrs, and 24hrs post injection. PET images were reconstructed using Fourier Re-binning and Ordered Subsets Expectation Maximization (OSEM) 3D algorithm with dynamic framing

every 60 seconds. Reconstructed images were analyzed using Inveon® Research Workplace (IRW) software.

4.9.1 Biodistribution of PAA coated [^{89}Zr]-CuS-Mn NPs in nude mice

Mice were injected with [^{89}Zr]-CuS-Mn (200µl, ≈320 µCi). Mice then were dissected at different time points post injection (30min, 2hr and 24hrs). Following animal dissections, organs, including blood were collected. Radioactivity of each sample was measured by gamma counter. The percentage of the injected dose per gram (%ID/g) of tissues was calculated based on the total injected dose and organ weights. The resulting quantitative data were expressed in percent injected dose per gram (%ID/g).

4.10 Radiolabeling of CuS-Mn NPs with ^{67}Cu

In order to further demonstrate the intrinsic radiolabeling approach and flexibility, another radionuclide was investigated. ^{67}Cu is near ideal (theranostic) radionuclide. It emits both therapeutic radiation (beta particles) and low energy gamma photons ideal for SPECT imaging. It has a 62 hrs half-life which is long enough to study prolonged kinetics, yet short enough so it does not deliver high radiation dose to patients. In the course of ^{67}Cu radiolabeling, the radionuclide was also used to intrinsically radiolabel a NP based on cerium oxide nanoparticle (CONP) which was previously labeled with ^{89}Zr.[13]

4.10.1 Synthesis of radiolabeled [^{67}Cu]-CuS, [^{67}Cu]-CuS-Mn and [^{67}Cu]-CONP NPs

A. Synthesis of [^{67}Cu]-CuS nanoparticle:

The synthesis of ([^{67}Cu]-CuS NPs) was done by the reaction of $CuCl_2$ (13.4mg, 0.1 mmole), and $Na_2S.H_2O$ (0.1 mmole) in aqueous solution in the presence of organic polymers (PAA) (25mg). The reaction involves Na_2S with $CuCl_2$ in organic polymer solution at room temperature for 5 min, to form CuS core, followed by heating of the reaction mixture to 90° C for 30 min, to enable NPs

growth. For radiolabeling with ^{67}Cu, a 100 µl of $^{67}CuCl_2$ (≈150 µCi) was added to cold $CuCl_2$ solution before starting the reaction to incorporate ^{67}Cu in core NPs. The obtained NPs were purified using a 3KDa MWCO filters by spinning the solution at 4750 rpm for 30 min at room temperature to remove non-NP associated radioactivity.

B. Synthesis of [^{67}Cu]-CuS-Mn nanoparticle:

The synthesis of manganese doped copper sulfide nanoparticles (CuS-Mn NPs) was done by the reaction of $CuCl_2$ (13.4mg, 0.1 mmole), $MnCl_2.H_2O$ (3.4mg, 0.02 mmole) and $Na_2S.H_2O$ (0.12 mmole) in aqueous solution in the presence of PAA (25mg). The reaction involving Na_2S with $CuCl_2/MnCl_2$ in presence of PAA solution at room temperature for 5 min, to form CuS-Mn NPs core, followed by, heating the reaction mixture to 90° C for 30 min, to enable NP growth. For radiolabeling with ^{67}Cu, a 100 µl of $^{67}CuCl_2$ (≈150 µCi) was added to $CuCl_2/MnCl_2$ solution before starting reaction to incorporate ^{67}Cu in core NPs. The obtained NPs were purified by using a 3KDa MWCO centrifuge filters by spinning the solution at 4750 rpm for 30 min at RT to remove non-NP associated radioactivity. Synthesis scheme for ^{67}Cu labeled CuS-Mn NPs is shown in figure 17.

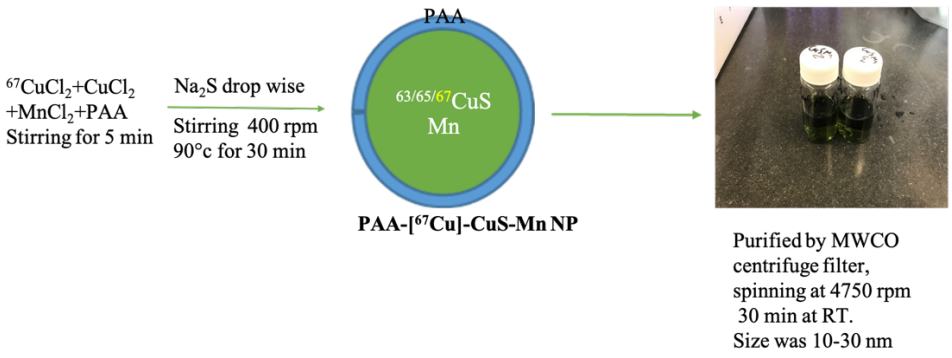

Figure 17: Synthesis scheme for ^{67}Cu labeled CuS-Mn NPs. $^{67}CuCl_2$ was added to the synthesis to incorporate ^{67}Cu into the CuS-Mn NP. PAA coated material was used to synthesis CuS-Mn NP. 3k MWCO filters were used for purification. HD size range was 10-35 nm.

C. Synthesis of [^{67}Cu]-CONPs

Another metal-based nanoparticle which is developed by our group is CONP and has been intrinsically radiolabeled with other radionuclides such as ^{89}Zr and ^{111}In [39]. The synthesis scheme of [^{67}Cu]-CONP is shown in figure 18, and the procedure as follows:

1- To a 10 ml vial, cerium nitrate Ce $(NO_3)_3 \cdot 6H_2O$ (4mg) and polyacrylic acid (PAA) (10mg), and a desired volume of $^{67}CuCl_2$ (100 µl of ≈150 µCi) was added. Water was added to bring the volume to 600 µl.

2- Another separate vial was filled with a diluted ammonium hydroxide NH_4OH (10x dilution of concentrated 28% NH_3 stock).

3- To a 600 µl of diluted NH_4OH, the prepared solution in step one was added. The solution was stirred overnight 400 rpm at RT.

4- The obtained NPs were purified using 0.2µm filter to remove large particles and a 3 KDa MWCO centrifuge filters by spinning the solution at 4750 rpm for 30 min at RT to remove non-NP associated radioactivity.

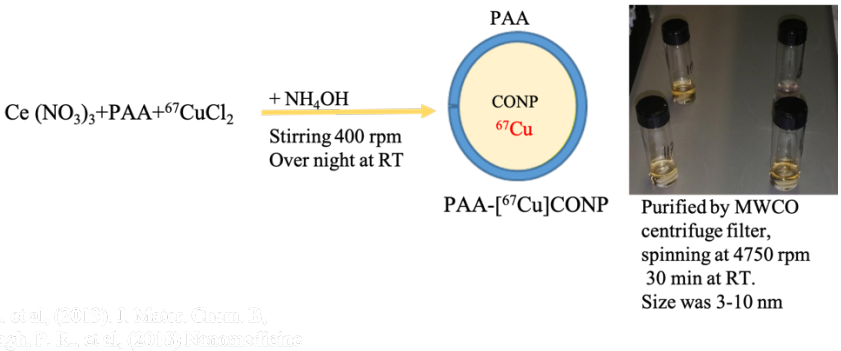

Figure 18: Synthesis scheme for ^{67}Cu labeled CONPs. $^{67}CuCl_2$ was added to the synthesis to incorporate ^{67}Cu into the CONP. PAA coated material was used to synthesis CONP, 3k MWCO filters were used for purification. HD size range was 3-10 nm.

4.10.2 Radiolabeling yield measurement of [^{67}Cu]-CuS, [^{67}Cu]-CuS-Mn and [^{67}Cu]-CONP

The obtained radiolabeled NPs were purified using a 3KDa MWCO centrifuge filters by spinning the solution at 4750 rpm for 30 min at RT to remove non-NP incorporated radioactivity. Radioactive reaction yields of ^{67}Cu incorporated into CuS, CuS Mn and CONPs were measured using an ionization chamber-based dose calibrator (Capintec CRC-15 PET) and gamma counting. Measurements were taken during the radiosynthesis, end of radiosynthesis and one week after the synthesis, to determine the radiochemical yield and retention of the radioactive at various steps.

4.10.3 Cells Uptake of [^{67}Cu]-$CuCl_2$ [^{67}Cu]-CuS, [^{67}Cu]-CuS-Mn and [^{67}Cu]-CONP

As part of evaluation of multimodality [^{67}Cu]-CuS-Mn NP in order to validate the nature and chemical identity of externally detected imaging signals. The assessment of surface coating NPs on cell binding (non-specific binding) uptake was done. To understand interactions of three types of radiolabeled NPs with cells, three cell lines were used to determine cell uptake kinetics. The *in vitro* cell uptake studies were done by using relatively low concentrations of $^{67}CuCl_2$, [^{67}Cu]-CuS NP, [^{67}Cu]-CuS-Mn NP, and [^{67}Cu]-CONP to assess the accumulation in to U87-MG, COLO-205 and MDA-MB-435 cell lines within the time. The procedure was done as follows:

1- Three cell lines were used for cell uptake experiment, human brain glioblastoma astrocytoma (U87-MG), human colon carcinoma (COLO-205) and breast cancer cell lines (MDA-MB-435).
2- Cell Culture: Cell lines were maintained in humidified incubator at 37 °C and 5% CO2. Briefly, cells were grown in DMEM/High glucose medium supplemented with 10% fetal bovine serum (FBS), 5mM L-Glutamine, Penicillin (100U/ml), Streptomycin (100µg/ml)

and Amphotericin B (0.25 ug/ml). The cells were grown to 70-80% confluency before they were used.

3- Then 1X10^{6}cells were incubated with 200 µl [^{67}Cu]-Cl_2, [^{67}Cu]-CuS NPs, [^{67}Cu]-CuS-Mn NPs and [^{67}Cu]-CONP in DEME media at 37 °C and 5% CO2. Three incubation times (1hr, 4 hrs and 24 hrs) were studied in triplicate.
4- At the end of the incubation period the supernatant was collected and used for gamma counting.
5- Cell pellet was washed with phosphate buffer saline (PBS) by spun down at 1000 rpm for 10 minutes 3 times, and wash was collected for gamma counting.
6- After third wash, cell pellet, wash 1,2,3 and supernatant were collected for gamma counting.

4.10.4 *Ex vivo* Biodistribution of [^{67}Cu]-CuS-Mn NP

The biodistribution of [^{67}Cu]-CuS-Mn NP was done in normal female CD-1 mice.

Methodology: A nine mice (3 groups, n=3) were iv injected with a 200 µl of [^{67}Cu]-CuS-Mn NPs (≈ 25 µCi). Mice were dissected at 15min, 1 hr, and 24 hrs post-injection, blood samples and major organs were collected and weighted. Gamma counter (Perkin Elmer Wallac Wizard 1470) was used to measure radioactivity of each tissue. The percentage of the injected dose per gram (%ID/g) of tissues was calculated from the total injected dose and organ weights. The organs removed for counting are given below:

1-Blood, 2-Heart, 3- Liver, 4- RT.&LT. Kidney, 5-Spleen, 6-Muscle, 7-Lung, 8-Urine, 9-Feumer bone, 10-Skull, and 11-Brain.

Chapter 5: Results

5.1 Characterization of CuS-Mn NP

5.1.1 Absorption spectra of CuS-Mn NPs

The optical properties of CuS NPs and CuS-Mn NPs were characterized using UV-visible as explained in section 4.5.1. To study the effect of surface coating and content of manganese on the absorption of synthesized CuS NPs and CuS-Mn NPs, the absorption spectra have been analyzed as shown in figure 19 below. All the NP preparations showed a NIR peak in the region of 400-1100 nm. The addition of Mn and/or the surface coating still retains absorption at the NIR region for both the addition of Mn (Fig. 19 A) and modification of surface coating (Fig. 19 B). The magnitude of the absorption, however, has dropped slightly compared to the absorption of neat CuS NP.

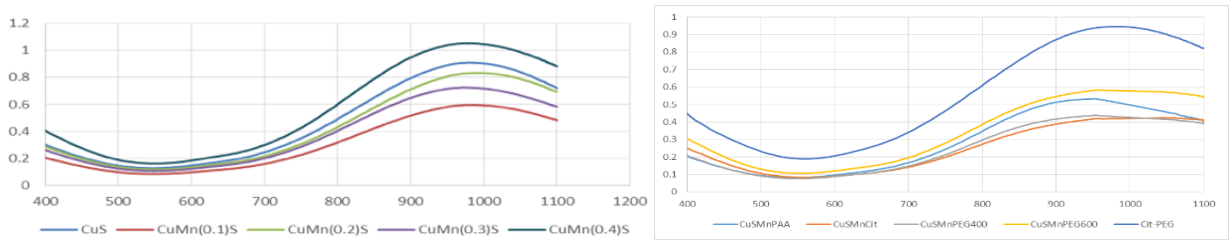

A. B.

Figure 19: A) Absorption of PAA coated CuS NPs with different amount of Mn doping (10%, 20%, 30% and 40%). B) Absorption CuS-Mn with different surface coating (PAA, Citric acid, Polyethylene glycol (PEG) and Cit-PEG).

5.1.2 Hydrodynamic size (HD) and zeta potential (ZP) analysis of CuS NP and CuS-Mn NP

The use of different precursor coating materials resulted in different sizes and charges of the synthesized NP. The synthesis of Mn doped CuS NPs was successfully achieved and variation in the amount of Mn content has also affected the HD size of the NP. The doped Mn NP reaction yield ranged from 80% to 90% as measured by ICP. The HD size and ZP of CuS and CuS-Mn NPs with various amount of Mn and different coating materials are summarized in table 7. Compared to PEG and citrate, coating with PAA resulted in the smallest HD size.

The amount of Mn doping has also impacted the HD size with 20% Mn content resulting in the smallest size as shown in table 7 and figure 22. The zeta potential of the CuS NPs and CuS-Mn NPs were ranged from (-22mV to -35mV), yielding a negative surface charge of the coated nanoparticles.

Table 7: Hydrodynamic (HD) size and zeta potential of the synthesized CuS NPs, Cus-Mn NP

NPs Type	**Range of size distribution**	**Zeta potential (ZP) (mV)**
PAA-CuS NP	10-40 nm	-29
PAA-CuS-Mn (10%) NP	6-20 nm	-35
PAA-CuS-Mn (20%) NP	2.5-7 nm	-32
Cit-CuS-Mn NP	5-20 nm	-33
PEG-Cit-CuS-Mn NP	10-30 nm	-22

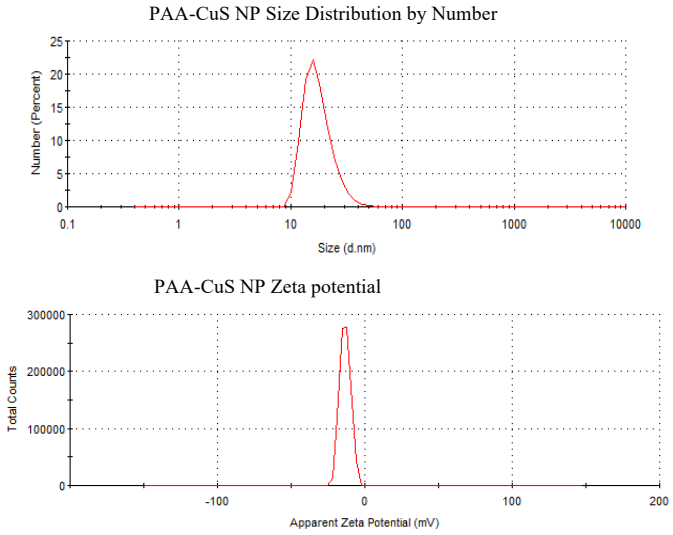

Figure 20: Hydrodynamic size distribution by number (top), and zeta potential (bottom) of PAA-CuS NPs

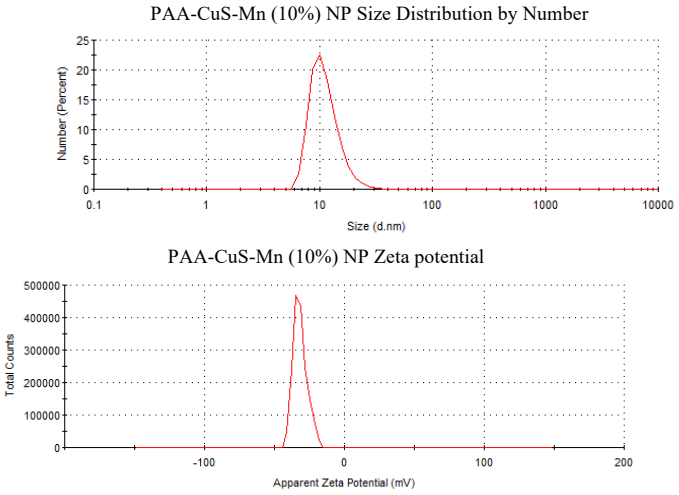

Figure 21: Hydrodynamic size distribution by number (top), and zeta potential (bottom) of PAA-CuS-Mn (10%) NPs

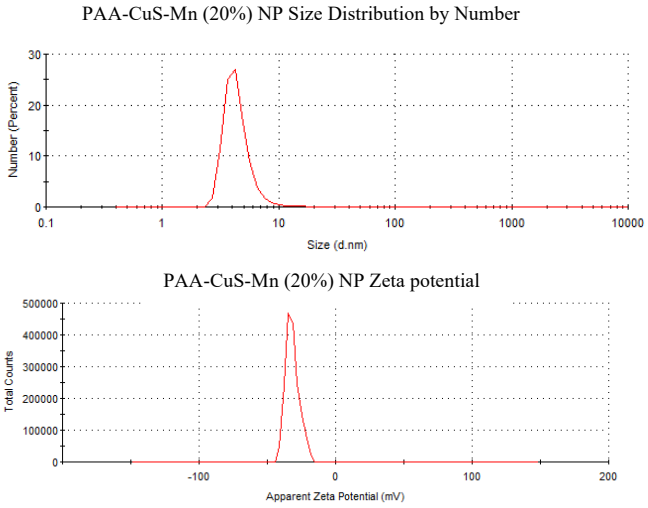

Figure 22: Hydrodynamic size distribution by number (top), and zeta potential (bottom) of PAA-CuS-Mn (20%) NPs

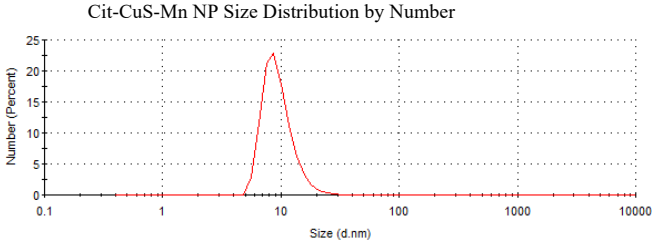

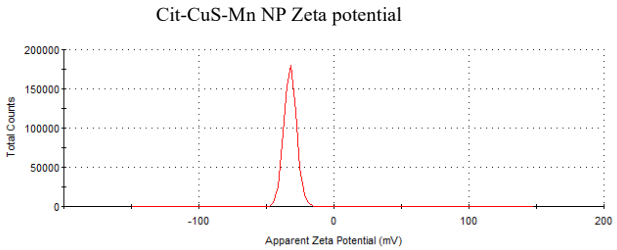

Figure 23: Hydrodynamic size distribution by number (top), and zeta potential (bottom) of Cit-CuS-Mn NPs

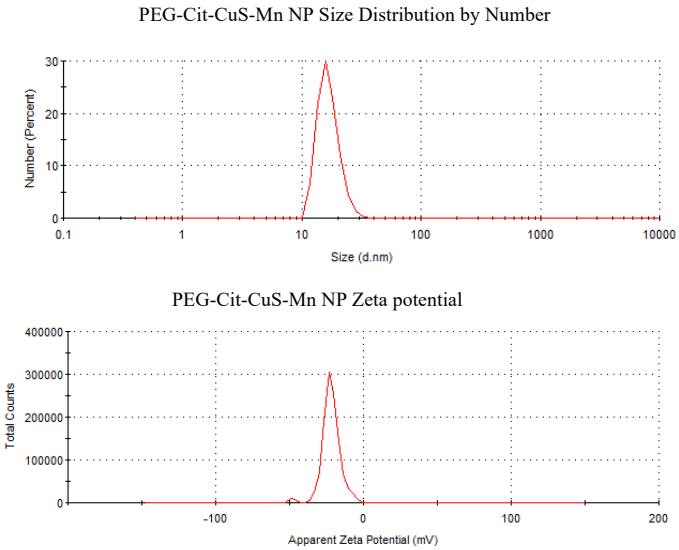

Figure 24: Hydrodynamic size distribution by number (top), and zeta potential (bottom) of PEG-Cit-CuS-Mn NPs

5.1.3 Transmission electron microscope (TEM) for CuS-Mn NPs

The synthesized CuS-Mn NPs was accomplished with the synthesis method as described in section 4.4.1. The morphology and qualitative size were characterized by TEM as described in section 4.2.3. Representative TEM images from different field views of CuS-Mn NPs coated with PAA are shown in (Fig. 25, A). The Samples were prepared by spreading a diluted solution of CuS-Mn NPs onto carbon-coated copper grid. The size measured of each particle is characteristic of the size of the CuS-Mn NPs. The size range was (≈ 5-20 nm). Figure 25, B is showing the HD size of the same sample measured by DLS and the size range was (≈ 7-20 nm).

A) TEM of CuS-Mn NP

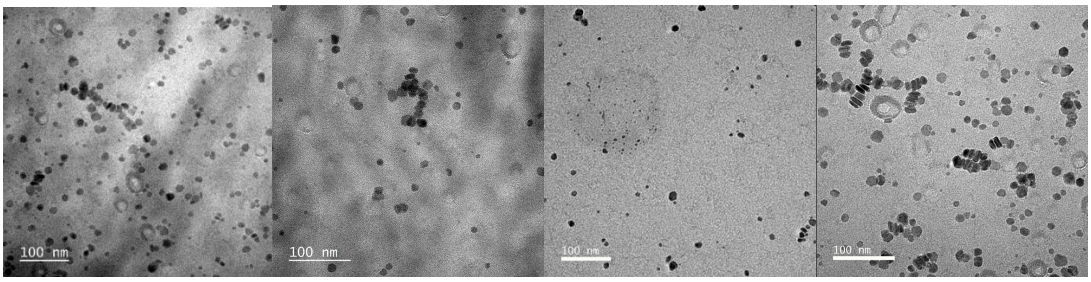

B) PAA- CuS-Mn NP size distribution by number

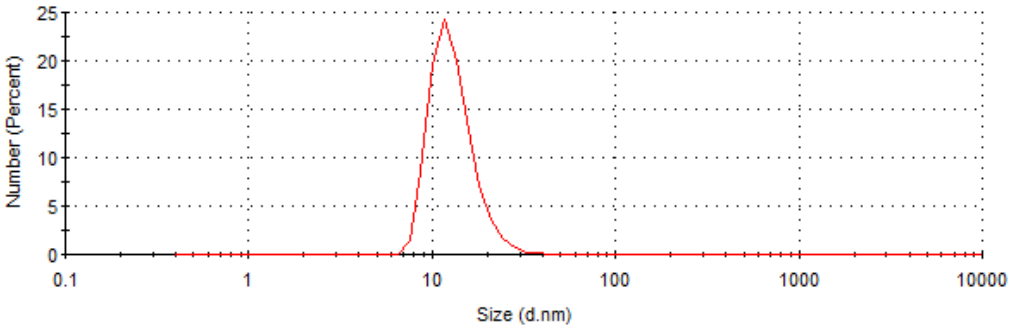

Figure 25: A) Representative TEM images from different field views of CuS-Mn NPs coated with PAA. Samples were prepared by spreading a dilute solution of CuS-Mn NPs onto carbon-coated copper grid. The size measured of each particle is characteristic of the size of the CuS-Mn NP. B) Size distribution by number of CuS-Mn NP measured by DLS.

5.2 MRI relaxivity study of CuS-Mn NP

The MRI signal intensity of the CuS-Mn NP was assessed as a function of Mn concentration and compared to the intensity obtained from "bulk" $MnCL_2$. This was tested in a phantom study, as outlined in section 4.7.1, to obtain a relaxivity curve as shown in figures 26 and 27. Images of the phantom shown in these figures 26, 27 (A and B) indicate image enhancement with increasing Mn concentration for both compounds. Further relaxivity characterization revealed that CuS-Mn NP had a 2-fold increase compared to $MnCl_2$. It can be deduced from figures 26, C and 27, C that CuS-Mn NP shows a two-fold signal intensity higher than $MnCl_2$ (r1: 6.1 $S^{-1}mM^{-1}$ for CuS-Mn NP vs 2.9 $S^{-1}mM^{-1}$ for $MnCl_2$), and (r2: 151.6 $S^{-1}mM^{-1}$ for CuS-Mn NP vs 82.5 $S^{-1}mM^{-1}$ for $MnCl_2$).

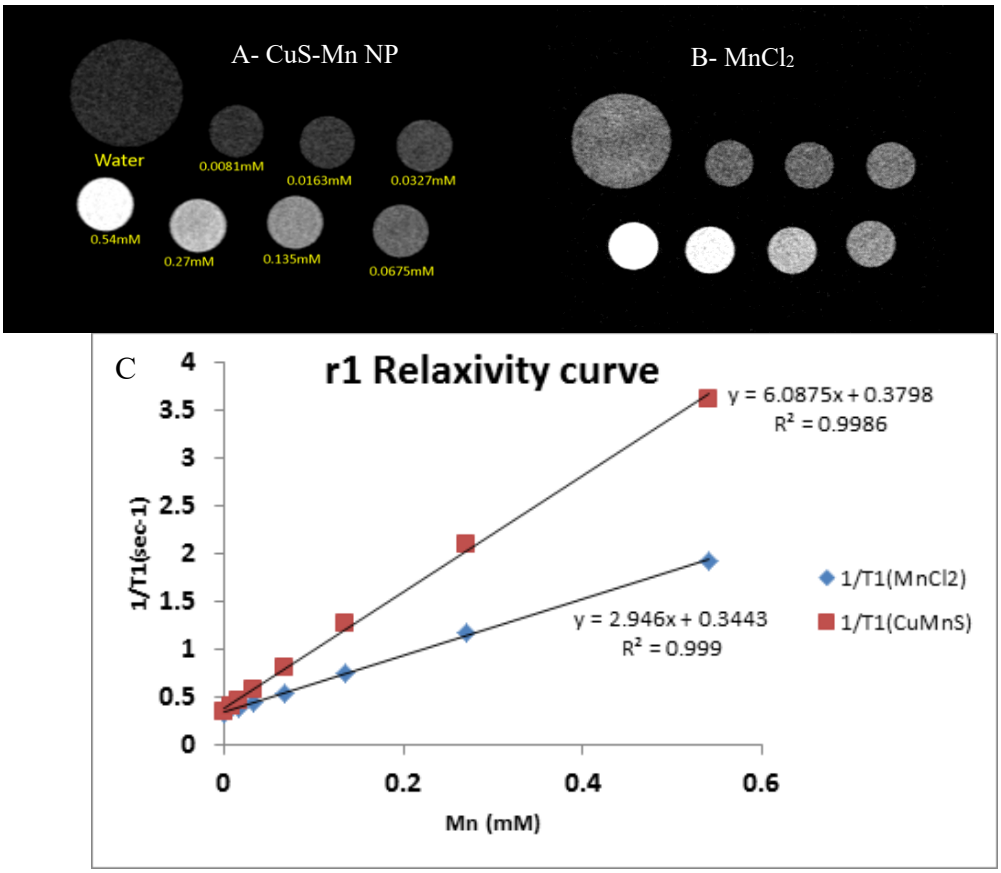

Figure 26: A) CuS-Mn NPs MR T1 images of phantom. B) $MnCl_2$ MR T1 images of phantom. Mn concentration range, 0 mM (Water) 0.0081mM, 0.0163mM, 0.0327mM, 0.0675mM, 0.135mM, 0.27mM and 0.54 mM. C) MRI T1 signal intensity as a function of concentration of CuS-Mn NP and $MnCl_2$ solution in water at various concentration of Mn.

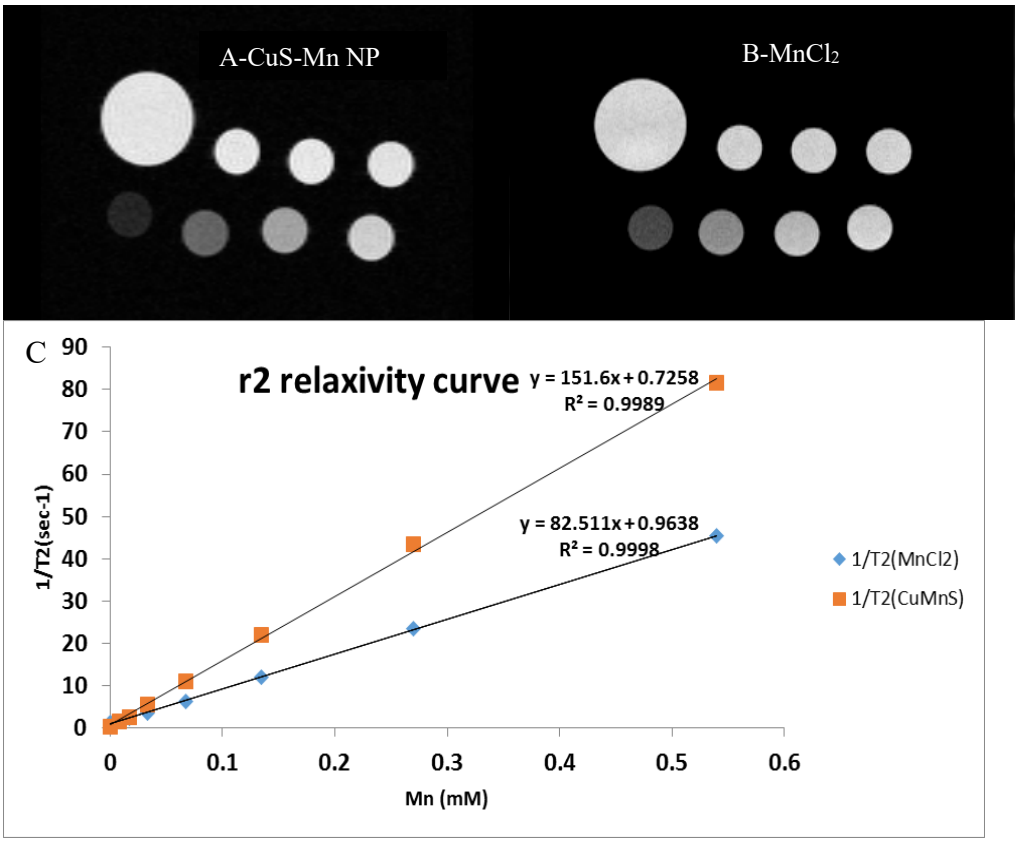

Figure 27: A) CuS-Mn NPs MR T2 images of phantom. B) $MnCl_2$ MR T2images of phantom. Mn concentration range, 0 mM (Water) 0.0081mM, 0.0163mM, 0.0327mM, 0.0675mM, 0.135mM, 0.27mM and 0.54 mM. C) MRI T2 signal intensity as a functional of concentration of CuS-Mn NP and $MnCl_2$ solution in water at various concentration of Mn.

5.2.1 *In vivo* MRI with CuS-Mn NP

To validate *in vitro* MRI characterization of CuS-Mn NP, *in vivo* imaging was accomplished as described in section 4.7.2. Figure 28 is a representative of *in vivo* T1 MR images of a mouse before and 2 hours after the injection of CuS-Mn NPs. Enhancement in both the liver (upper images) and the kidney (lower images) can be seen 2 hours after injection of CuS-Mn NP.

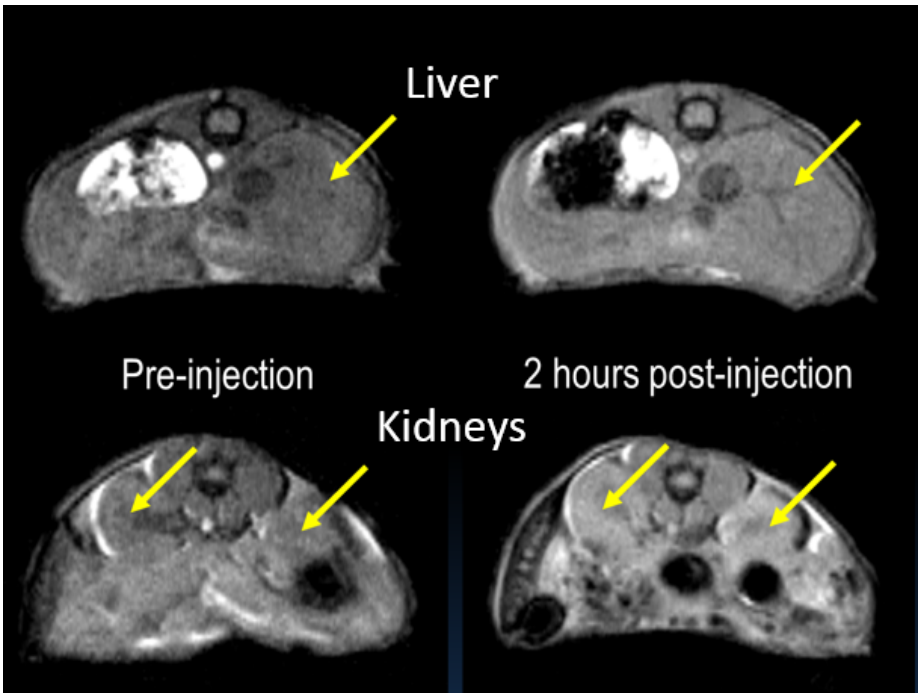

Figure 28: *In vivo* T1 weighted MRI images of mouse pre-injection and 2 hours post-injection of CuS-Mn NPs. Yellow arrows point to liver (top images) and kidneys (bottom images). Images show brighter MRI signal in both liver and kidney following injection.

5.3 MSOT signal as a function of CuS-Mn NP concentration

The CuS NP has a unique property, which is the ability to absorb NIR, which results in an efficient NIR and photoacoustic signal. After doping with Mn, the CuS-Mn NP was evaluated in terms of its photoacoustic performance *in vitro* and *in vivo*. To test the merit of the NP performance as a PA agent using MSOT, both phantom and animal studies were conducted.

MSOT signals as a function of CuS-Mn NP concentrations have been studied and as shown in (Fig., 29), the PA signal increased as a function of the concentration of CuS-Mn NPs, which indicates contrast enhancement due to the CuS-Mn NP. Such enhancement is due to the efficient photo-absorption at the NIR region, resulting in a high PA signal.

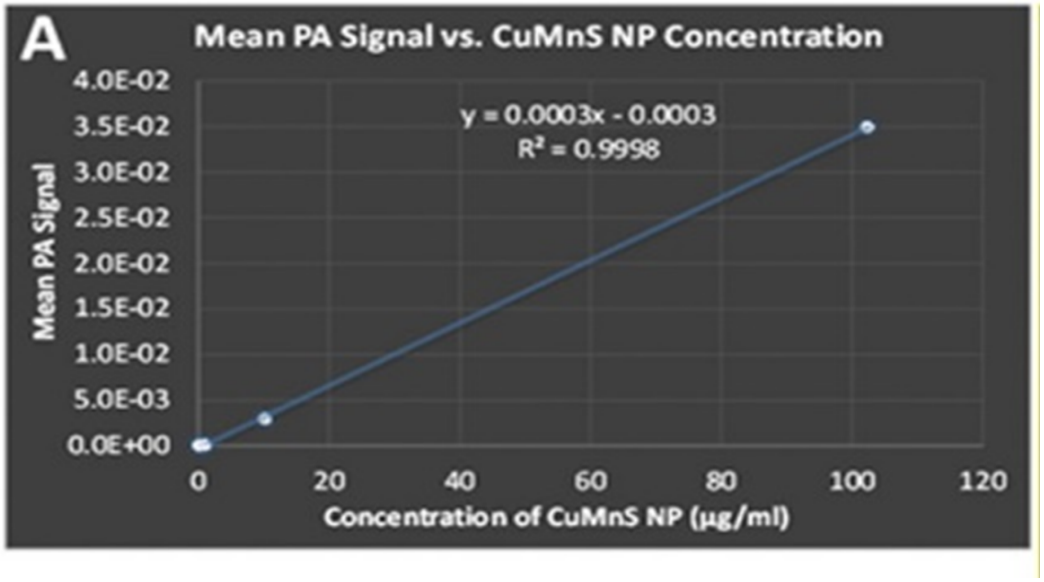

Figure 29: Linearity of MSOT signal as a function of CuS-Mn NP concentration. Photoacoustic signal intensity of CuS-Mn NPs.

5.3.1 CuS-Mn NP Photoacoustic Imaging *in vivo*

In addition to evaluation in a phantom, the CuS-Mn NPs were also investigated *in vivo.* Figure 30 illustrates lack or decreased signal prior to injection, however, increased signal is observed following injection as soon as one hour after injection and persisted for 24 hours. Whole-body imaging showed maximum signal in the abdomen at 1 hr post injection (Fig.31), in fact maximum signal could have been obtained less than an hour post injection as can be seen in the figure. The rapid renal clearance of CuS-Mn NPs allows for the minimum waiting period between injection and start of imaging. The small HD size makes the NP escape engulfing by phagocytosis cells in blood, liver and spleen. This unique feature makes CuS-Mn NP a desirable contrast agent with accelerated renal clearance.

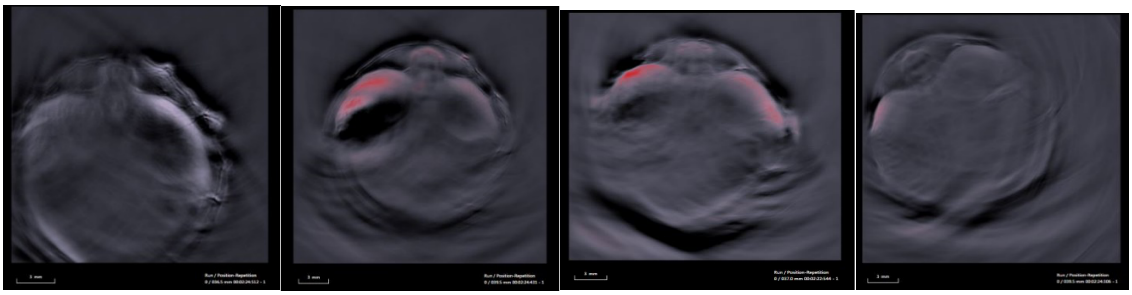

Pre-injection 1hour post-injection 5 hrs post-injection 24 hrs post-injection

Figure 30: Photoacoustic imaging of mice at pre-injection, 1, 5 and 24 hours post i.v. injection of CuS-Mn NPs. MSOT images show PA signal in liver and kidneys as early as 1hour post injection.

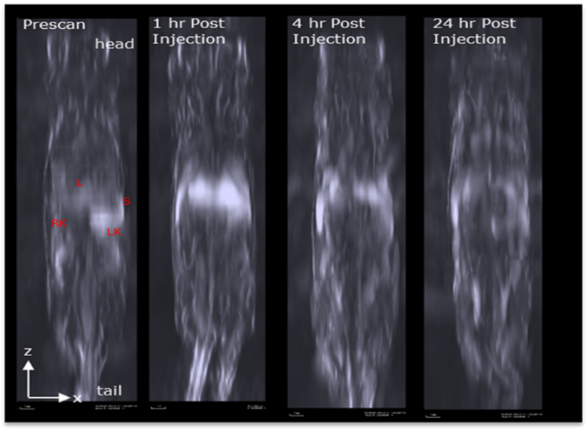

Figure 31: Whole body Photoacoustic Imaging showing contrast signal of CuS-Mn NPS and with time is decreased.

5.3.2 Multi-frame Kinetic Analysis Single Wavelength (800 nm)

Kinetic analysis was calculated for CuS-Mn NPs signal intesity. As shown in figure 32, the presentage of optoacoustic signal in the kidneys and renal clearance were confirmed by photoacoustic imaging. The higher signal percent was in the kidneys (Blue) as soon as the CuS-Mn NPs was injected, followed by the liver (Red). The liver signal was subsequently decreased, followed by the kidneys.

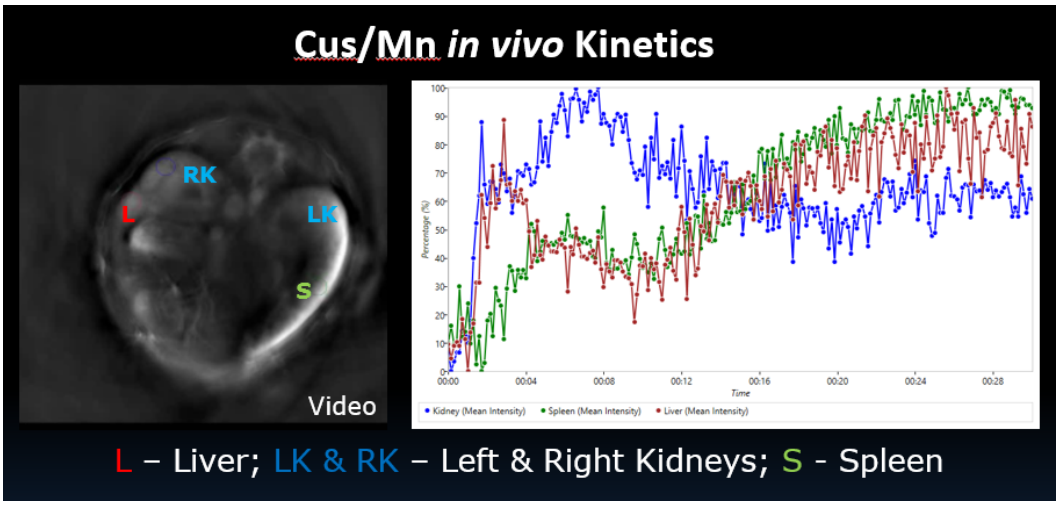

Figure 32: Presence of optoacoustic signal in the kidneys and renal clearance were confirmed by photoacoustic imaging. MSOT kinetic analysis of CuS-Mn NP signal intensity at one wavelenght (800) in mice kidney, spleen and liver post injection

5.3.3 *Ex vivo* biodistribution study of CuS-Mn NP using ICP

To further validate *in vivo* MSOT imaging data a biodistribution study was accumplished as described in section 4.8.3. The bioditribution results were based on *ex vivo* ICP measurments of copper and manganesse in the blood, major organs and tumors. The data was expressed as a relative percentage uptake (organ uptake as a percentage of total Cu/Mn detected in the organ relative to to the total elements in the rest of the organs), excluding the carcass. As seen in figure 33, the liver and the kidneys showed highest accumulation of the NP based on these measurements. This depicts a similar pattern of accumulation as was observed from the MSOT images and kinetic analysis.

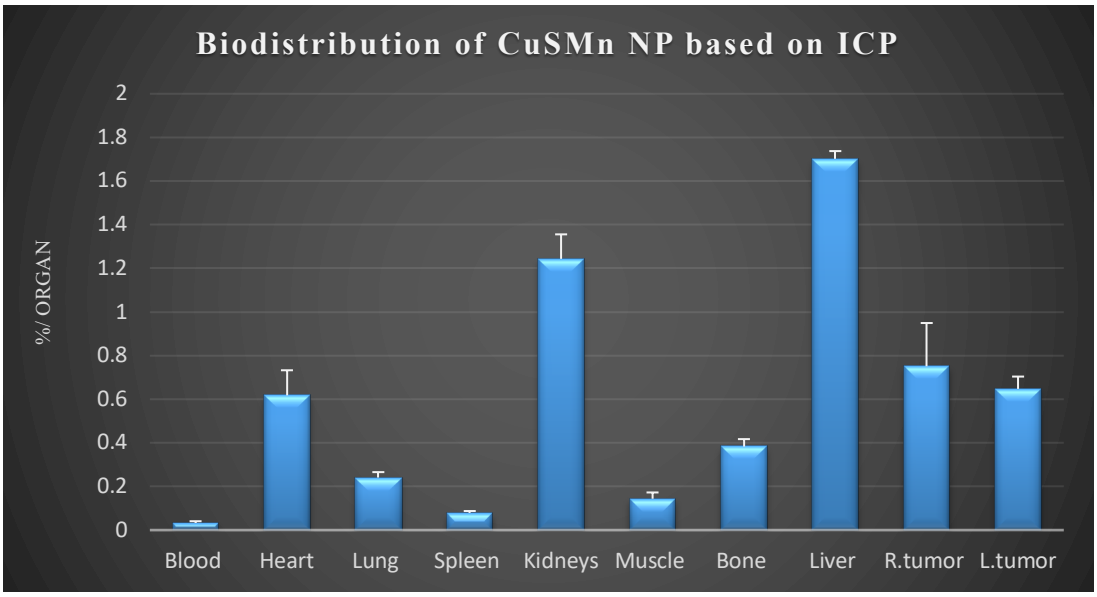

Figure 33: Biodistribution of CuS-Mn NPs in single organs after 24hrs post injection. Tissues were digested by using concentrated nitric acid, and ICP-MS was used to measure Cu and Mn. Results from 1 group of mice (n=3) and presented as average distribution of CuS-Mn NPs per organ, high uptake in liver and kidneys followed by the tumor and heart.

5.4. Radiolabeling of CuS-Mn NP with ^{89}Zr

The ultimate strategy is to use Cu isotopes doped in CuS-Mn NPs because such isotopes are chemically the same as stable copper. However, while developing the concept of doping, ^{89}Zr was the only radioisotope available.

The other purpose of this experiment is to demonstrate the PET capability of CuS-Mn NPs by incorporating a PET isotope.

The synthesis of ^{89}Zr labeled CuS-Mn NP was conducted as explained in section 4.4.2. The radiolabeling reaction yield of [^{89} Zr]-CuS-Mn NPs was > 60%. ^{89}Zr was used due to availability to test the merit of intrinsic radiolabeling. ^{89}Zr may not be the best radionuclide to incorporate into CuS-Mn NPs, due to the element having a different chemistry and oxidation state compared to the di-valent Cu and Mn.

5.4.1 Stability of PAA-[^{89}Zr]-CuS-Mn NP

Size Exclusion Radio-HPLC was used to study the stability of PAA-Coated [^{89}Zr]-CuS-Mn NP to validate the incorporation of ^{89}Zr into the core of the NP and the radioactivity signal represents the radiolabeled NPs. This was done in three different media: water, plasma, and urine. Figure 34 shows the results and radioactive retention time in all samples, A), in aqueous solution the peak had a retention time of 10.3 min; B) after incubation in mouse plasma for 24hrs, the peak had a retention time of 10.7 min.; and C) in urine sample collected 2hrs post injection, the peak had a retention time of 11.3 min. This demonstrates the incorporation and stability of the ^{89}Zr into the CuS-Mn NP.

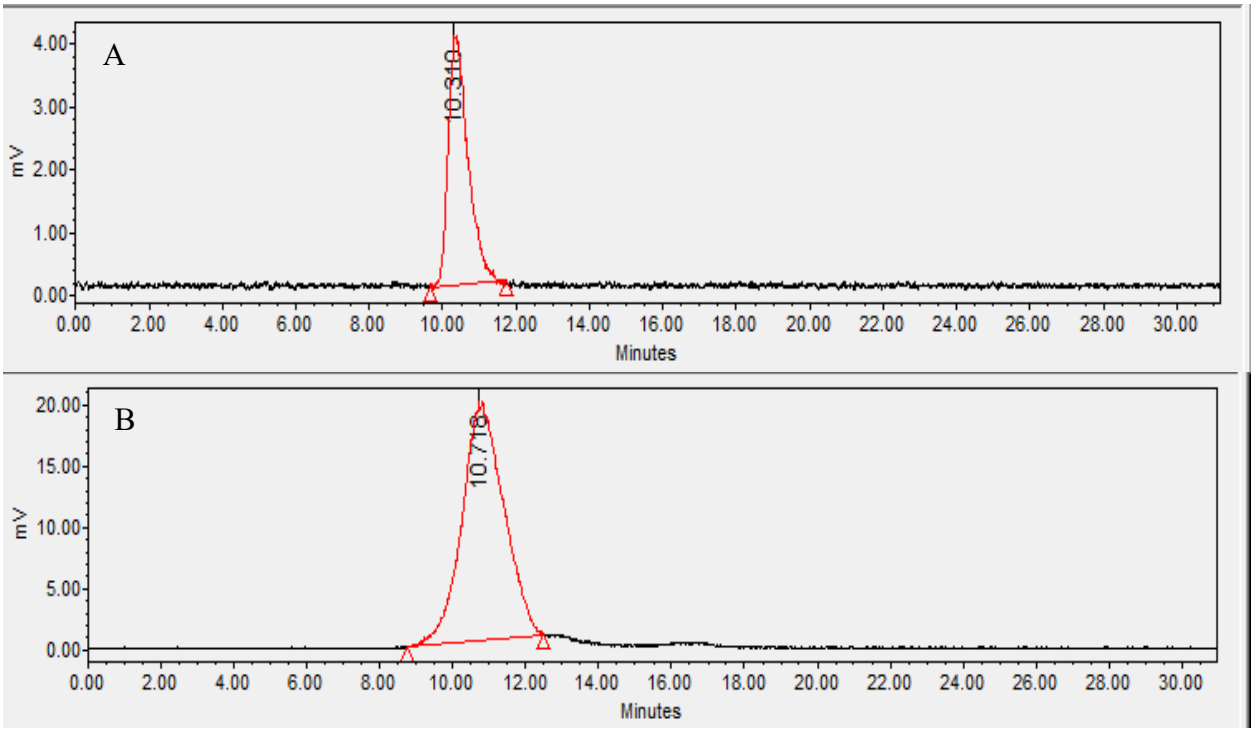

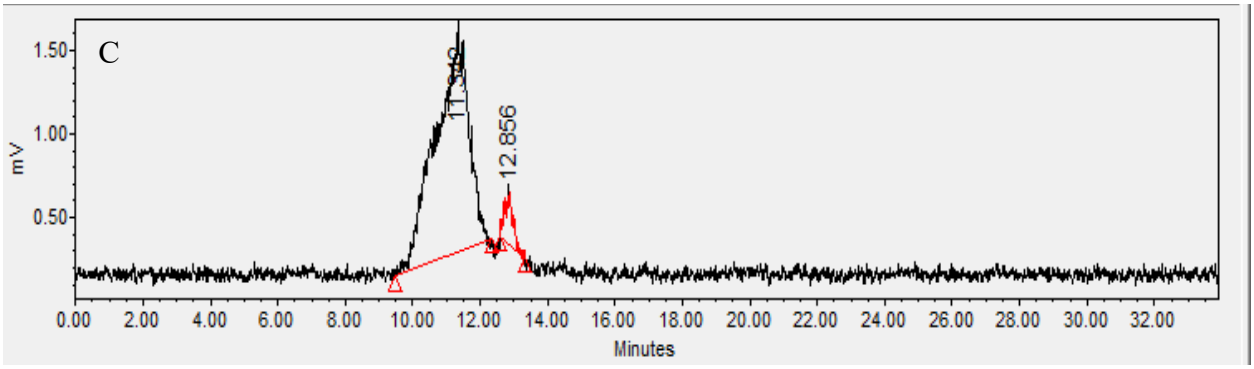

Figure 34: Radio-HPLC retention times of PAA-Coated [^{89}Zr]-CuS-Mn NP. (A) In aqueous solution. (B) After in vitro incubation in mouse plasma for 24 hours. (C) In urine sample collected 2 hours post injection. Samples were injected into HPLC and detected by radioactivity of ^{89}Zr.

5.4.2 *In vivo* PET imaging of [^{89}Zr]-CuS-Mn NP

PET imaging of [^{89}Zr]-CuS-Mn NPs was accomplished as explained in section 4.9. ^{89}Zr PET imaging was performed in mice at 30 min, 2 hrs and 24 hrs post injection of (≈320 µCi) [^{89}Zr]-CuS-Mn NPs (0.04 µmole). There was rapid first pass renal clearance of [^{89}Zr]-CuS-Mn NPs as early as 30 min or indeed earlier, because of the small size of the NPs (Figure 35). The small HD size (1-5 nm) of NPs facilitated rapid renal clearance, and the NP does not accumulate appreciably in liver or spleen. As early as 30 min, it was already in the kidney and possibly earlier. There is ^{89}Zr accumulated in the bone, presumably due to detachment of the ^{89}Zr from its NP and subsequent accumulation in the bone, because Zirconium has a strong affinity for phosphate and hence is a bone seeker.

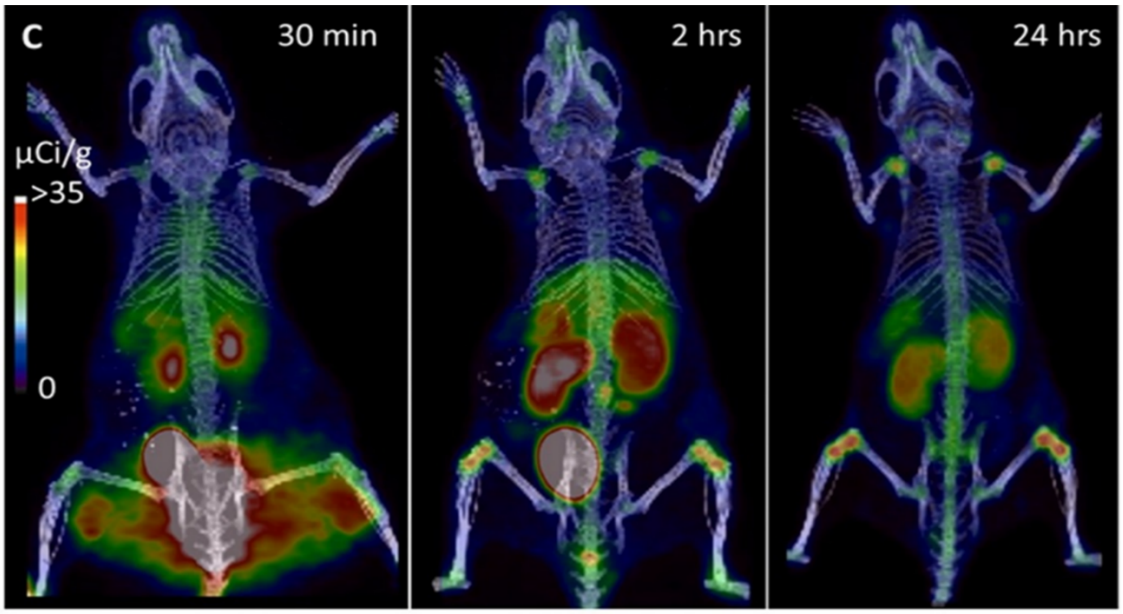

Figure 35: A female nude mice were injected iv with ≈320 µCi of [^{89}Zr]-CuS-Mn NP, and PET imaging was performed in mice at 30 min, 2 hrs and 24 hrs post injection. There was rapid renal clearance of [^{89}Zr]-CuS-Mn NPs as early as 30 min because of the small size of the NPs. The bone uptake because of ^{89}Zr is bone seeker.

5.4.3 Biodistribution of PAA coated [^{89}Zr]-CuS-Mn NPs in nude mice

The *in vivo* image data was validated by quantitative biodistribution results showing rapid uptake and clearance through the kidneys and less uptake in all other organs (Fig.36). The ^{89}Zr activity uptake seen in bone, is probably due to leakage of ^{89}Zr ion from the NP core/shell, and accumulating in bone lattice, as Zr is a bone seeker and has a strong affinity for phosphate. By using another type of radionuclide such as ^{64}Cu/^{67}Cu, bone uptake could be avoided.

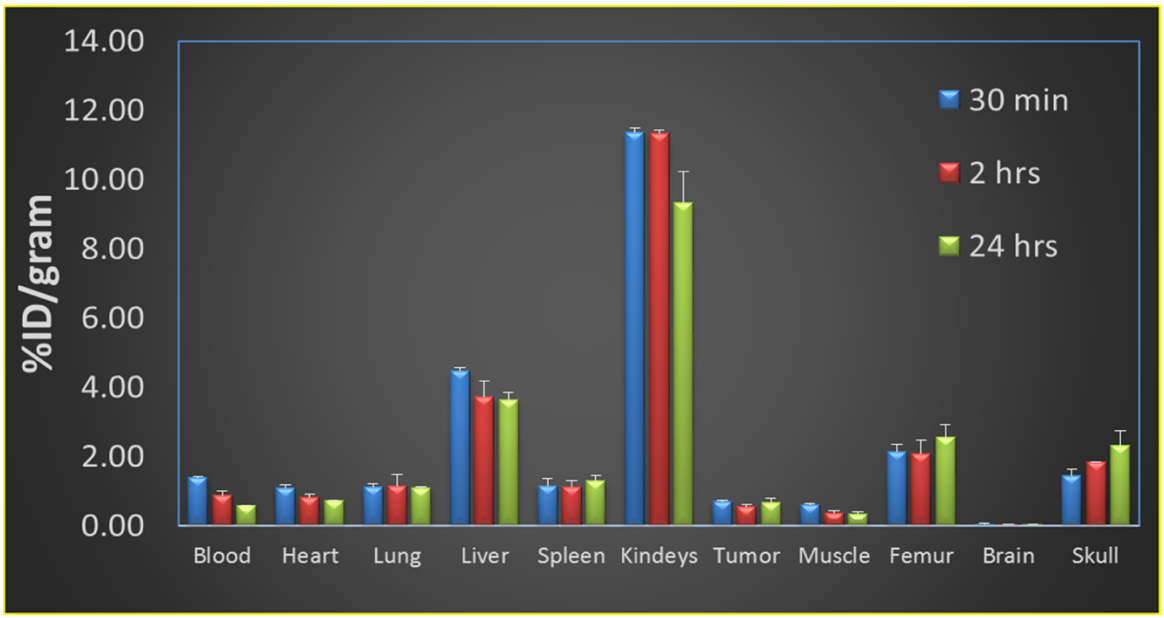

Figure 36: Biodistribution of [^{89}Zr]-CuS-Mn NPs at various time points 30min, 2hrs, and 24hrs. Tissues were weighted, and gamma counted and percent injected dose per gram (%ID/g) was calculated. High uptake in kidney and rapid renal clearance were observed, with low uptake in liver and spleen due to small size of the NPs.

6.1. Radiolabeling of the CuS-Mn NPs with ^{67}Cu

In order to further demonstrate the intrinsic radiolabeling approach and flexibility, another radionuclide was investigated. The ideal radioisotopes to incorporate within the CuS NP are those of copper, ^{64}Cu and ^{67}Cu. ^{67}Cu was incorporated with three types of NPs as explained on section 5.1.2.

6.1.1 Radiolabeling yield measurements of [^{67}Cu]-CuS, [^{67}Cu]-CuS-Mn and [^{67}Cu]-CONP

The Synthesis of intrinsically radiolabeled [^{67}Cu]-CuS, [^{67}Cu]-CuS-Mn and [^{67}Cu]-CONP NPs was accomplished as described in section 5.1.2. The radiochemical yields of [^{67}Cu]-CuS NPs, [^{67}Cu]-CuS-Mn NPs and [^{67}Cu]-CONP were 88±2, 98%±0 and 78%±5 respectively as shown in (Table 8 and Fig.37). The radioactive yield stability of [^{67}Cu]-CuS NP, [^{67}Cu]-CuS-Mn NP and [^{67}Cu]-CONP was measured one week after the synthesis and was the same, excluding loss of radioactivity due to physical decay of the radionuclide. Radiochemical yields for the incorporation

of ^{67}Cu into CuS-Mn NPs and CuS NPs were higher than that of CONP, presumably due to the different chemistry of divalent Cu and Mn compared to that of Zr, indicating that incorporation of the same elemental material results in a higher yield.

Table 8: Radiochemical yield of [^{67}Cu]-CuS NP, [^{67}Cu]-CuS-Mn NP and [^{67}Cu]-CONP after the synthesis. The measurements were taken by dose calibrator and gamma counting (n=3)

Radiochemical yield of [^{67}Cu]-CuS	Radiochemical yield of [^{67}Cu]-CuS-Mn	Radiochemical yield of [^{67}Cu]-CONP
88%±2	98%±0	78%±5

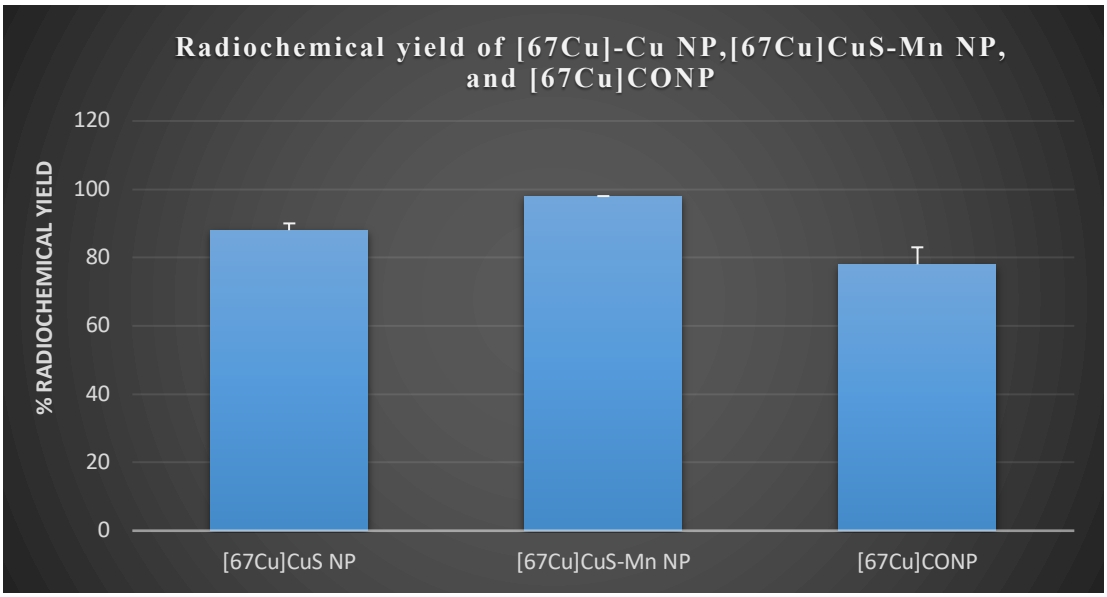

Figure 37: Radiochemical yield of [^{67}Cu]-CuS NP, [^{67}Cu]-CuS-Mn NP and [^{67}Cu]-CONP. The measurements were taken by dose calibrator and gamma counting (n=3)

6.1.2 Cell Uptake of [^{67}Cu]-$CuCl_2$ [^{67}Cu]-CuS, [^{67}Cu]-CuS-Mn and [^{67}Cu]-CONP

Three cell lines were used for the cell uptake experiment, to determine the degree of accumulation by cells, U87-MG, COLO-205 and MDA-MB-435. This was done as preparation of future work to evaluate the radiolabeled CuS-Mn NPs in cancer cells and in tumor-bearing animals. Cell uptake was done for the three types of radiolabeled nanoparticles as well as [^{67}Cu]-Cl_2, a bulk molecule for comparison in order to test the effect of physiochemical properties on cellular uptake.

The cell uptake results are shown in figures 38, 39, 40 and 41. [^{67}Cu]-Cl_2 shows higher uptake in all types of the cell lines and this uptake increased over time in the range of (3% to 22%). [^{67}Cu]-CuS NPs and [^{67}Cu]-CuS-Mn NPs showed lower uptake initially and then increased over time (≈ 0.4 % to 5%). Compared to [^{67}Cu]-CuS NPs and [^{67}Cu]-CuS-Mn NPs, however, [^{67}Cu]-CONPs showed higher cellular uptake which increased over time (1% to 20%).

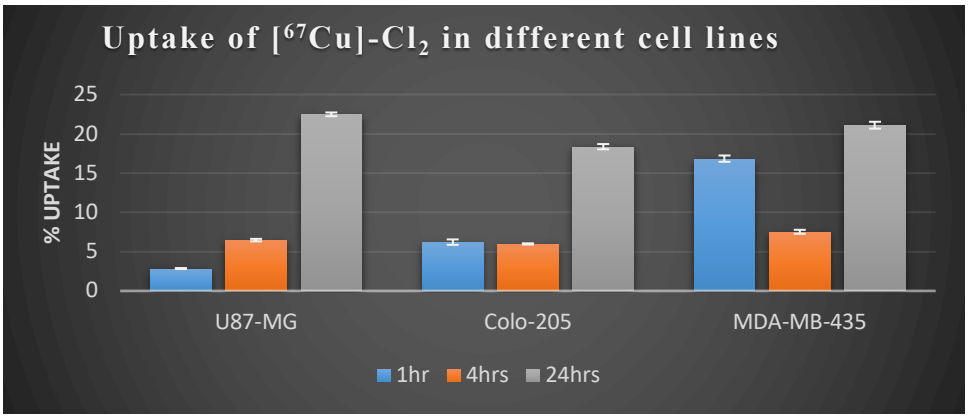

Figure 38: Uptake of [^{67}Cu]-Cl_2 in U87-MG, Colo-205 and MDA-MB435, [^{67}Cu]-Cl_2 shows higher uptake compared with radiolabeled NPs and the cellular uptake increasing over time.

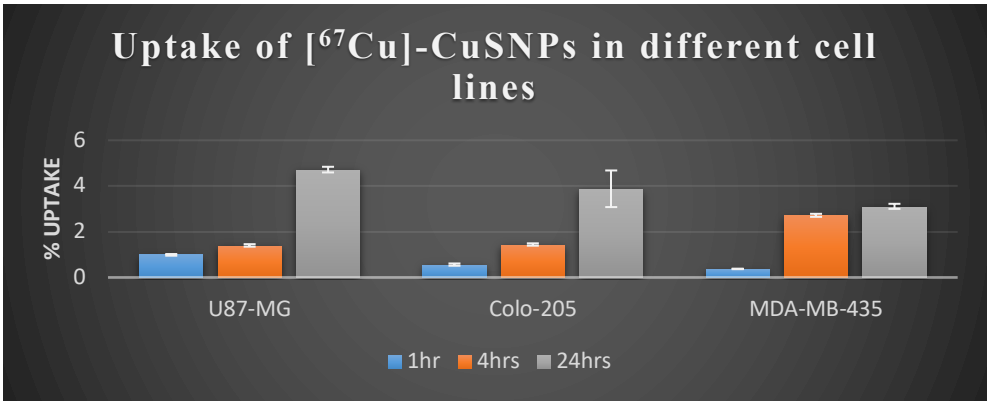

Figure 39: Uptake of [^{67}Cu]-CuS NPs in U87-MG, Colo-205 and MDA-MB435. Uptake of [^{67}Cu]-CuS NPs in U87-MG was 1% at 1 hr incubation and increased over time, with Colo-205 and MDA-MB-435 was ≈ 0.5% and increased at 4hrs and 24hrs.

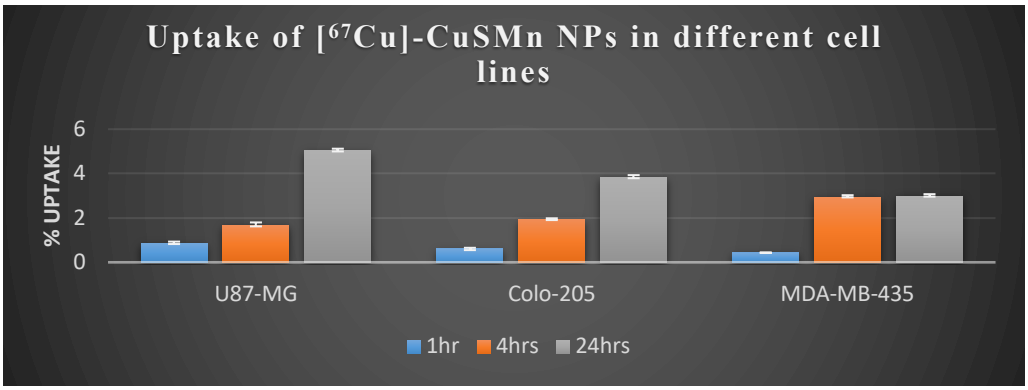

Figure 40: Uptake of [^{67}Cu]-CuS-Mn NPs in U87-MG, Colo-205 and MDA-MB435. Uptake of [^{67}Cu]-CuS-Mn NPs in U87-MG was ≈1% at 1 hr incubation and increased over time, with Colo-205 and MDA-MB-435 was ≈ 0.5% and increased at 4hrs and 24hrs.

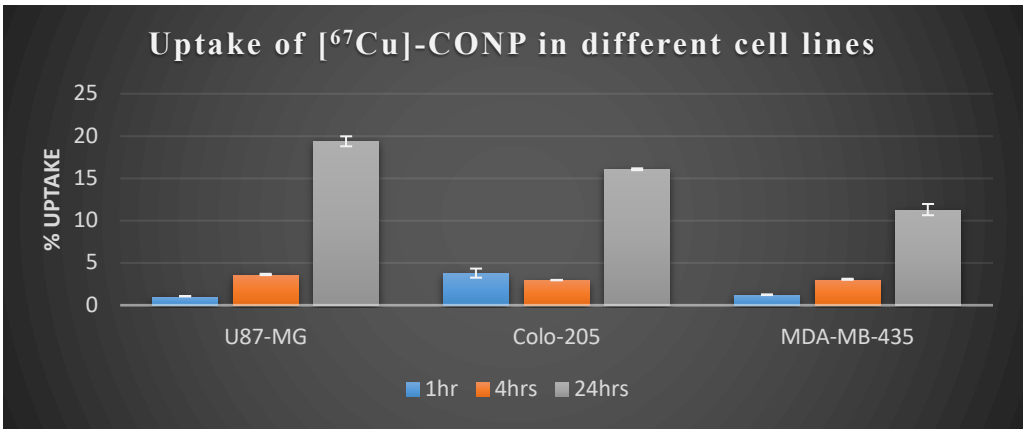

Figure 41: Uptake of [^{67}Cu]-CONP in U87-MG, Colo-205 and MDA-MB-435. Uptake of [^{67}Cu]-CONPs in U87-MG was 1% at 1 hr incubation and increased over time, with Colo-205 was ≈ 4%, at 4hrs was 3% and 24hrs was16%, with MDA-MB-435 was ≈ 1% and increased by the time.

6.1.3 Biodistribution of [^{67}Cu]-CuS-Mn NP

The *ex vivo* biodistribution for [^{67}Cu]-CuS-Mn NPs at 15 min, 1 hr, and 24 hours post injection is shown in (Fig., 42). The results show that the majority of [^{67}Cu]-CuS-Mn NPs is in the liver as a result of NPs being engulfed by liver phagocytosis predominantly due to the larger HD size of these nanoparticles. The increase in liver accumulation over the time period studied indicates hepatobiliary excretion.

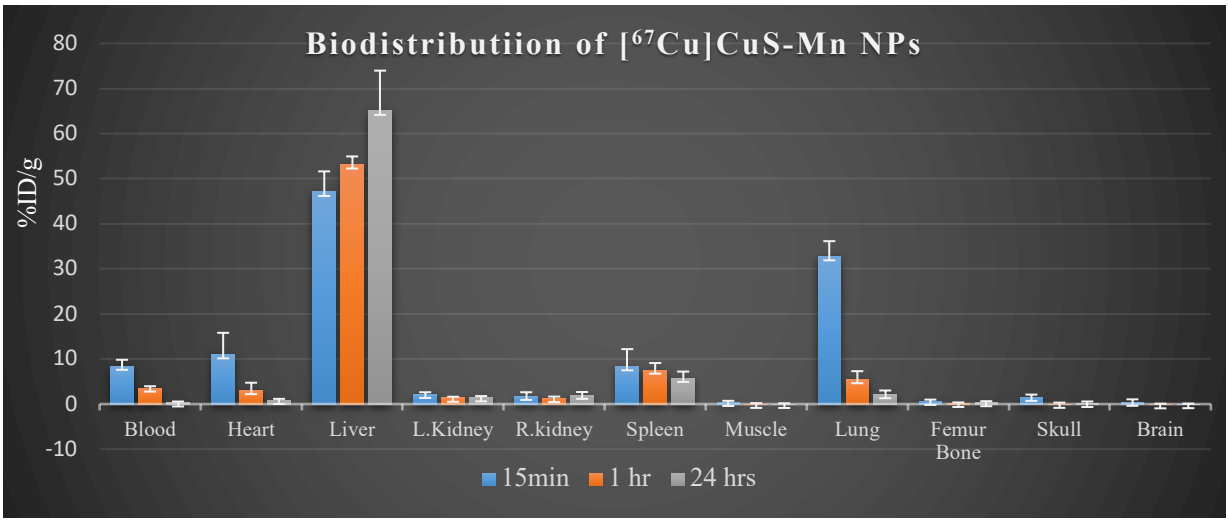

Figure 42: Biodistribution of [^{67}Cu]-CuS-Mn NPs. Uptake of the organ at various time points 15min, 1hr, and 24hrs, (n=3 per time point). Mice tail vein injected with [^{67}Cu]-CuSMn NPs were dissected, and tissues were weighted, and gamma counted and percent injected dose per gram (%ID/g) was calculated. High uptake of [^{67}Cu]-CuS-Mn NPs was by the liver followed by lung, heart and blood.

Chapter 6: Discussion

6.1 Mn doped CuS NPs

Mn was successfully doped within CuS NPs with an 80-90% reaction yield. Mn doping and PAA surface coating has the ability to reduce the size of CuS NPs. Doping 20% of Mn in CuS NPs reduced the HD size up to ≈5 nm which is lower than the renal clearance threshold. The CuS-Mn NP was rapidly cleared by the kidneys because of the small size. Fast clearance is needed and optimum NPs should do their function in the target *in vivo* and then be eliminated from the body.[68] For example, if the NPs are used as a drug delivery vehicle , they has to deliver the drug to the target and then degrade or clear to avoid over exposure of the body to NP and hence reduce overall toxicity.

Absorption spectra and ZP were measured to see the effect of Mn concentrations and different coating materials. Absorption spectra of the CuS-Mn NPs were analyzed with the wavelength range from (400-1100 nm). The data showed a slight shift in absorption, with all recorded peaks in the wavelength range of 900-1000 nm. This is still within the NIR range (700-1100 nm) which maintains PA absorption properties of CuS-Mn NP.[143] HD size and ZP of the different types of the NPs were measured which shows the different size ranges of the CuS-Mn NPs and the difference in range of negative charges depending on the coating materials. The magnitude of charge of the zeta potential value affects the NP interactions with cells and tissues *in vitro* and *in vivo.*

6.2 Intrinsically radiolabeled CuS-Mn NP

Two types of radionuclides were incorporated within the CuS-Mn NPs. ^{89}Zr for PET imaging and ^{67}Cu for SPECT. First, intrinsically radiolabeled CuS-Mn NPs were tested by using ^{89}Zr because of availability. The incorporation synthesis of ^{89}Zr into CuS-Mn NP was successful, with a radiochemical yield of >60% which enabled PET imaging and biodistribution study.

However, ^{89}Zr was not a good candidate due to the difference in chemistry and showed detachment and bone accumulation *in vivo*.

^{67}Cu was used to test the intrinsic labeling within three different types of NPs CuS NP, CuS-Mn NP and CONP. ^{67}Cu is a SPECT radiotracer and useful isotope that can be used for therapy and diagnosis and has medium energy (beta particle, gamma emissions) with a half-life of 2.6 days. The incorporation of ^{67}Cu was successfully accomplished into three different types of the NPs which are CuS NP, CuS-Mn NP and CONP, to test the intrinsically radiolabeling and enable SPECT imaging, cellular uptake and biodistribution study. The radiolabeling yields were 88±2, 98%±0 and 78%±5 respectively. Higher yields resulted in [^{67}Cu]-CuS NP and [^{67}Cu]-CuS-Mn NP due to this same chemistry. Intrinsically radiolabeling using the same chemical material can result higher radiochemical efficiency and good stability.[144] ^{52}Mn and ^{64}Cu can be tested for intrinsically labeled CuS-Mn NP and enable PET imaging.

6.3 PET *in vivo* imaging of [^{89}Zr]-CuS-Mn NPs

To enable PET imaging ^{89}Zr was incorporated with CuS-Mn NP. *In vivo* PET imaging was taken 30 min, 2hrs and 24hrs post injection. [^{89}Zr]-CuS-Mn NPs accumulated in the kidney as early as 30 minutes post injection and decreased over time. This is due to the small size of the NPs which was lower than the renal threshold (HD size ≈ 5 nm) and able to be cleared by the kidneys. This is in sharp contrast to larger NPs which lodge in the liver and spleen due to larger HD size. The nanoparticles can be eliminated from the body by the renal or through hepatobiliary clearance. The small size NPs can be degraded and cleared by the kidneys.[13,145]

^{89}Zr radiolabeling CuS-Mn NPs enable *ex vivo* biodistribution to study organ uptake and retention within the time of the NPs. The [^{89} Zr]-CuS-Mn NPs showed higher uptake by the kidneys after 30 minutes post injection, or possibly sooner, and decreased over time as shown in PET

imaging. The liver showed lower uptake than the kidneys followed by the bones. The higher uptake by the kidneys is because of the small HD size of the NPs which enable them to be cleared through the kidneys as soon they are injected. The bone uptake was due to the fact that ^{89}Zr is a bone seeker which has a high affinity to phosphate. This result validated [^{89}Zr]-CuS-Mn NP PET imaging.

6.4 MRI and MSOT evaluation of CuS-Mn NPs

Mn^{2+} is an inorganic compound and is known as a transition metal ion with five unpaired electrons which can produce a very efficient positive contrast enhancement for MRI such as Gd. Gd-incorporated CuS NPs has been demonstrated feasible imaging for both MR and PA.[146] Mn doped into the CuS NP to enable MR signal. Also, PA signal was assessed as a function of CuS-Mn NP concentration. Relaxivity study was done for CuS-Mn NP in comparison with $MnCl_2$ and the results show enhancement in MRI signal. The linearity relationship between r1 and r2 with the Mn concentration was demonstrated. The CuS-Mn NP showed higher 2 folds than $MnCl_2$. *In vivo* images were taken for mouse liver and kidneys before, and two hours post injection by CuS-Mn NPs. The enhancement in MRI signal was seen in both liver and kidneys post injection. The MRI contrast agent has to be low toxic and with no side effect. Hence, here the small amount of Mn doping within the CuS NP was able to enhance MRI signal, this may overcome with toxicity problems caused by Mn based contrast agents and Gd based contrast agents.[147]

CuS NPs have strong NIR optical absorption properties. CuS-Mn NPs was evaluated in terms of its ability to enhance MSOT signals. Phantom study and *in vivo* imaging were taken pre and post injection (1hr, 5hrs and 24hrs) of CuS-Mn NP. In phantom, MSOT signal intensity was increased as a function of CuS-Mn NP concentration and there was a linear relationship. *In vivo* images of CuS-Mn NPs showed enhancement in MSOT signal and the signal decreased over time because of the clearance of the NPs from the animal.

Ni, Gd, and Fe integrated into CuS NP and successfully applied both PA and MR signal.[146,148,149] CuS-Mn NP demonstrated here as a dual contrast agent for MRI and PA.

6.5 *In vivo* Biodistribution study of CuS-Mn NPs and [^{67}Cu]-CuS-Mn NPs

Radiolabeling CuS-Mn NPs enable *in vivo* biodistribution study to evaluate organs uptake and accumulation over time of the NPs. Gamma counting was used to count the activity. Another biodistribution study was done for unlabeled CuS-Mn NPs and ICP-MS was used to measure Mn and Cu in tissues.

The biodistribution study of [^{67}Cu]-CuS-Mn NPs showed higher uptake in the liver increased over time. The lower uptake showed in the lung, spleen, heart, blood and kidneys which decreased over time. The [^{67}Cu]-CuS-Mn NP was cleared from the body through hepatobiliary excretion. This is due to the size of the [^{67}Cu]-CuS-Mn NP which was (10-30 nm) above the size threshold of renal clearance. In the case of the previous radiolabeling with Zr, the NP size was (≈5nm) which cleared through the kidneys. The nanoparticles can be potentially eliminated via renal or hepatobiliary, both demonstrated here.[11,13]

Another biodistribution study was done by unlabeled CuS-Mn NPs by using ICP-MS. This was done in one time point which is 24hrs post injection in tumor model mice to assess the accumulation of the unlabeled CuS-Mn NP in the tumor and other organs. The higher uptake was shown in the liver followed by kidneys, tumor, heart, bone, lung and muscle. Tumor uptake was based on the advantage of EPR effect of the NPs which adsorbed into the tumor tissue due to vascular leakage. The uptake of CuS-Mn NPs was seen in most major organs which is important as these organs could be targeted for cancer treatment. In future work, the plan is to conjugate the CuS-Mn NPs with a targeting molecule to enhance tumor uptake *in vivo*.

6.6 Cellular uptake of [^{67}Cu]-CuS NP, [^{67}Cu]-CuS-Mn NP and [^{67}Cu]-CONP

For *in vitro* uptake study, the cellular uptake of all types of NPs with three different cell lines (U87, MDA-MB435, and COLO-205) were shown to be gradually enhanced over time. The higher uptake was seen in [^{67}Cu]-CONP compared with [^{67}Cu]-CuS NP and [^{67}Cu]- CuS-Mn NP. This is due to the smaller HD size of [^{67}Cu]-CONP. The HD size affects the cellular uptake as [^{67}Cu]- CONP (3-10nm) size was smaller than [^{67}Cu]-CuS NP (15-30nm) and [^{67}Cu]-CuS-Mn NP (10-30nm). These results showed that the intrinsically radiolabeled NP provides a feasible method to quantitatively study the behavior of CuS-Mn NPs *in vitro*. This work was done to evaluate the passive diffusion of the untargeted radiolabeled NPs into different cancer cell lines. The CuS-Mn NP will be conjugated with targeting molecule (e.g peptide or mAb) to enhance tumor uptake *in vitro* and *in vivo*.

Chapter 7: Conjugation of CuS-Mn NPs to RGD for Integrins targeting

7.1 Introduction

Integrins are cell surface receptor proteins. One of the integrin family members consisting of dimeric alpha v and beta 3 (αvβ) subunits, has been found over expressed in several types of cancer cells, such as breast cancer and glioblastoma. Therefore, the αvβ integrin has become an attractive molecular target for early cancer diagnosis and treatment. Cyclic arginine–glycine–aspartic acid (cRGD) peptide has excellent selectivity and high binding affinity to $\alpha_V\beta 3$ integrin.[150] The cRGD peptide has been well established and labeled with various imaging probes and demonstrated feasibility of imaging integrin receptors in tumors.[5,151]

A method has been developed to conjugate CuS-Mn NPs with cRGD peptide. Characterization by FTIR, DLS and ZP. The flow cytometry was performed on three different cell lines to assess the integrins expression. The RGD-CuS-Mn NP then will be tested in cancer cells with different levels of integrin expression *in vivo*. The NP-conjugate will be evaluated in terms of its binding to integrin receptors expressed to varying degrees in the cancer cell lines, U87-MG, Colo-205, and MDA-MB-345.

7.2 Synthesis of Specific Targeting CuS-Mn NP using cRGD peptide

7.2.1 Synthesis of cRGD-CuS-Mn NPs

In order to facilitate the conjugate cRGD peptide with CuS-Mn NP, the surface coating has to be functionalized by using polyethylene glycol (PEG) or bovine serum albumin (BSA). Two different synthesis strategies were done and the synthesis procedure for each one is described below.

7.2.1.1Synthesis of cRGD-PEG-CuS-Mn NPs

Synthesis of PEG-Cit-CuS-Mn NP

The synthesis of Cit-CuS-Mn NP was done as explained in the section 4.1.1. Briefly, $CuCl_2$ (13.4mg, 0.1 mmole), $MnCl_2.H_2O$ (3.4mg, 0.02 mmole) and $Na_2S.H_2O$ (0.12 mmole) in aqueous solution under existence of sodium citrate (25mg) at room temperature for 5 min, to form CuS-Mn core, followed by heating the reaction mixture to 90° C for 30 min to grow nanoparticles. The obtained Cit-CuS-Mn NPs was purified by using a 3K MWCO by centrifugation. To introduce PEG into Cit-CuS-Mn NPs, the solution was suspended in 1ml H_2O and 1 mg of Thiol-PEG-amine was added to Cit-CuS-Mn NP and incubated stirring at RT overnight to form PEG-Cit-CuS-Mn NP.

Synthesis of cRGD-PEG-CuS-Mn NP

1-The PEG-Cit-CuS-Mn NPs in PBS transferred to a 10 mL vial.

2-Sulfosuccinimidyl-4-(N-maleimidomethyl) cyclohexane-1-carboxylate(Sulfo-SMCC)(5mg/ml) was added to PEG-Cit-CuS-Mn NP under stirring and reacted for 40 min at room temperature. The sulfo-SMCC acts as a bifunctional crosslinker between the PEG-Cit-CuS-Mn NPs and the cRGD peptide.

3-The reaction mixture was purified by Sephadex G25 column to remove unreacted sulfo-SMCC.

4-Cyclo-RGD (1mg/ml) was mixed with activated PEG-Cit-CuS-Mn NP and stirred at room temperature for 1 hour.

5-The cRGD-PEG-CuS-Mn NP was purified and concentrated by centrifuging through a 3,000 MW cut-off centrifuge filter at 4750 rpm for 30 min at RT. Schematic of the reaction is shown below (Fig., 43).

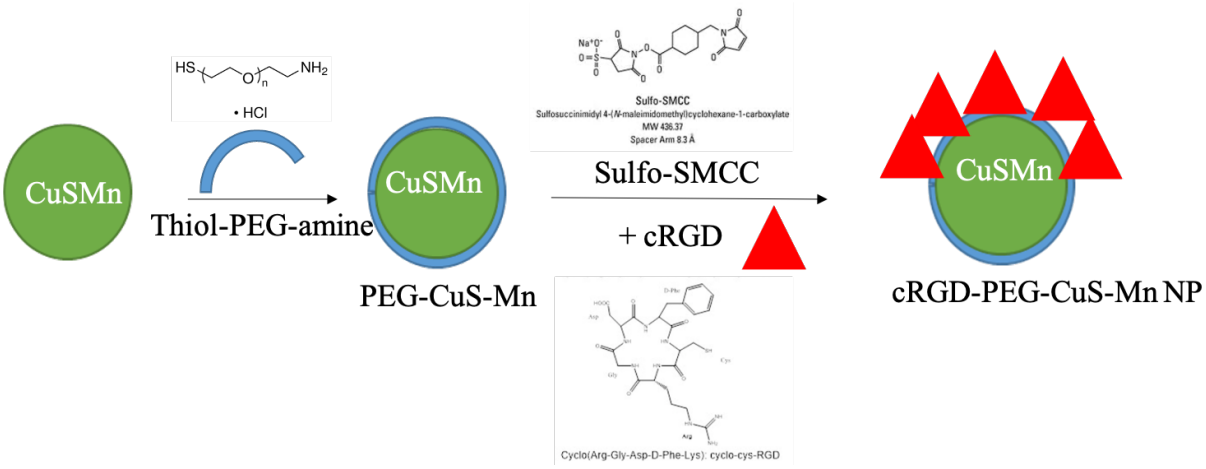

Figure 43: Schematic diagram of synthesis of cRGD-PEG-CuS-Mn NPs. CuS-Mn NPs coated with PEG and then further conjugated with cRGD peptide. Sulfo-SMCC was used as a crosslinker between cRGD and PEG-CuS-Mn NP.

7.2.1.2 Synthesis of cRGD-BSA-CuS-Mn NPs

As an alternative strategy previously used was done by using bovine serum albumin (BSA) as a coating material for the CuS-Mn NPs and then N-(3-dimethylaminopropyl)-N′-ethylcarbodiimide hydrochloride (EDC) and N-hydroxysuccinimide (NHS) used as a crosslinker between BSA and cRGD to form cRGD-BSA-CuS-Mn NPs.[152] EDC is a carboxyl activate agent which then reacted with NHS resulting unstable NHS ester which was reacted with primary amine to form amide crosslinker bond between RGD and BSA. The strategy and schematic of the reaction is shown below (Fig. 44).

1-0.25 g of BSA was dissolved in 7.5 mL of ultrapure water and this was used as the core reagent.

2-Next, 0.268 g of $CuCl_2$, 0.08g $MnCl_2$ and 0.48 g of $Na_2S.9H2O$ was dissolved in 10 mL of ultrapure water to form the reaction solution.

3-Then, 1 mL of the copper solution was added to the BSA solution. 0.5 mL, NaOH solution was added to adjust the pH, followed by the addition of 1.5 mL of sodium sulfide solution.

4-Then, the mixture was heated to 90 °C and stirred for about 30 min, to form BSA-CuS-Mn NP and ready for conjugation with RGD peptide as explained in the following.

5- The aqueous solution then cooled down to room temperature.

6-Then, 40 mg of EDC was added to the prepared BSA-CuS-Mn NP solution at room temperature with slight stirring.

7-After 20 min, 32 mg of NHS was added to the mixture and allow to react for 2 h in the dark. This was followed by adding 1 mL of cRGD (5 mg ml^{-1}) to the solution.

8- The resulting mixture was vigorously stirred for 12 h.

9- The -cRGD-BSA-CuS-Mn NP solution was purified by using (0.22 µm) syringe filters and a 3k MWCO centrifuge filters by centrifugation 3 times at 4750 rpm for 30 min at RT.

10- The purified cRGD-BSA-CuSMn NP solution was then stored at 4 °C for further use.

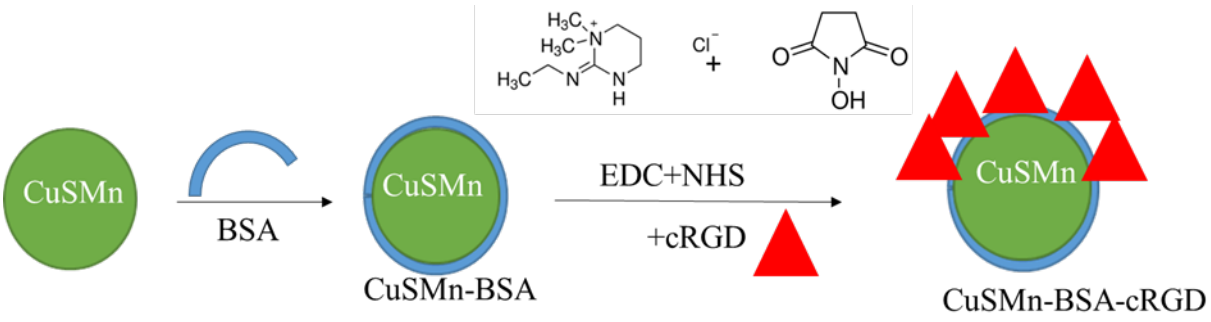

Figure 44: Schematic diagram of synthesis of cRGD-BSA-CuS-Mn NPs. CuS-Mn NPs coated with BSA and then further conjugated with RGD peptide. EDC+NHS was used as a crosslinker between cRGD and BSA-CuS-Mn NP.

7.3 Characterization

The physical characterizations of BSA-CuS-Mn NP and cRGD-BSA-CuS-Mn NP were done by using dynamic light scattering (DLS), zeta potential to evaluate the effect of PEG, BSA and cRGD peptide on the size and charge of the CuS-Mn NP. ICP-OES was done to measure the amount of Cu and Mn in the NP. DLS, zeta potential and ICP-OES were done as explained in a

previous section (4.2). Fourier Transform infrared spectroscopy (FTIR) was done to identify surface functional groups of conjugated cRGD peptide to BSA-CuS-Mn NP and the procedure and principle as below.

7.3.1 Fourier Transform infrared spectroscopy (FTIR)

FTIR spectroscopy is a method used to study solid, liquid, or gas by obtaining a high resolution of wide range of infrared spectrum of absorption. The basic theory is that the bonds between different elements absorb light at different frequencies. The frequency range is from 400 to 4000 cm^{-1} and at a resolution of 0.15 cm^{-1}. In FTIR technique, the instrument produces infrared light passes through interferometer where spectral encoding takes place. When the sample absorbs specific frequencies of energy from the beam that enters the samples compartment, this will characterize the sample. This spectrum provides information about the chemical bounds and molecular structure. The BSA-CuS-Mn NP and RGD-BSA-CuS-Mn NP were dried in the oven at 45°C for 2 hrs. Dry samples as shown in (Fig., 45) were prepared to be tested for FTIR spectrum measurement which was taken at room temperature by using Nicolet iS50 FT-IR.

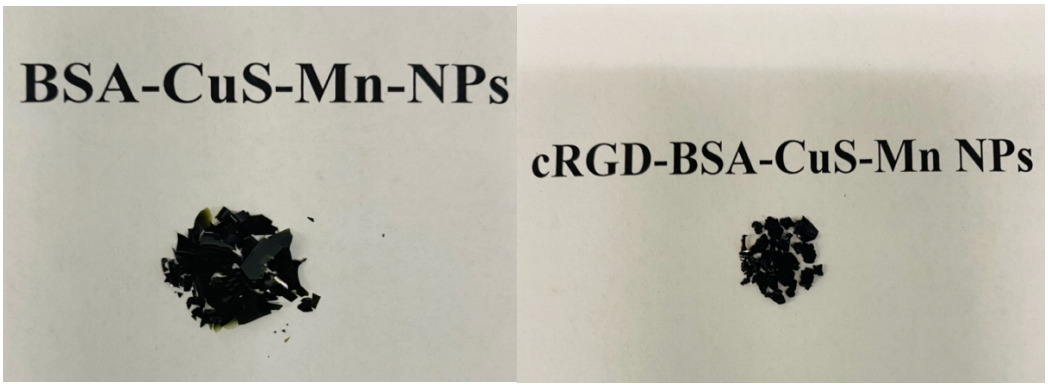

Figure 45: Images of dried synthesized BSA-CuS-Mn and cRGD-BSA-CuS-Mn NPs.

7.4 Flowcytometry analysis of αVβ3 integrins on tumor cells

Integrins receptors expressed on the surface of tumor cells with various levels and lack of expression on other cells. It is important to study the percent of the expression of the integrins before starting implantation in animals. This work was done in the preparation of *in vitro* and *in vivo* work for evaluation of targeting RGD-CuS-Mn NP. The flowcytometry was used to detect the expression level of αVβ3 integrins on the tumor cells. Three cell lines were used; human brain glioblastoma astrocytoma (U87-MG), colon cancer cell line (Colo-205) and breast cancer cell lines (MDA-MB-435), which were measured with a fluorescent labeled antibody.

7.4.1 Flowcytometry

First, the cells were either labeled with fluorochrome-linked antibodies or stained with fluorescent membrane, cytoplasm, or nuclear dyes. Hence, differentiation of cell type (immunophenotyping), the presence of membrane receptors and antigens, membrane potential, pH, enzyme activity, and DNA content can be measured. The basic principle of flowcytometry is that cells which passes through a laser beam can be detected and counted depending on their properties. As the cell passes through the laser beam, light is scattered in all directions, and the light scattered in the forward direction forward scatter (FSC), at low angles (0.5-10°) from the axis is proportional to the square of the radius of a sphere and the size of the cell or particle. Light also may enter the cell and be reflected by nucleus and other contents of the cell; thus, the 90° light (right-angled, side scatter (SSC)) may be considered proportional to the granularity and internal complexity of the cell (Figure 46). Fluorescent labeled internal or external cells components are excited by the laser to emit light at various wavelength. Various detectors are used to measure FSC, a line with the light beam to detect cell volume. The other detector is placed perpendicular to the stream and used to measure SSC which detects the inner component of the cells.[153]

Labeling cells by using fluorescent antibody to detect αVβ3 integrin:

Cells were labeled by using human integrin αVβ3 anti-body and the procedure was as follows:

1- 1 $\times 10^6$ of the cells were collected and washed with phosphate buffer saline (PBS) three times.
2- The cell pellets were resuspended in in 100 µl of staining buffer and were incubated with 5 µL of Fc blocker on refrigerator for 10 min, to prevent non-specific binding of the anti-body.
3- Then, the cells were incubated for 20 minutes with 5 µL of human integrin αVβ3 anti-body labeled with Alexa Fluor 488.
4- The cells were washed three times with staining buffer.
5- The cells were resuspended in 1 ml of staining buffer and analyzed by flow cytometry.
6- Unstained cells were prepared in the same procedure without florescence to be used as a negative control.
7- The fluorescence signal of 50,000 cells were analyzed on a cell-by-cell basis using flow cytometry.

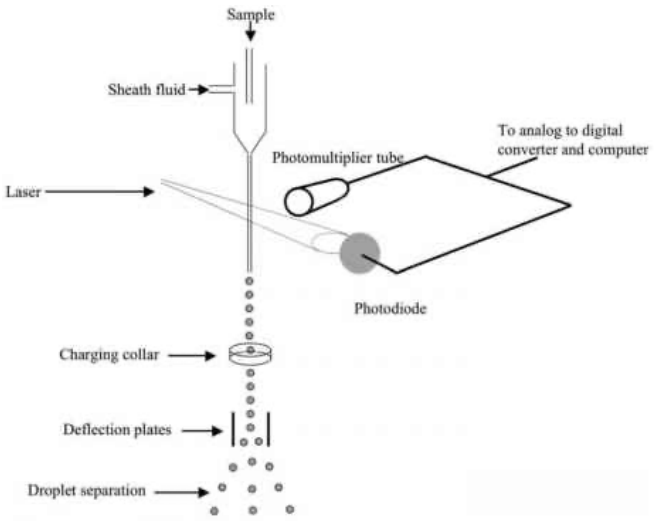

Figure 46: Principle of flowcytometry: Flow cytometry is a technique that colored fluorescence cells particle move in a liquid stream through a laser light. The relative light-scattering by cells particle is measured. Analysis and differentiation of the cells is based on their size, granularity and which cells are carrying antibodies or dyes.

7.4.2 Fluorescence Microscope

After cells were analyzed by flow cytometry, fluorescence microscope (BZ-X800E) was used to image the cells to assess the expression of $\alpha_V\beta_3$ integrins.

7.5 Results and discussion

7.5.1 Synthesis and Characterization of untargeted CuS-Mn NP and targeted CuS-Mn NP

The synthesis of untargeted BSA-CuS-Mn NP and targeted RGD-BSA-CuS-Mn NP was successfully accomplished as described in section 7.2.1. BSA was used as coating material and then RGD conjugated with BSA-CuS-Mn NP using crosslinker as described above. DLS and ZP were done as described in section 4.2. FTIR spectra was done to confirm the conjugation of BSA-CuS-Mn NP with RGD peptide.

DLS and ZP of BSA-CuS-Mn NP and RGD-CuS-Mn NP

The HD size of untargeted BSA-CuS-Mn NP was ranged from 1.5-4 nm and the zeta-potential was -33 mV. The HD size of targeted RGD-CuS-Mn NPs was ranged from 5-20 nm and

zeta-potential was -28 as shown in figure 47. The increased in hydrodynamic size in RGD-BSA-CuS-Mn NP was due to the conjugation of RGD peptide with BSA-CuS-Mn NP.

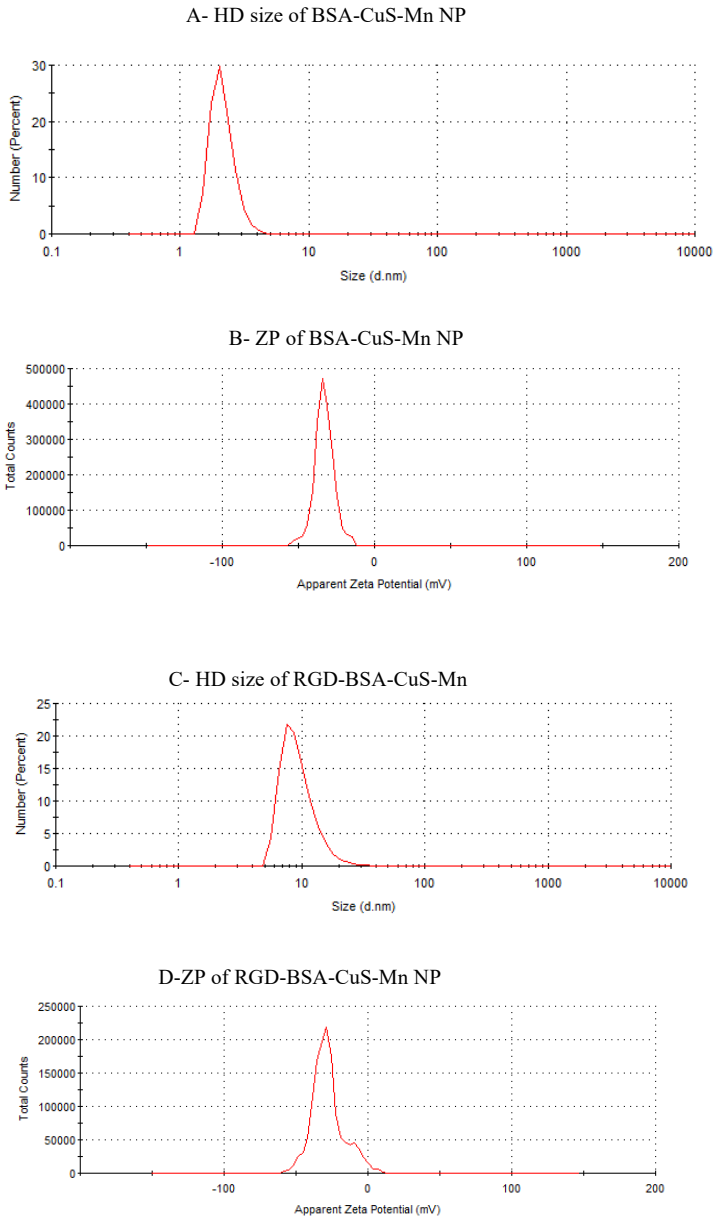

Figure 47: Hydrodynamic size and zeta-potential of A) HD size of BSA-CuS-Mn NPs, B) ZP of BSA-CuS-Mn NPs, C) HD size of RGD-BSA-CS-Mn NPs and D) ZP of RGD-BSA-CuS-Mn NPs, showing different HD size and ZP between both NPs.

The Fourier Transform Infrared Spectroscopy (FTIR)

FTRI spectra of the peptides were measured for RGD-BSA-CuS-Mn NP and the corresponding BSA-CuS-Mn NP (Figure 48). The characteristic IR absorption peaks at 1633 cm^{-1} (amide I, C=O carbonyl stretch vibration) and 1388 cm^{-1} (amide III, C–N stretch vibration) are representative of RGD peptides and were also found in the spectra of the corresponding NP, which indicating the successful binding of peptide molecules to the BSA-CuS-Mn NPs. A stronger and broad peak between 3100 cm^{-1} and 3400 cm^{-1} was observed from the FTIR spectrum of RGD-BSA-CuS-Mn NP, indicating the existence of a –NH–CO– bond between BSA and RGD peptide.

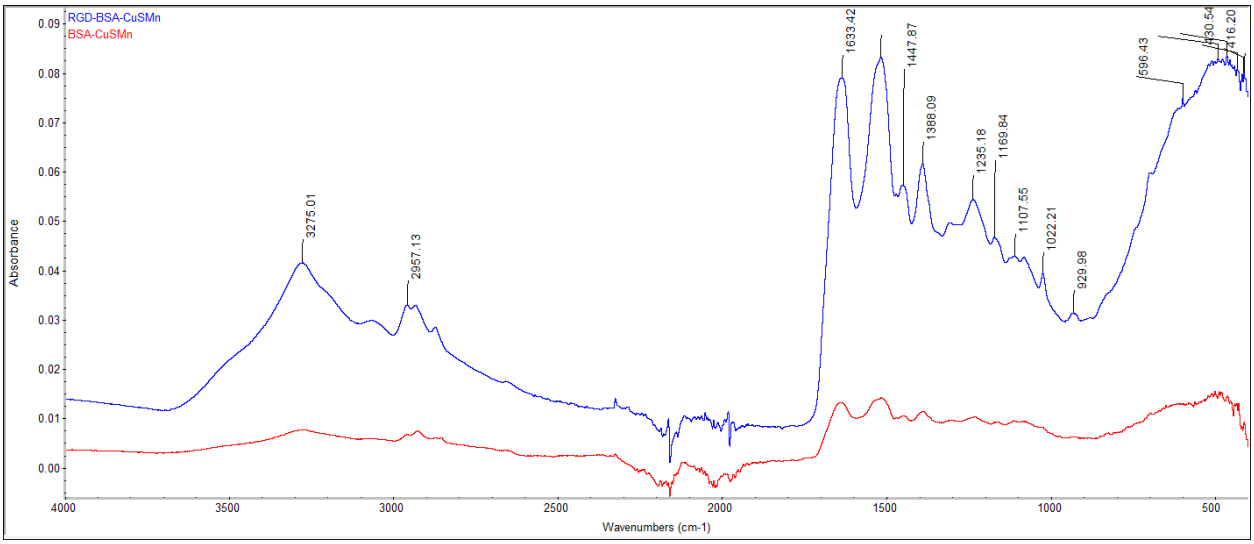

Figure 48: FTIR spectra of BSA-CuS-Mn NPs and RGD-BSA-CuS-Mn NPs

7.5.2 Integrins expression levels

Three different cell lines were used to measure $\alpha_v\beta_3$ integrins expression levels by flow cytometry as explained in section 7.4.2. The antibody-stained cells (labeled cells) were compared with negative unstained cells (unlabeled cells). As can be seen in figure 49, A colo-205 showed a lack in the expression of $\alpha_v\beta_3$ integrins as the cells overlays with negative unstained cells. On the other hand, U87-MG and MDA-MB-435 showed higher expression of $\alpha_v\beta_3$ integrins where the

cells shifted to the positive fluorescence intensity with the αVβ3 antibody-stained cells. Fluorescence microscopic images were taken to validate the flowcytometry result (Figure 50). The U87-MG has been known to express $\alpha_V\beta_3$ integrins and used in previous studies for imaging targeted using RGD peptides. MDA-MB-435 also utilized in previous studies for targeting integrins to enhance therapeutic efficacy. [5,154,155]

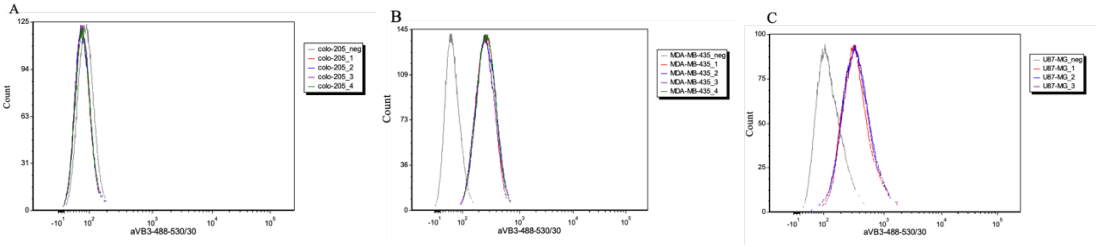

Figure 49: Flow cytometry results of A) Colo-205, B) MDA-MB-435, C) U87-MG cells. U87-MG and MDA-MB-435 cells showed increase fluorescence with the $\alpha_V\beta_3$ antibody stain compared to unstained (negative cells), indicating that the $\alpha_V\beta_3$ integrin is expressed on the U87MG cells and MDA-MB-435. The Colo-205 cells did not show a shift in fluorescence intensity, indicating a lack of αVβ3 integrin expression.

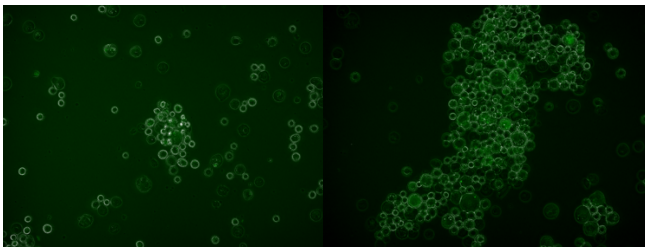

Unlabeled U87. Labeled U87

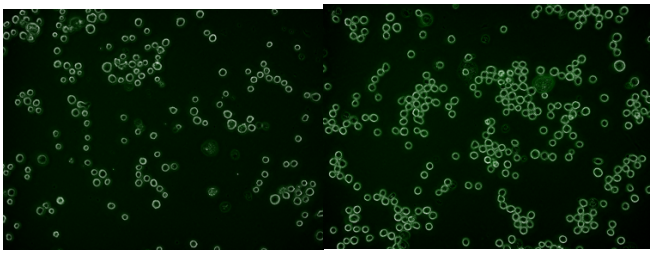

Unlabeled MDA-MB435 Labeled MDA-Mb-435

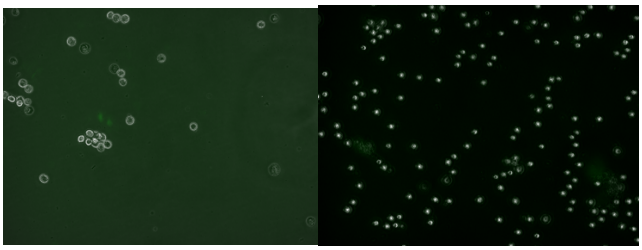

Unlabeled Colo-205. Labeled Colo-205

Figure 50: Fluorescence microscope images of U87, MDA-MB-435 and Colo-205 for stained cells with human integrin αvβ3 anti-body labeled with Alexa Fluor 488 (Labeled cells), compared with unstained cells which not stained with human integrin αVβ3 anti-body labeled with Alexa Fluor 488 (Unlabeled cells).

7.6 Conclusion

This work was undertaken prior to the pandemic and was intended to prepare the groundwork for future *in vivo* studies. Unfortunately, the pandemic had disrupted such plans. The development, however, has been valuable to build upon for future work.

The untargeted BSA-CuS-Mn NPs and targeted RGD-BSA-CuS-Mn NPs were successfully synthesized and ready for *in vitro* and *in vivo* evaluation, which may enhance the tumor uptake. Integrins expression level were studied on three cell lines (U87MG, MDA-MB435 and COLO-205). U87MG and MDA-MB435 were shown over expression of integrins than COLO-205. The cells which showed expression of $\alpha_v\beta_3$ integrins will be candidates for future tumor impanation in mice.

Chapter 8: Summary and Conclusions

8.1 Summary of Conclusion

A general strategy to synthesize a multimodality intrinsic doping/radiolabeling of CuS-Mn NPs was demonstrated. Neither the chemical nor physical properties of radiolabeled CuS-Mn NPs were changed by the incorporation of trace quantities of radionuclides. The NPs have been coated with different coating polymers which facilitate water solubility, stability, biocompatibility, and functionalization. The physiological properties and pharmacokinetics of CuS-Mn NPs can be adjusted by modifying their surface coating. The physiochemical properties were characterized by hydrodynamic size analysis, surface charge, radiochemical yield, absorption spectra, and relaxivity measurements. The cell uptake and biodistribution of [^{67}Cu]-CuS NP, [^{67}Cu]-CuS-Mn NP and [^{67}Cu]-CONP, indicated obvious correlation with its size. Real time *in vivo* PET imaging of [^{89}Zr]-CuS-Mn NPs depicted the fate of the radiolabeled NP and revealed indications of some ^{89}Zr dissociation as evidenced by the bone uptake. This pharmacokinetic picture was reflected in the data obtained by an *ex vivo* biodistribution study. MRI and MSOT imaging were characterized, first in phantom and then in mice and the enhancement of MRI and PA signal were confirmed. Doping with small amount of Mn enabled MR enhancement following intravenous (iv) administration while maintaining PA contrast at the same time. *Ex vivo* biodistribution study of [^{67}Cu]-CuS-Mn NPs were conducted using gamma counting and another biodistribution study of unlabeled CuS-Mn NPs were done using ICP-MS. Both showing higher uptake by the liver which indicating hepatobiliary excretion. Finally, targeting cRGD-CuS-Mn NP was synthesized to evaluate the active targeting *in vivo*. The cRGD peptide was conjugated with CuS-Mn NP through surface functionalization approaches.

The radiolabeling method provides a useful quantitative tool to study and monitor the behavior of the CuS-Mn NPs *in vitro* and *in vivo*. The multimodality radiolabeling CuS-Mn NPs

can be utilized as a novel nanomedicine platform for multiple biomedical imaging and theranostic applications. The "all in one" platform is flexible and can be used either as a single modality imaging (PA/MRI/PET/SPECT) agent or as multi-modal agent combining two or more imaging techniques.

8.2 Future work

The intrinsic radiolabeling of CuS-Mn NPs was established as a platform to build on in the future. Conjugation synthesis of RGD-CuS-Mn NPs was developed and can be used for future *in vivo* imaging and toxicity studies.

8.2.1 Future directions for intrinsically radiolabeled CuS-Mn NPs

Further studies could focus on three directions:

1. Investigate the *in vivo* targeting merit of radiolabeled NP and perform pharmacokinetic and toxicity studies.
2. Investigate intrinsic radiolabeling of other radionuclides such as ^{52}Mn and ^{64}Cu to assess not only imaging performance, but also the effect of the radionuclide on the overall accumulation, retention and clearance, as well as toxicity related issues pertinent to the radionuclide.
3. Explore the combination of photo-thermal and radionuclide therapy guided by imaging. This approach could break new grounds in multi-modal therapy.

Appendix

Research Presentation and Manuscript for publications

- **Gawi A**., Gobalakrishnan S., Vijayaragavan V., Cicek H., Sun M., and Zweit J. "Image-Guided CuS-Mn Nanoparticles for Targeted Photo-thermal and Radiotherapy of Cancer"**,** poster presentation at Virginia Commonwealth University, Chemistry annual poster session (2016,2017 and 2018).
- **Gawi A**., Gobalakrishnan S., Cicek H., Elmekharam N., McDonagh P., Wang L. and Zweit J. "Multimodality Theranostic Copper Sulfide Nanoparticles", oral presentation at 50th Annual Meeting of Biomedical Engineering Society (BMES) 2018, Atlanta, Georgia.
- **Gawi A**., Gobalakrishnan S., Cicek H., Elmekharam N., McDonagh P., Wang L., Sun M. and Zweit J "Intrinsically Radiolabeled Copper Sulfide-Manganese Nanoparticles for Multimodality for *in vitro* and *in vivo* study" (Manuscript in preparation).
- **Gawi A**., Gobalakrishnan S., Cicek H., Elmekharam N., McDonagh P., Wang L., Sun M. and Zweit J "Manganese-Doped Copper Sulfide Nanoparticles as Dual MR and Photoacoustic Imaging Contrast Agent" (Manuscript in preparation).
- Rojas J., Umretiya R., Molina-Higgins M., **Gawi A**., Gobalakrishnan S., and Zweit J."Incorporation of ^{67}Cu within Luminescent lanthanide phosphate nanoparticles for theranostics" (Submitted for publication).

References

(1) Andreou, C.; Pal, S.; Rotter, L.; Yang, J.; Kircher, M. F. Molecular Imaging in Nanotechnology and Theranostics. *Mol. Imaging Biol.* **2017**, *19* (3), 363–372.

(2) Siddique, S.; Chow, J. C. L. Application of Nanomaterials in Biomedical Imaging and Cancer Therapy. *Nanomaterials* **2020**, *10* (9), 1–41.

(3) Ryu, J. H.; Lee, S.; Son, S.; Kim, S. H.; Leary, J. F.; Choi, K.; Kwon, I. C. Theranostic Nanoparticles for Future Personalized Medicine. *J. Control. Release* **2014**, *190*, 477–484.

(4) Jo, S. D.; Ku, S. H.; Won, Y. Y.; Kim, S. H.; Kwon, I. C. Targeted Nanotheranostics for Future Personalized Medicine: Recent Progress in Cancer Therapy. *Theranostics* **2016**, *6* (9), 1362–1377.

(5) Hoffman, D.; Hoffman, D. B. Hybrid PET / MRI Nanoparticle Development and Multi-Modal Imaging. **2013**.

(6) Sarko, D.; Eisenhut, M.; Haberkorn, U.; Mier, W. Bifunctional Chelators in the Design and Application of Radiopharmaceuticals for Oncological Diseases. *Curr. Med. Chem.* **2012**, *19* (17), 2667–2688.

(7) Cutler, C. S.; Hennkens, H. M.; Sisay, N.; Huclier-Markai, S.; Jurisson, S. S. Radiometals for Combined Imaging and Therapy. *Chem. Rev.* **2013**, *113* (2), 858–883.

(8) Cai, W.; Chen, K.; Mohamedali, K. A.; Cao, Q.; Gambhir, S. S.; Rosenblum, M. G.; Chen, X. PET of Vascular Endothelial Growth Factor Receptor Expression. *J. Nucl. Med.* **2006**, *47* (12), 2048–2056.

(9) Goel, S.; Chen, F.; Ehlerding, E. B.; Cai, W. Intrinsically Radiolabeled Nanoparticles: An Emerging Paradigm. *Small* **2014**, *10* (19), 3825–3830.

(10) Sun, M.; Hoffman, D.; Sundaresan, G.; Yang, L.; Lamichhane, N.; Zweit, J. Synthesis and Characterization of Intrinsically Radiolabeled Quantum Dots for Bimodal Detection. *Am. J. Nucl. Med. Mol. Imaging* **2012**, *2* (2), 122–12235.

(11) Yang, L.; Sundaresan, G.; Sun, M.; Jose, P.; Hoffman, D.; McDonagh, P. R.; Lamichhane, N.; Cutler, C. S.; Perez, J. M.; Zweit, J. Intrinsically Radiolabeled Multifunctional Cerium Oxide Nanoparticles for in Vivo Studies. *J. Mater. Chem. B* **2013**, *1* (10), 1421–1431.

(12) Hoffman, D.; Sun, M.; Yang, L.; McDonagh, P. R.; Corwin, F.; Sundaresan, G.; Wang, L.; Vijayaragavan, V.; Thadigiri, C.; Lamichhane, N.; et al. Intrinsically Radiolabelled [(59)Fe]-SPIONs for Dual MRI/Radionuclide Detection. *Am. J. Nucl. Med. Mol. Imaging* **2014**, *4* (6), 548–54860.

(13) McDonagh, P. R.; Sundaresan, G.; Yang, L.; Sun, M.; Mikkelsen, R.; Zweit, J. Biodistribution and PET Imaging of 89-Zirconium Labeled Cerium Oxide Nanoparticles Synthesized with Several Surface Coatings. *Nanomedicine Nanotechnology, Biol. Med.*

2018, *14* (4), 1429–1440.

(14) John, R. Global Cancer Facts & Figures 4 Th Edition-Special Section,the Obesity Epidemic. *Am. Cancer Soc.* **2018**, 76.

(15) Viale, P. H. The American Cancer Society's facts & figures. *Journal of the Advanced Practitioner in Oncology* 11, no. 2, **2020**, 135.

(16) Siegel, R. L.; Miller, K. D.; Jemal, A. Cancer Statistics, 2019. *CA. Cancer J. Clin.* **2019**, *69* (1), 7–34.

(17) Hanahan, D.; Weinberg, R.A. The hallmarks of cancer. *cell* 100, no. 1 **2000**, 57-70.

(18) Hanahan, D.; Weinberg, R. A. Hallmarks of Cancer: The next Generation. *Cell* **2011**, *144* (5), 646–674.

(19) Miller, K. D.; Nogueira, L.; Mariotto, A. B.; Rowland, J. H.; Yabroff, K. R.; Alfano, C. M.; Jemal, A.; Kramer, J. L.; Siegel, R. L. Cancer Treatment and Survivorship Statistics, 2019. *CA. Cancer J. Clin.* **2019**, *69* (5), 363–385.

(20) Young, M. R. I. Cancer Immunology with a Focus on Understudied Cancers as Targets for Immunotherapy. *Int. J. Mol. Sci.* **2017**, *18* (1), 10–13.

(21) Leclerc, M.; Mezquita, L.; De Nerville, G. G.; Tihy, I.; Malenica, I.; Chouaib, S.; Mami-Chouaib, F. Recent Advances in Lung Cancer Immunotherapy: Input of T-Cell Epitopes Associated with Impaired Peptide Processing. *Front. Immunol.* **2019**, *10* (JUL), 1–8.

(22) Salvati, E.; Stellacci, F.; Krol, S. Nanosensors for Early Cancer Detection and for Therapeutic Drug Monitoring. *Nanomedicine* **2015**, *10* (23), 3495–3512.

(23) Adorno-Cruz, V.; Kibria, G.; Liu, X.; Doherty, M.; Junk, D. J.; Guan, D.; Hubert, C.; Venere, M.; Mulkearns-Hubert, E.; Sinyuk, M.; et al. Cancer Stem Cells: Targeting the Roots of Cancer, Seeds of Metastasis, and Sources of Therapy Resistance. *Cancer Res.* **2015**, *75* (6), 924–929.

(24) Doherty, M. R.; Smigiel, J. M.; Junk, D. J.; Jackson, M. W. Cancer Stem Cell Plasticity Drives Therapeutic Resistance. *Cancers (Basel).* **2016**, *8* (1), 1–13.

(25) Chen, H. H. W.; Kuo, M. T. Improving Radiotherapy in Cancer Treatment: Promises and Challenges. *Oncotarget* **2017**, *8* (37), 62742–62758.

(26) Senan, S.; De Ruysscher, D. Critical Review of PET-CT for Radiotherapy Planning in Lung Cancer. *Crit. Rev. Oncol. Hematol.* **2005**, *56* (3), 345–351.

(27) Sano, K.; Kanada, Y.; Kanazaki, K.; Ding, N.; Ono, M.; Saji, H. Brachytherapy with Intratumoral Injections of Radiometal-Labeled Polymers That Thermoresponsively Self-

Aggregate in Tumor Tissues. *J. Nucl. Med.* **2017**, *58* (9), 1380–1385.

(28) Skowronek, J. Current Status of Brachytherapy in Cancer Treatment – Short Overview. *J. Contemp. Brachytherapy* **2017**, *9* (6), 581–589.

(29) Baskar, R.; Lee, K. A.; Yeo, R.; Yeoh, K. W. Cancer and Radiation Therapy: Current Advances and Future Directions. *Int. J. Med. Sci.* **2012**, *9* (3), 193–199.

(30) Song, G.; Cheng, L.; Chao, Y.; Yang, K.; Liu, Z. Emerging Nanotechnology and Advanced Materials for Cancer Radiation Therapy. *Adv. Mater.* **2017**, *29* (32), 1–26.

(31) Nurgali, K.; Jagoe, R. T.; Abalo, R. Editorial: Adverse Effects of Cancer Chemotherapy: Anything New to Improve Tolerance and Reduce Sequelae? *Front. Pharmacol.* **2018**, *9* (MAR), 1–3.

(32) Senapati, S.; Mahanta, A. K.; Kumar, S.; Maiti, P. Controlled Drug Delivery Vehicles for Cancer Treatment and Their Performance. *Signal Transduct. Target. Ther.* **2018**, *3* (1), 1–19.

(33) Yan, L.; Shen, J.; Wang, J.; Yang, X.; Dong, S.; Lu, S. Nanoparticle-Based Drug Delivery System: A Patient-Friendly Chemotherapy for Oncology. *Dose-Response* **2020**, *18* (3).

(34) Abotaleb, M.; Kubatka, P.; Caprnda, M.; Varghese, E.; Zolakova, B.; Zubor, P.; Opatrilova, R.; Kruzliak, P.; Stefanicka, P.; Büsselberg, D. Chemotherapeutic Agents for the Treatment of Metastatic Breast Cancer: An Update. *Biomed. Pharmacother.* **2018**, *101* (August 2017), 458–477.

(35) Ke, X.; Shen, L. Molecular Targeted Therapy of Cancer: The Progress and Future Prospect. *Front. Lab. Med.* **2017**, *1* (2), 69–75.

(36) Marcu, L.; Bezak, E.; Allen, B. J. Global Comparison of Targeted Alpha vs Targeted Beta Therapy for Cancer: In Vitro, in Vivo and Clinical Trials. *Crit. Rev. Oncol. Hematol.* **2018**, *123* (July 2017), 7–20.

(37) Makvandi, M.; Dupis, E.; Engle, J. W.; Nortier, F. M.; Fassbender, M. E.; Simon, S.; Birnbaum, E. R.; Atcher, R. W.; John, K. D.; Rixe, O.; et al. Alpha-Emitters and Targeted Alpha Therapy in Oncology: From Basic Science to Clinical Investigations. *Target. Oncol.* **2018**, *13* (2), 189–203.

(38) Baudino, T. Targeted Cancer Therapy: The Next Generation of Cancer Treatment. *Curr. Drug Discov. Technol.* **2015**, *12* (1), 3–20.

(39) Lee, Y. T.; Tan, Y. J.; Oon, C. E. Molecular Targeted Therapy: Treating Cancer with Specificity. *Eur. J. Pharmacol.* **2018**, *834* (July), 188–196.

(40) Banerjee, S. R.; Kumar, V.; Lisok, A.; Chen, J.; Minn, I.; Brummet, M.; Boinapally, S.; Cole, M.; Ngen, E.; Wharram, B.; et al. 177Lu-Labeled Low-Molecular-Weight Agents for PSMA-Targeted Radiopharmaceutical Therapy. *Eur. J. Nucl. Med. Mol. Imaging* **2019**, *46*

(12), 2545–2557.

(41) Hofman, M. S.; Violet, J.; Hicks, R. J.; Ferdinandus, J.; Ping Thang, S.; Akhurst, T.; Iravani, A.; Kong, G.; Ravi Kumar, A.; Murphy, D. G.; et al. [177 Lu]-PSMA-617 Radionuclide Treatment in Patients with Metastatic Castration-Resistant Prostate Cancer (LuPSMA Trial): A Single-Centre, Single-Arm, Phase 2 Study. *Lancet Oncol.* **2018**, *19* (6), 825–833.

(42) Kratochwil, C.; Bruchertseifer, F.; Rathke, H.; Bronzel, M.; Apostolidis, C.; Weichert, W.; Haberkorn, U.; Giesel, F. L.; Morgenstern, A. Targeted A-Therapy of Metastatic Castration-Resistant Prostate Cancer with 225Ac-PSMA-617: Dosimetry Estimate and Empiric Dose Finding. *J. Nucl. Med.* **2017**, *58* (10), 1624–1631.

(43) Lazzari, C.; Karachaliou, N.; Bulotta, A.; Viganó, M.; Mirabile, A.; Brioschi, E.; Santarpia, M.; Gianni, L.; Rosell, R.; Gregorc, V. Combination of Immunotherapy with Chemotherapy and Radiotherapy in Lung Cancer: Is This the Beginning of the End for Cancer? *Ther. Adv. Med. Oncol.* **2018**, *10*, 1–12.

(44) Liu, Y.; Bhattarai, P.; Dai, Z.; Chen, X. Photothermal Therapy and Photoacoustic Imaging: Via Nanotheranostics in Fighting Cancer. *Chem. Soc. Rev.* **2019**, *48* (7), 2053–2108.

(45) Kaur, P.; Hurwitz, M. D.; Krishnan, S.; Asea, A. Combined Hyperthermia and Radiotherapy for the Treatment of Cancer. *Cancers (Basel).* **2011**, *3* (4), 3799–3823.

(46) Mantso, T.; Vasileiadis, S.; Anestopoulos, I.; Voulgaridou, G. P.; Lampri, E.; Botaitis, S.; Kontomanolis, E. N.; Simopoulos, C.; Goussetis, G.; Franco, R.; et al. Hyperthermia Induces Therapeutic Effectiveness and Potentiates Adjuvant Therapy with Non-Targeted and Targeted Drugs in an in Vitro Model of Human Malignant Melanoma. *Sci. Rep.* **2018**, *8* (1), 1–16.

(47) Wang, J.; Qiu, J. A Review of Organic Nanomaterials in Photothermal Cancer Therapy. *Cancer Res. Front.* **2016**, *2* (1), 67–84.

(48) Kaur, P.; Aliru, M. L.; Chadha, A. S.; Asea, A.; Krishnan, S. Hyperthermia Using Nanoparticles - Promises and Pitfalls. *Int. J. Hyperth.* **2016**, *32* (1), 76–88.

(49) Vines, J. B.; Yoon, J. H.; Ryu, N. E.; Lim, D. J.; Park, H. Gold Nanoparticles for Photothermal Cancer Therapy. *Front. Chem.* **2019**, *7* (APR), 1–16.

(50) Xiao, Z. CuS Nanoparticles: Clinically Favorable Materials for Photothermal Applications? *Nanomedicine* **2014**, *9* (3), 373–375.

(51) Gao, W.; Sun, Y.; Cai, M.; Zhao, Y.; Cao, W.; Liu, Z.; Cui, G.; Tang, B. Copper Sulfide Nanoparticles as a Photothermal Switch for TRPV1 Signaling to Attenuate Atherosclerosis. *Nat. Commun.* **2018**, *9* (1), 1–10.

(52) Liang, L.; Peng, S.; Yuan, Z.; Wei, C.; He, Y.; Zheng, J.; Gu, Y.; Chen, H. Biocompatible Tumor-Targeting Nanocomposites Based on CuS for Tumor Imaging and Photothermal Therapy. *RSC Adv.* **2018**, *8* (11), 6013–6026.

(53) Farkona, S.; Diamandis, E. P.; Blasutig, I. M. Cancer Immunotherapy: The Beginning of the End of Cancer? *BMC Med.* **2016**, *14* (1), 1–18.

(54) Oiseth, S. J.; Aziz, M. S. Cancer Immunotherapy: A Brief Review of the History, Possibilities, and Challenges Ahead. *J. Cancer Metastasis Treat.* **2017**, *3* (10), 250.

(55) Romano, G.; Kwong, L. N. Diagnostic and Therapeutic Applications of MiRNA-Based Strategies to Cancer Immunotherapy. *Cancer Metastasis Rev.* **2018**, *37* (1), 45–53.

(56) Homet Moreno, B.; Ribas, A. Anti-Programmed Cell Death Protein-1/Ligand-1 Therapy in Different Cancers. *Br. J. Cancer* **2015**, *112* (9), 1421–1427.

(57) Misra, R.; Acharya, S.; Sahoo, S. K. Cancer Nanotechnology: Application of Nanotechnology in Cancer Therapy. *Drug Discov. Today* **2010**, *15* (19–20), 842–850.

(58) Bhise, K.; Sau, S.; Alsaab, H.; Kashaw, S. K.; Tekade, R. K.; Iyer, A. K. Nanomedicine for Cancer Diagnosis and Therapy: Advancement, Success and Structure-Activity Relationship. *Ther. Deliv.* **2017**, *8* (11), 1003–1018.

(59) Jain, K. K. *The Handbook of Nanomedicine, Third Edition*; 2017.

(60) Etheridge, M. L.; Campbell, S. A.; Erdman, A. G.; Haynes, C. L.; Wolf, S. M.; McCullough Jeffrey. The Big Picture on Small Medicine. **2013**, *9* (1), 1–14.

(61) Barenholz, Y. Doxil® - The First FDA-Approved Nano-Drug: Lessons Learned. *J. Control. Release* **2012**, *160* (2), 117–134.

(62) Bobo, D.; Robinson, K. J.; Islam, J.; Thurecht, K. J.; Corrie, S. R. Nanoparticle-Based Medicines: A Review of FDA-Approved Materials and Clinical Trials to Date. *Pharm. Res.* **2016**, *33* (10), 2373–2387.

(63) Jeevanandam, J.; Barhoum, A.; Chan, Y. S.; Dufresne, A.; Danquah, M. K. Review on Nanoparticles and Nanostructured Materials: History, Sources, Toxicity and Regulations. *Beilstein J. Nanotechnol.* **2018**, *9* (1), 1050–1074.

(64) Nel, A.; Ruoslahti, E.; Meng, H. New Insights into "Permeability" as in the Enhanced Permeability and Retention Effect of Cancer Nanotherapeutics. *ACS Nano* **2017**, *11* (10), 9567–9569.

(65) Li, C. A Targeted Approach to Cancer Imaging and Therapy. *Nat. Mater.* **2014**, *13* (2), 110–115.

(66) Bai, J.; Liu, Y.; Jiang, X. Multifunctional PEG-GO/CuS Nanocomposites for near-Infrared Chemo-Photothermal Therapy. *Biomaterials* **2014**, *35* (22), 5805–5813.

(67) Shen, Z.; Chen, T.; Ma, X.; Ren, W.; Zhou, Z.; Zhu, G.; Zhang, A.; Liu, Y.; Song, J.; Li, Z.; et al. Multifunctional Theranostic Nanoparticles Based on Exceedingly Small Magnetic Iron Oxide Nanoparticles for T1-Weighted Magnetic Resonance Imaging and

Chemotherapy. *ACS Nano* **2017**, *11* (11), 10992–11004.

(68) Zhou, M.; Li, J.; Liang, S.; Sood, A. K.; Liang, D.; Li, C. CuS Nanodots with Ultrahigh Efficient Renal Clearance for Positron Emission Tomography Imaging and Image-Guided Photothermal Therapy. *ACS Nano* **2015**, *9* (7), 7085–7096.

(69) Yang, Y.; Lin, Y.; Di, D.; Zhang, X.; Wang, D.; Zhao, Q.; Wang, S. Gold Nanoparticle-Gated Mesoporous Silica as Redox-Triggered Drug Delivery for Chemo-Photothermal Synergistic Therapy. *J. Colloid Interface Sci.* **2017**, *508*, 323–331.

(70) Kim, D.; Kim, J.; Park, Y. Il; Lee, N.; Hyeon, T. Recent Development of Inorganic Nanoparticles for Biomedical Imaging. *ACS Cent. Sci.* **2018**, *4* (3), 324–336.

(71) Han, X.; Xu, K.; Taratula, O.; Farsad, K. Applications of Nanoparticles in Biomedical Imaging. *Nanoscale* **2019**, *11* (3), 799–819.

(72) Pellico, J.; Gawne, P. J.; T. M. De Rosales, R. Radiolabelling of Nanomaterials for Medical Imaging and Therapy. *Chem. Soc. Rev.* **2021**, *50* (5), 3355–3423.

(73) Peltek, O. O.; Muslimov, A. R.; Zyuzin, M. V.; Timin, A. S. Current Outlook on Radionuclide Delivery Systems: From Design Consideration to Translation into Clinics. *J. Nanobiotechnology* **2019**, *17* (1), 1–34.

(74) Patra, J. K.; Das, G.; Fraceto, L. F.; Campos, E. V. R.; Rodriguez-Torres, M. del P.; Acosta-Torres, L. S.; Diaz-Torres, L. A.; Grillo, R.; Swamy, M. K.; Sharma, S.; et al. Nano Based Drug Delivery Systems: Recent Developments and Future Prospects. *J. Nanobiotechnology* **2018**, *16* (1), 1–33.

(75) Feng, Q.; Zhang, Y.; Zhang, W.; Shan, X.; Yuan, Y.; Zhang, H.; Hou, L.; Zhang, Z. Tumor-Targeted and Multi-Stimuli Responsive Drug Delivery System for near-Infrared Light Induced Chemo-Phototherapy and Photoacoustic Tomography. *Acta Biomater.* **2016**, *38*, 129–142.

(76) Zhou, M.; Song, S.; Zhao, J.; Tian, M.; Li, C. Theranostic CuS Nanoparticles Targeting Folate Receptors for PET Image-Guided Photothermal Therapy. *J. Mater. Chem. B* **2015**, *3* (46), 8939–8948.

(77) Wang, L. Synthetic Methods of CuS Nanoparticles and Their Applications for Imaging and Cancer Therapy. *RSC Adv.* **2016**, *6* (86), 82596–82615.

(78) Wang, Z.; Huang, P.; Jacobson, O.; Wang, Z.; Liu, Y.; Lin, L.; Lin, J.; Lu, N.; Zhang, H.; Tian, R.; et al. Biomineralization-Inspired Synthesis of Copper Sulfide-Ferritin Nanocages as Cancer Theranostics. *ACS Nano* **2016**, *10* (3), 3453–3460.

(79) Zha, Z.; Zhang, S.; Deng, Z.; Li, Y.; Li, C.; Dai, Z. Enzyme-Responsive Copper Sulphide Nanoparticles for Combined Photoacoustic Imaging, Tumor-Selective Chemotherapy and Photothermal Therapy. *Chem. Commun.* **2013**, *49* (33), 3455–3457.

(80) Guo, L.; Yan, D. D.; Yang, D.; Li, Y.; Wang, X.; Zalewski, O.; Yan, B.; Lu, W. Combinatorial Photothermal and Immuno Cancer Therapy Using Chitosan-Coated Hollow Copper Sulfide Nanoparticles. *ACS Nano* **2014**, *8* (6), 5670–5681.

(81) Guo, L.; Panderi, I.; Yan, D. D.; Szulak, K.; Li, Y.; Chen, Y. T.; Ma, H.; Niesen, D. B.; Seeram, N.; Ahmed, A.; et al. A Comparative Study of Hollow Copper Sulfide Nanoparticles and Hollow Gold Nanospheres on Degradability and Toxicity. *ACS Nano* **2013**, *7* (10), 8780–8793.

(82) Zhou, M.; Tian, M.; Li, C. Copper-Based Nanomaterials for Cancer Imaging and Therapy. *Bioconjug. Chem.* **2016**, *27* (5), 1188–1199.

(83) Zeineldin, R. Nanotechnology for Cancer Screening and Diagnosis. *Biomater. Cancer Ther. Diagnosis, Prev. Ther.* **2013**, 137–164.

(84) Kim, P. S.; Djazayeri, S.; Zeineldin, R. Novel Nanotechnology Approaches to Diagnosis and Therapy of Ovarian Cancer. *Gynecol. Oncol.* **2011**, *120* (3), 393–403.

(85) Doane, T. L.; Burda, C. The Unique Role of Nanoparticles in Nanomedicine: Imaging, Drug Delivery and Therapy. *Chem. Soc. Rev.* **2012**, *41* (7), 2885–2911.

(86) Din, F. U.; Aman, W.; Ullah, I.; Qureshi, O. S.; Mustapha, O.; Shafique, S.; Zeb, A. Effective Use of Nanocarriers as Drug Delivery Systems for the Treatment of Selected Tumors. *Int. J. Nanomedicine* **2017**, *12*, 7291–7309.

(87) Dang, Y.; Guan, J. Nanoparticle-Based Drug Delivery Systems for Cancer Therapy. *Smart Mater. Med.* **2020**, *1* (March), 10–19.

(88) Al-fartusie, F. S.; Mohssan, S. N. Essential Trace Elements and Their Vital Roles in Human Body. *Indian J. Adv. Chem. Sci.* **2017**, *5* (3), 127–136.

(89) Pysz, M. A.; Gambhir, S. S.; Willmann, J. K. Molecular Imaging: Current Status and Emerging Strategies. *Clin. Radiol.* **2010**, *65* (7), 500–516.

(90) Michalski, M. H.; Chen, X. Molecular Imaging in Cancer Treatment. *Eur. J. Nucl. Med. Mol. Imaging* **2011**, *38* (2), 358–377.

(91) James, M. L.; Gambhir, S. S. A Molecular Imaging Primer: Modalities, Imaging Agents, and Applications. *Physiol. Rev.* **2012**, *92* (2), 897–965.

(92) Spick, C.; Herrmann, K.; Czernin, J. 18F-FDG PET/CT and PET/MRI Perform Equally Well in Cancer: Evidence from Studies on More than 2,300 Patients. *J. Nucl. Med.* **2016**, *57* (3), 420–430.

(93) Badawi, R. D.; Shi, H.; Hu, P.; Chen, S.; Xu, T.; Price, P. M.; Ding, Y.; Spencer, B. A.; Nardo, L.; Liu, W.; et al. First Human Imaging Studies with the Explorer Total-Body PET Scanner. *J. Nucl. Med.* **2019**, *60* (3), 299–303.

(94) Lakshmanan, A.; Lu, G. J.; Farhadi, A.; Nety, S. P.; Kunth, M.; Lee-Gosselin, A.; Maresca, D.; Bourdeau, R. W.; Yin, M.; Yan, J.; et al. Preparation of Biogenic Gas Vesicle Nanostructures for Use as Contrast Agents for Ultrasound and MRI. *Nat. Protoc.* **2017**, *12* (10), 2050–2080.

(95) Li, Y.; Chen, Y.; Du, M.; Chen, Z. Y. Ultrasound Technology for Molecular Imaging: From Contrast Agents to Multimodal Imaging. *ACS Biomater. Sci. Eng.* **2018**, *4* (8), 2716–2728.

(96) Zaidi, H. *Molecular Imaging of Small Animals: Instrumentation and Applications*; 2014; Vol. 9781493908.

(97) Massoud, T. F.; Gambhir, S. S. Molecular Imaging in Living Subjects: Seeing Fundamental Biological Processes in a New Light. *Genes Dev.* **2003**, *17* (5), 545–580.

(98) Zhang, S.; Joseph, A. A.; Voit, D.; Schaetz, S.; Merboldt, K.-D.; Unterberg-Buchwald, C.; Hennemuth, A.; Lotz, J.; Frahm, J. Real-Time Magnetic Resonance Imaging of Cardiac Function and Flow-Recent Progress. *Quant. Imaging Med. Surg.* **2014**, *4* (5), 313–329.

(99) Birur, B.; Kraguljac, N. V.; Shelton, R. C.; Lahti, A. C. Brain Structure, Function, and Neurochemistry in Schizophrenia and Bipolar Disorder- A Systematic Review of the Magnetic Resonance Neuroimaging Literature. *npj Schizophr.* **2017**, *3* (1), 1–15.

(100) Shapiro, L.; Harish, M.; Hargreaves, B.; Staroswiecki, E.; Gold, G. Advances in Musculoskeletal MRI: Technical Considerations. *J. Magn. Reson. Imaging* **2012**, *36* (4), 775–787.

(101) Park, C. A.; Kang, C. K.; Kim, Y. B.; Cho, Z. H. Advances in MR Angiography with 7T MRI: From Microvascular Imaging to Functional Angiography. *Neuroimage* **2018**, *168* (January 2017), 269–278.

(102) McRobbie, D. W.; Moore, E. A.; Graves, M. J. MRI from Picture to Proton. *MRI from Pict. to Prot.* **2017**, 1–383.

(103) Tognarelli, J. M.; Dawood, M.; Shariff, M. I. F.; Grover, V. P. B.; Crossey, M. M. E.; Cox, I. J.; Taylor-Robinson, S. D.; McPhail, M. J. W. Magnetic Resonance Spectroscopy: Principles and Techniques: Lessons for Clinicians. *J. Clin. Exp. Hepatol.* **2015**, *5* (4), 320–328.

(104) Na, H. Bin; Song, I. C.; Hyeon, T. Inorganic Nanoparticles for MRI Contrast Agents. *Adv. Mater.* **2009**, *21* (21), 2133–2148.

(105) Shokrollahi, H. Contrast agents for MRI. *Materials Science and Engineering.* **2013** *C* 33, no. 8 ,4485-4497.

(106) Samadi, K.; Salazar, G. M. Role of Imaging in the Diagnosis of Vascular Malformations Vascular Malformations. *Cardiovasc. Diagn. Ther.* **2019**, *9* (S1), S143–S151.

(107) Ramalho, J.; Semelka, R. C.; Ramalho, M.; Nunes, R. H.; AlObaidy, M.; Castillo, M. Gadolinium-Based Contrast Agent Accumulation and Toxicity: An Update. *Am. J. Neuroradiol.* **2016**, *37* (7), 1192–1198.

(108) Guo, B. J.; Yang, Z. L.; Zhang, L. J. Gadolinium Deposition in Brain: Current Scientific Evidence and Future Perspectives. *Front. Mol. Neurosci.* **2018**, *11* (September), 1–12.

(109) Zhen, Z.; Xie, J. Development of Manganese-Based Nanoparticles as Contrast Probes for Magnetic Resonance Imaging. *Theranostics* **2012**, *2* (1), 45–54.

(110) Qian, X.; Han, X.; Yu, L.; Xu, T.; Chen, Y. Manganese-Based Functional Nanoplatforms: Nanosynthetic Construction, Physiochemical Property, and Theranostic Applicability. *Adv. Funct. Mater.* **2020**, *30* (3), 1–40. https://doi.org/10.1002/adfm.201907066.

(111) Del Guerra, A.; Belcari, N.; Bisogni, M. Positron Emission Tomography: Its 65 Years. *Riv. del Nuovo Cim.* **2016**, *39* (4), 155–223.

(112) Foster, B.; Bagci, U.; Mansoor, A.; Xu, Z.; Mollura, D. J. A Review on Segmentation of Positron Emission Tomography Images. *Comput. Biol. Med.* **2014**, *50*, 76–96.

(113) Khalil, M. M.; Tremoleda, J. L.; Bayomy, T. B.; Gsell, W. Molecular SPECT Imaging: An Overview. *Int. J. Mol. Imaging* **2011**, *2011*, 1–15.

(114) Rahmim, A.; Zaidi, H. Pet versus Spect: Strengths, Limitations and Challenges. *Nucl. Med. Commun.* **2008**, *29* (3), 193–207.

(115) Delouya, G.; Igidbashian, L.; Houle, A.; Bélair, M.; Boucher, L.; Cohade, C.; Beaulieu, S.; Filion, É. J.; Coulombe, G.; Hinse, M.; et al. 18F-FDG-PET Imaging in Radiotherapy Tumor Volume Delineation in Treatment of Head and Neck Cancer. *Radiother. Oncol.* **2011**, *101* (3), 362–368.

(116) Almuhaideb, A.; Papathanasiou, N.; Bomanji, J. 18F-FDG PET/CT Imaging in Oncology. *Ann. Saudi Med.* **2011**, *31* (1), 3–13.

(117) Lenzo, N.; Meyrick, D.; Turner, J. Review of Gallium-68 PSMA PET/CT Imaging in the Management of Prostate Cancer. *Diagnostics* **2018**, *8* (1), 16.

(118) Petersen, L. J.; Nielsen, J. B.; Langkilde, N. C.; Petersen, A.; Afshar-Oromieh, A.; De Souza, N. M.; De Paepe, K.; Fisker, R. V.; Arp, D. T.; Carl, J.; et al. 68Ga-PSMA PET/CT Compared with MRI/CT and Diffusion-Weighted MRI for Primary Lymph Node Staging Prior to Definitive Radiotherapy in Prostate Cancer: A Prospective Diagnostic Test Accuracy Study. *World J. Urol.* **2020**, *38* (4), 939–948.

(119) Pimlott, S. L.; Sutherland, A. Molecular Tracers for the PET and SPECT Imaging of Disease. *Chem. Soc. Rev.* **2011**, *40* (1), 149–162.

(120) Pirovano, G.; Roberts, S.; Kossatz, S.; Reiner, T. Optical Imaging Modalities: Principles and Applications in Preclinical Research and Clinical Settings. *J. Nucl. Med.* **2020**, *61* (10),

1419–1427.

(121) Rosencwaig, A.; Gersho, A. Theory of the Photoacoustic Effect with Solids. *J. Appl. Phys.* **1976**, *47* (1), 64–69.

(122) Ntziachristos, V.; Razansky, D. Molecular Imaging by Means of Multispectral Optoacoustic Tomography (MSOT). *Chem. Rev.* **2010**, *110* (5), 2783–2794.

(123) Taruttis, A.; Ntziachristos, V. Advances in Real-Time Multispectral Optoacoustic Imaging and Its Applications. *Nat. Photonics* **2015**, *9* (4), 219–227.

(124) Taruttis, A.; Wildgruber, M.; Kosanke, K.; Beziere, N.; Licha, K.; Haag, R.; Aichler, M.; Walch, A.; Rummeny, E.; Ntziachristos, V. Multispectral Optoacoustic Tomography of Myocardial Infarction. *Photoacoustics* **2013**, *1* (1), 3–8.

(125) Gottschalk, S.; Felix Fehm, T.; Luís Deán-Ben, X.; Razansky, D. Noninvasive Real-Time Visualization of Multiple Cerebral Hemodynamic Parameters in Whole Mouse Brains Using Five-Dimensional Optoacoustic Tomography. *J. Cereb. Blood Flow Metab.* **2015**, *35* (February 2014), 531–535.

(126) Laufer, J. G.; Zhang, E. Z.; Treeby, B. E.; Cox, B. T.; Beard, P. C.; Johnson, P.; Pedley, B. In Vivo Preclinical Photoacoustic Imaging of Tumor Vasculature Development and Therapy. *J. Biomed. Opt.* **2012**, *17* (5), 1.

(127) Ruan, Q.; Xi, L.; Boye, S. L.; Han, S.; Chen, Z. J.; Hauswirth, W. W.; Lewin, A. S.; Boulton, M. E.; Law, B. K.; Jiang, W. G.; et al. Development of an Anti-Angiogenic Therapeutic Model Combining ScAAV2-Delivered SiRNAs and Noninvasive Photoacoustic Imaging of Tumor Vasculature Development. *Cancer Lett.* **2013**, *332* (1), 120–129.

(128) Buehler, A.; Kacprowicz, M.; Taruttis, A.; Ntziachristos, V. Real-Time Handheld Multispectral Optoacoustic Imaging. *Opt. Lett.* **2013**, *38* (9), 1404.

(129) Taruttis, A.; Timmermans, A. C.; Wouters, P. C.; Kacprowicz, M.; Van Dam, G. M.; Ntziachristos, V. Optoacoustic Imaging of Human Vasculature: Feasibility by Using a Handheld Probe. *Radiology* **2016**, *281* (1), 256–263.

(130) Tzoumas, S.; Nunes, A.; Olefir, I.; Stangl, S.; Symvoulidis, P.; Glasl, S.; Bayer, C.; Multhoff, G.; Ntziachristos, V. Eigenspectra Optoacoustic Tomography Achieves Quantitative Blood Oxygenation Imaging Deep in Tissues. *Nat. Commun.* **2016**, *7* (May), 1–10.

(131) Stoffels, I.; Morscher, S.; Helfrich, I.; Hillen, U.; Leyh, J.; Lehy, J.; Burton, N. C.; Sardella, T. C. P.; Claussen, J.; Poeppel, T. D.; et al. Metastatic Status of Sentinel Lymph Nodes in Melanoma Determined Noninvasively with Multispectral Optoacoustic Imaging. *Sci. Transl. Med.* **2015**, *7* (317).

(132) Yao, D.-K.; Maslov, K.; Shung, K. K.; Zhou, Q.; Wang, L. V. In Vivo Label-Free Photoacoustic Microscopy of Cell Nuclei by Excitation of DNA and RNA. *Opt. Lett.* **2010**,

35 (24), 4139.

(133) Taruttis, A.; Van Dam, G. M.; Ntziachristos, V. Mesoscopic and Macroscopic Optoacoustic Imaging of Cancer. *Cancer Res.* **2015**, *75* (8), 1548–1559.

(134) Ho, C. J. H.; Balasundaram, G.; Driessen, W.; McLaren, R.; Wong, C. L.; Dinish, U. S.; Attia, A. B. E.; Ntziachristos, V.; Olivo, M. Multifunctional Photosensitizer-Based Contrast Agents for Photoacoustic Imaging. *Sci. Rep.* **2014**, *4*, 1–6.

(135) Hellebust, A.; Richards-Kortum, R. Advances in Molecular Imaging: Targeted Optical Contrast Agents for Cancer Diagnostics. *Nanomedicine* **2012**, *7* (3), 429–445.

(136) Li, M. L.; Oh, J. T.; Xie, X.; Ku, G.; Wang, W.; Li, C.; Lungu, G.; Stoica, G.; Wang, L. V. Simultaneous Molecular and Hypoxia Imaging of Brain Tumors in Vivo Using Spectroscopic Photoacoustic Tomography. *Proc. IEEE* **2008**, *96* (3), 481–489.

(137) Levi, J.; Kothapalli, S. R.; Bohndiek, S.; Yoon, J. K.; Dragulescu-Andrasi, A.; Nielsen, C.; Tisma, A.; Bodapati, S.; Gowrishankar, G.; Yan, X.; et al. Molecular Photoacoustic Imaging of Follicular Thyroid Carcinoma. *Clin. Cancer Res.* **2013**, *19* (6), 1494–1502.

(138) Krumholz, A.; Shcherbakova, D. M.; Xia, J.; Wang, L. V.; Verkhusha, V. V. Multicontrast Photoacoustic in Vivo Imaging Using Near-Infrared Fluorescent Proteins. *Sci. Rep.* **2014**, *4*, 1–7.

(139) Gujrati, V.; Mishra, A.; Ntziachristos, V. Molecular Imaging Probes for Multi-Spectral Optoacoustic Tomography. *Chem. Commun.* **2017**, *53* (34), 4653–4672.

(140) Pejjai, B.; Reddivari, M.; Kotte, T. R. R. Phase Controllable Synthesis of CuS Nanoparticles by Chemical Co-Precipitation Method: Effect of Copper Precursors on the Properties of CuS. *Mater. Chem. Phys.* **2020**, *239* (May 2019).

(141) Aliev, R. A.; Belyshev, S. S.; Kuznetsov, A. A.; Dzhilavyan, L. Z.; Khankin, V. V.; Aleshin, G. Y.; Kazakov, A. G.; Priselkova, A. B.; Kalmykov, S. N.; Ishkhanov, B. S. Photonuclear Production and Radiochemical Separation of Medically Relevant Radionuclides: 67Cu. *J. Radioanal. Nucl. Chem.* **2019**, *321* (1), 125–132.

(142) Kikuchi, M.; Clump, D. A.; Srivastava, R. M.; Sun, L.; Zeng, D.; Diaz-Perez, J. A.; Anderson, C. J.; Edwards, W. B.; Ferris, R. L. Preclinical ImmunoPET/CT Imaging Using Zr-89-Labeled Anti-PD-L1 Monoclonal Antibody for Assessing Radiation-Induced PD-L1 Upregulation in Head and Neck Cancer and Melanoma. *Oncoimmunology* **2017**, *6* (7).

(143) Peng, S.; He, Y.; Er, M.; Sheng, Y.; Gu, Y.; Chen, H. Biocompatible CuS-Based Nanoplatforms for Efficient Photothermal Therapy and Chemotherapy: In Vivo. *Biomater. Sci.* **2017**, *5* (3), 475–484.

(144) Cai, H.; Xie, F.; Mulgaonkar, A.; Chen, L.; Sun, X. Nanoparticles for Targeted Imaging of Orthotopic Prostate Cancer. **2018**, *13* (May), 1695–1705.

(145) Pelaz, B.; Alexiou, C.; Alvarez-Puebla, R. A.; Alves, F.; Andrews, A. M.; Ashraf, S.; Balogh, L. P.; Ballerini, L.; Bestetti, A.; Brendel, C.; et al. Diverse Applications of Nanomedicine. *ACS Nano* **2017**, *11* (3), 2313–2381.

(146) Yang, W.; Guo, W.; Le, W.; Lv, G.; Zhang, F.; Shi, L.; Wang, X.; Wang, J.; Wang, S.; Chang, J.; et al. Albumin-Bioinspired Gd:CuS Nanotheranostic Agent for in Vivo Photoacoustic/Magnetic Resonance Imaging-Guided Tumor-Targeted Photothermal Therapy. *ACS Nano* **2016**, *10* (11), 10245–10257.

(147) Hao, D.; Ai, T.; Goerner, F.; Hu, X.; Runge, V. M.; Tweedle, M. MRI Contrast Agents: Basic Chemistry and Safety. *J. Magn. Reson. Imaging* **2012**, *36* (5), 1060–1071.

(148) Gao, D.; Zhang, P.; Liu, C.; Chen, C.; Gao, G.; Wu, Y.; Sheng, Z.; Song, L.; Cai, L. Compact Chelator-Free Ni-Integrated CuS Nanoparticles with Tunable near-Infrared Absorption and Enhanced Relaxivity for in Vivo Dual-Modal Photoacoustic/MR Imaging. *Nanoscale* **2015**, *7* (42), 17631–17636.

(149) Wang, Z.; Yu, W.; Yu, N.; Li, X.; Feng, Y.; Geng, P.; Wen, M.; Li, M.; Zhang, H.; Chen, Z. Construction of CuS@Fe-MOF Nanoplatforms for MRI-Guided Synergistic Photothermal-Chemo Therapy of Tumors. *Chem. Eng. J.* **2020**, *400* (May).

(150) Danhier, F.; Breton, A. Le; Préat, V. RGD-Based Strategies to Target Alpha(v) Beta(3) Integrin in Cancer Therapy and Diagnosis. *Mol. Pharm.* **2012**, *9* (11), 2961–2973.

(151) Cui, L.; Xiong, C.; Zhou, M.; Shi, S.; Chow, D. S. L.; Li, C. Integrin Avβ3-Targeted [64 Cu]CuS Nanoparticles for PET/CT Imaging and Photothermal Ablation Therapy. *Bioconjug. Chem.* **2018**, *29* (12), 4062–4071.

(152) Yan, H.; Chen, J.; Li, Y.; Bai, Y.; Wu, Y.; Sheng, Z.; Song, L.; Liu, C.; Zhang, H. Ultrasmall Hybrid Protein-Copper Sulfide Nanoparticles for Targeted Photoacoustic Imaging of Orthotopic Hepatocellular Carcinoma with a High Signal-to-Noise Ratio. *Biomater. Sci.* **2019**, *7* (1), 92–103.

(153) Adan, A.; Alizada, G.; Kiraz, Y.; Baran, Y.; Nalbant, A. Flow Cytometry: Basic Principles and Applications. *Crit. Rev. Biotechnol.* **2017**, *37* (2), 163–176.

(154) Taherian, A.; Li, X.; Liu, Y.; Haas, T. A. Differences in Integrin Expression and Signaling within Human Breast Cancer Cells. *BMC Cancer* **2011**, *11*.

(155) Liu, Y.; Bajjuri, K. M.; Liu, C.; Sinha, S. C. Targeting Cell Surface Alpha(v)Beta(3) Integrin Increases Therapeutic Efficacies of a Legumain Protease-Activated Auristatin Prodrug. *Mol. Pharm.* **2012**, *9* (1), 168–175.